Technical University of Denmark

DTU

Advanced optical design and control of multi-colored SSL system for stage lighting application.

Chakrabarti, Maumita; Petersen, Paul Michael; Dam-Hansen, Carsten

Link back to DTU Orbit

DTU Library
Technical Information Center of Denmark

DTU Fotonik
Department of Photonics Engineering

Advanced optical design and control of multi-colored SSL system for stage lighting application

Maumita Chakrabarti

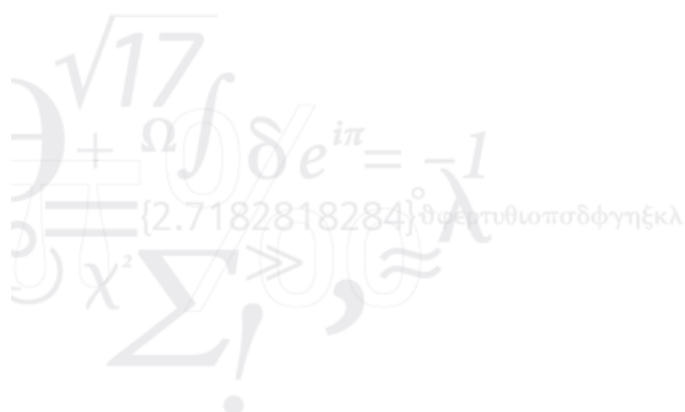Technical University of Denmark
Kongens Lyngby, Denmark
2016

Advanced optical design and control of multi-colored SSL systems for stage lighting applications

February 29

2016

PhD Thesis

Dedicated to

My parents, Arindam Adhikari and DTU LED group

Acknowledgements

The successful completion of this thesis has been possible only because of the professional and personal support from colleagues, friends, and family. Therefore I would like to express my acknowledgements for this kind help.

First of all, I would like to express my sincere gratitude to my supervisors Senior Scientist Carsten Dam-Hansen and Prof. Paul Michael Petersen for their priceless supervision throughout the years and for giving me the wonderful opportunity to work with LED related technology which was a completely new field to me three years ago. You both believe in me and that confidence provides me the fuel and drive to challenge myself to go through a most interesting project. In particular, I would like to thank you Carsten Dam-Hansen, for always being there with your insightful guidance, mentoring and discussions. You always encourage me and provide the moral support even when things were difficult. I will always be grateful to you for introducing me to the world of LED lighting and related technology. I am also grateful to Prof. Paul Michael Petersen for your valuable time for counseling on my PhD work and important suggestions related to the same. You have always had patience to listen me even when you were busy. Thank you both for being my supervisors and mentors, which I have enjoyed throughout my PhD time. What I have learned from both of you will be my capital for my future career.

I would like to thank Peter Behrensdorff Poulsen for his kind help and moral support. Being the project leader of the PhD project, you have always tried to provide the relevant information which was helpful. I have enjoyed your humor and our friendship, which make my time easy to pass. Your moral support has given me confidence.

The PhD work could not be possible to finish if I did not get kind support from a Danish lighting company Brother, Brother & Sons Aps. In particular, I would like to thank Thomas Brockmann, Peter Plesner, Christian Poulsen, and Esben Mallan for collaborating with me for the project and all their kind support.

I would like to give a warm gratitude to Prof. Emeritus Steen G. Hanson for introducing the speckle world to me. Earlier, I had a limited knowledge on the ABCD matrix and on speckle. You helped me to enhance my depth in the same field. I have also enjoyed your good humor. It was lovely working with you and Michael Linde Jakobsen. I enjoyed very much when we shared our success while eating cake. I would like to thank you both for giving me the opportunity to working with you both. In this regard, I would like to thank Dr. Harold Yura from University of California for being my examiner during the course evaluation process. I was honored when I came to know that you are one of the pupils of Nobel Laureate Prof. Richard Feynman.

I am truly fortunate to get kind help from Prof. Emeritus P.S. Ramanujam and Maria Louisa Rosenberg Welling for their technical and editorial checking of my thesis, respectively. Because of your reviewing comments, my writing was corrected and I feel

more confident. I would grateful to both of you and thank you both. Throughout the years Maria has not only checked my thesis, she has also checked all my articles. I would like to express my sincere thanks to you for your editorial support, kind help, and for your friendship. I would also like to thank Linda Christel for your kind help and friendship. You have helped me lot to fulfil the PhD formalities.

I have collaborated with different groups and different people with regards to project work packages throughout three years. I would like to thank all of you for your collaboration and kind help and moral support. In particular, I would like to thank Henrik Chresten Pedersen, Thøger Kari Jensen, Jørgen Stubager, Dennis Dan Corell, Jesper Wolff, Jørgen Jepsen, Anders Thorseth, Stela Canulescu, and Johannes Lindén. Although you are my colleagues, I have also enjoyed your friendship. In particular, I will miss Anders Thorseth and Dennis Dan Corell for your kind help as a friend, and our conversations and debates about diverse topics. You both become my close friends. I have appreciated the using of Matlab toolbox, which you both made.

I would like to express my sincere gratitude to Anders Kragh Hansen for your constant moral support and kind help as a friend. Many times I got technical help in Matlab from you which I appreciated. Whenever I had any issue, I shared with you and you have always tried to solve it as a true friend without any complains. I am grateful to have you as my close friend. So I would like to thank you and will miss you.

I would also like to thank my friends, colleagues, office mates, including our team-members, and senior members. In particular, I would like to thank Rebecca Bolt Ettlinger, Naghmehalsadat Mirbagheri, Thierry Silvio Claude Soreze, Mekbib Wubishet Amdemeskel, Sara Lena Josefin Engberg, Andrea Carlo Cazzaniga, Dominik Marti, Jakob Munkgaard Andersen, Aikaterini Argyraki, Ahmed Fadil, Sune Thorsteinsson, Søren Stentoft Hansen, Peter Jensen, Christian Pedersen, Ole Bjarlin Jensen, Haiyan Ou, Jørgen Schou, and Lars-Ulrik Aaen Andersen for your moral support, friendship, and valuable advice related to my PhD study. I will miss the lunch time talks with all of you, which I have enjoyed lot. I also would like to thank my flat mate Edgar Nuño Martinez, and bus mate Kasper Grann Andersson who believe in me and provide moral support and kind help.

I would like to thank Jan Kühn from the company JJ Kühn A/S and Thomas Fich Pedersen from Force technology for helping me to fabricate and characterize the microlens array which is a key component in my PhD work. I would like to thank to the companies JJ Kühn A/S, InMold, and Polerteknik for their helps to make TIR lens, mirror coating, and the raw mirror, respectively. In this context I would like to thank Henrik Chresten Pedersen again for collaborating with the project from Innovation Consortium LICQOP, grant #2416669. I would like to thank Hagen Schwitzer from Germany for his kind help to simulate a RGB color mixing system by the Unified Optical Design software (Wyrowski VirtualLab Fusion) from LightTrans UG. I would also like to thank Vladimir Leleko from Germany for his kind support and for sending a sample of diffuser made by Advanced Microoptic Systems Gambh for the optical characterization.

Summary

The thesis deals with a novel LED color mixing light engine which is designed, developed, and subsequently demonstrated by making a prototype of the same, which is experimentally investigated. Further, the design optimization solves the problems of achieving collimated high luminous flux in a color mixing system and provides a solution which is capable of replacing both the Fresnel lens spotlight Halogen lamp (2kW) and the commercially available LED luminaire (~160W), which have applications in stage lighting, theater lighting, TV studio lighting, etc. Since the optical design comprises LEDs, the light output from the light engine is energy and optically efficient as well as environmentally friendly. The light output stability during the operational time is investigated by using the Monte Carlo simulation and a color sensor is implemented along with the pre-calibrated lookup table to a feedback system in order to provide controlled color and intensity variations within certain limits. By implementing the control mechanism, system-to-system calibration is possible. The control mechanism can be generalized to be used in any other SSL system. Instead of using a color sensor, the variation in wavelength for a laser color mixing system can be detected by a new speckle based wavemeter, which is easy for use and cost-effective compared to the commercially available expensive spectrometers. The thesis also reports on the fabrication of a tool for replicating the microlens structure used for beam homogeneity, which overcomes the expensive and tedious manual polishing or direct diamond turning. The tool fabrication provides an easy and inexpensive mold and hence a cost effective injection molding replication process.

Resumé

Afhandlingen omhandler optisk design, optimering og eksperimentel undersøgelse af et nye multifarvede LED optisk systemer. Det er resultatet af et højteknologifonds projekt udført i samarbejde med Brother, Brother & Sons omkring lyskilder og lamper til professionel belysning af studier og teatre. Resultatet er et nyt LED optisk system kaldet V8 light engine som muliggør en fokuserbar lysstråle med variable korreleret farvetemperatur fra en 50 mm gate, kombineret med en meget høj lysstrøm på mere end 20.000 lumen. Dette muliggør erstatning af traditionelle tungsten halogen lyskilder på 2 kW og er en markant forbedring af tilsvarende LED baserede lamper på markedet. Der er udviklet og afprøvet en ny og prisbillig metode til masseproduktion af mikrolinse array som er den for farveblandingen vigtigste komponent i systemet. Dette er et afgørende resultat for kommercialiseringen af V8 light engine da mikrolinse arrayet er den potentielt dyreste komponent i det optiske system. Afhandlingen fokuserer derudover på de styrings og kontrolmæssige problemer af sådanne multifarvede LED og laser belysningssystemer som kan varieres i lysets spektrale sammensætning. Der er opbygget en model for et farvekontrol feedback system baseret på en farvesensor. Monte Carlo simuleringer har vist nødvendigheden af og resultater af implementering af et sådant system til V8 light engine. Der er udviklet og indsendt en patentansøgning på et nyt speckle spektrometer, der vil kunne benyttes til farvekontrol af laserbaserede lyskilder. Afhandlingens resultater er publiceret i ti reviewed journal papers og konference proceedings.

List of publications

Articles in international peer-reviewed journals:

1. Maumita Chakrabarti, Michael Linde Jakobsen, and Steen G. Hanson,"*Speckle-based spectrometer*",**Opt. Lett.** Vol. 40, No. 14, 2015.*

2. M. Chakrabarti, A.Thorseth, D. C. Corell, and C. Dam-Hansen, "*A white-cyan-red LED lighting system for low correlated color temperature*", **Lighting Res. Technol.** 2015; 0: 1–14; * DOI: 10.1177/1477153515608416

3. M. Chakrabarti, C.Dam-Hansen, J.Stubager, T.F.Pedersen, and H.C.Pedersen, "*Replication of optical microlens arrays using photoresist coated molds*", **Opt. Express** 24(9), 9528–9540, 2016. *

4. Chakrabarti, M., Thorseth, A., Jepsen, J., and Dam-Hansen, C., "*Color control for tuneable white LED lighting system*", manuscript submitted in **Lighting Res. Technol.** on 29th February' 2016.*

5. Chakrabarti, M., Pedersen, H.C., Petersen, P.M., Poulsen, C., Behrensdorff Poulsen, P., and Dam-Hansen, C. "*Focusable, color tunable white and efficient LED light engine for stage lighting*", manuscript submitted in **Optical Engineering** on 29th of February 2016.*

Articles in international peer-reviewed conferences:

1. Chakrabarti, M., Thorseth, A., Jepsen, J., and Dam-Hansen, C. "*Monte Carlo Analysis of multicolor LED light engine*" Proceedings of 28th **CIE** Session 2015, OP60, 526. *

2. Maumita Chakrabarti, Anders Thorseth, Jørgen Jepsen , Dennis D. Corell, and Carsten Dam-Hansen, "*A color management system for multi-colored LED lighting*", **SPIE** proceedings, Vol. 9571 -10, 2015. *

3. Steen G. Hanson, Michael Linde Jakobsen, and Maumita Chakrabarti,and, "*Speckle based wavemeter*" Proc. **SPIE** 9660, SPECKLE 2015: VI International

Conference on Speckle Metrology, 96600U (August 24, 2015); doi:10.1117/12.2195629 *

4. Steen G. Hanson, Michael Linde Jakobsen, Maumita Chakrabarti, and H.T. Yura, "*Finding small displacements of recorded speckle patterns: revisited*" Proc. **SPIE** 9660, SPECKLE 2015: VI International Conference on Speckle Metrology, 96601J (August 24, 2015); doi:10.1117/12.2195631

5. Chakrabarti, M.; Thorseth, A.; Corell Dan, D. and Dam-Hansen, C., "*Optical design for multi–colored LED lighting systems for museum lighting application*" **3rd European-Asian workshop on Light-Emitting Diodes,** D2-02, 2014.

Patent application:

1. Maumita Chakrabarti, Michael Linde Jakobsen, Henrik C Pedersen, and Steen G. Hanson, "*Speckle-based spectrometer*" PA201500158, submitted in March 2015

*After receiving the permission from the respective publishers and also from co-authors, the author has used identical phrasing in the thesis as in the articles in some instances.

Abbreviations

BSDF: Bidirectional scatter distribution function

BRDF: Bidirectional reflectance distribution function

CCT: Correlated color temperature

CIE: Commission Internationale de l'Eclairage

CMFs: Color matching functions

CNC: Computer numerical control

CRI: Color rendering index

CQS: Color quality scale

DMX: Digital multiplex

ESTA: Entertainment Services and Technology Association

FWHM: Full width half maximum

 IP: Internet protocol

IS: Integrating sphere

IVL: Inverse square law

JND: Just noticeable difference

LED: Light emitting diode

LID: Light intensity distribution

MA: Microlens array

nm: Nanometer

PAC: Photochemical active polymer

PCB: Printed circuit board

PMMA: Polymethyl Methacrylate

PVD: Physical vapor deposition

RGB: Red, green and blue

SPD: Spectral power distribution

TIR: Total internal reflection

TLCI 12: Television Lighting Consistency Index

Table of Contents

Introduction and background

> *'For, usually and fitly, the presence of an introduction is held to imply that there is something of consequence and importance to be introduced.' – Arthur Machen*

Chapter 1 : Introduction and background

1.1 Motivation

The traditional light like high intensity incandescent/tungsten halogen lights [1] have been used particularly for studio or stage lighting. The electrical power requirements for such lights are substantially high (∼2kW) to illuminate the stage sufficiently with more than 10, 000 lm luminous flux. Hence those luminaires produce enormous heat and infrared radiation during the operating time and thus are not environmental friendly. Also; such lights require multi-color mechanical/optical filter devices which are subtractive method of color filtering to provide effective changes in projected light color ultimately make the luminaire even less efficient. In addition, the range of colors in such light sources is limited. Looking into those mentioned problems, in present scenario the traditional stage lights are replaced by light emitting diodes due to the improvement in efficiency and performance reliability[2], [3]. The arrays of multi-color LEDs can also be controlled selectively with certain intensity providing a wide range of tunable colors and light intensities [4]–[6]. However, there are several LED luminaires available in the market which uses white LED with filter as a subtractive color mixing. The efficient way of color mixing technique is additive. Some LED luminaires use color beams from individual color LEDs through lenses, and color mixing mechanism is possible by overlapping the different color beams into each other. The mixing of three color LEDs (Red-Green-Blue), four color LEDs (Red-Green-Blue-Amber or Red-Green-Blue-White) are a few examples of similar kinds of luminaires[7]. Although four color LEDs are providing a better color rendering index (CRI) than the three color luminaire, they both have shortcomings of the color shadows [8]. There are other possibilities to get unlimited color mixing with the package of multi-color LED die, integrated with single lens. However there will be a tradeoff on the flexibility of getting high luminous flux from one single package. Thus, in general it is required to have a multi-colored LED luminaire with a high lumen and also a high CRI. In addition, it is also necessary to have very compact illumination devices for handling, which is difficult to achieve when more light sources are integrated into the same illumination device. Due to etendue

limitations[9], [10], the task of combining light from an unlimited amount of light sources into a narrow light beam is difficult. One solution to this problem could be the case where an optical system collects the light from the optical gate and is adapted to image the optical gate at a target surface. Recently, the lighting architecture on such a system are described by Dennis Jørgensen [11] and Gadegaard et. al[7]. However, this design cannot sufficiently produce light of more than 10, 000 lm. Thus the present market clearly sets the demand of a new kind of luminaire which would provide the solution towards the stated problem. The stage lighting prerequisites focusable white light. Due to collimation property of laser light, it can be another potential candidate as an illuminator. There is a state-of-the-art available for white light coming from color mixing by laser[12]. However, the laser has a much narrower spectral linewidth than light emitted from LEDs or phosphors which may not create better comfort in visual perception than a broader spectrum. Furthermore, due to the demand of high luminous flux, the color mixing from several color lasers cannot be an inexpensive solution for the stage lighting. To address those issues, an advanced optical design of the additive color mixing technique by combining several colored LED beams with the help of microlens array (MA), positioned at the output gate of the luminaire, is proposed in this thesis[13]–[15].

To obtain flexibility in optical design it is always recommended to simulate the optical model beforehand. The optical simulation allows the design optimization and the modification easily and provides the cost effective solution. Thus initially, the color mixing technique and the proposed advance optical design are investigated by geometrical as well as spectral simulation considering a simple tri color LED lighting system[16]. The optical simulation of that tri color system has been taken and extended as a tool of the optical simulation for five color LED lighting system, called as V8 light engine.

The white light produced from the color mixing would suffer from color variation over time[17], [18]. Therefore there is a requirement of intelligent control loop to resist the color variation. The control system could work effectively if known uncertainties of the influencing parameters could be investigated and used as an input into a feedback loop[19], [20]. This leads to explore the spectrometric information from the light output. To examine the color mixing by laser and the corresponding color variation over time persuades to discover the idea behind speckle wavemeter, which is able to detect the wavelength change in the scene[21], [22]. However, in order to know the color variation form the LED based light output, the use of the speckle wavemeter cannot be seen as an optimal solution. Implementing the color sensor inside the feedback loop is the smart way of controlling the color variation which also gives the cost effective solution than using a spectrometer. Thus, this thesis also documents the proposed work on this field[23]–[25].

1.2 Aim of the project

The scientific idea behind the PhD project "Advanced optical design and control of multicolored SSL systems for stage lighting applications" is to develop, investigate and

analyze an optical system that collimates and combines the light beams from a number of colored high power LED arrays into a single focusable beam. Through intelligent control of the individual colored LEDs the resulting light will be able to:

1. cover a large color gamut area

2. cover a range of white light corresponding to different color temperatures and characterized by high color rendering properties and high beam homogeneity.

This will provide a fundamentally new focusable light engine that fully utilizes the potentials of LED components in energy efficiency and high light quality. This type of light source has, however, not yet been realized despite the rapid achievements in LED technology. There are two major problems with LED light sources using additive color mixing today[26], [27]. They suffer from either poor color rendering or generate colored shadows behind the illuminated objects. In order to overcome these problems without sacrificing efficiency, new innovative ideas on the optical systems are required. Furthermore, a better understanding of color rendering, control, uniformity and stabilization is needed. If these problems are overcome; the results would be of major interest in the LED and lighting R&D community as well as in the lighting industry. The solution also will be capable of replacing the Halogen-Fresnel spot lamp (2kW) as well as the commercially available LED luminaire (~160W) which has applications in stage lighting, theater lighting, TV studio lighting, etc.

The PhD project is part of the R&D project "LIGHT ENGINE V8 – A green revolution for colored light", which has been granted by The Danish National Advanced Technology Foundation in 2012. DTU Fotonik is running the project in collaboration with the Danish company Brother, Brother & Sons Aps, who would take the LED technology into the future of professional lighting in the entertainment industry. The possible application areas would be far more widespread and architectural as well as display lighting is going to be investigated further for cost effectiveness. The scientific contributions made in relation to the study period of this project are patented and published in peer-reviewed scientific articles.

1.3 Outline of the chapters

The study and the related work of the PhD project has been documented in this thesis divided in seven chapters. The short description about the chapters and their relation in connection to scientific articles are outlined below:

Chapter 1: describes the motivation of the study on the topic of the PhD project and the achievable goals behind the idea of researching on advanced optical design for multi-colored LEDs for stage lighting application. It also elaborates the state-of-the-art on LED lighting technology and corresponding measuring techniques of LED luminaires.

0: provides the state-of-the-art on the traditional stage lighting. The shortcomings and advantages of traditional stage lighting compare to LED stage lighting are listed. The experimental results from tungsten-halogen luminaire and LED luminaire (market

available) show the capability of present stage lighting system. The chapter also comments on the forecast on the upcoming stage lighting.

Chapter 3: introduces with V8 light engine covering the architectural design aspect of the same. It also defines the required optical components used to demonstrate the prototype of the V8 light engine. The geometrical simulation of the optical design optimizes the individual optical components within the light engine with respect to beam homogeneity, optical loss and luminous light output. There is a peer-reviewed scientific article on this new advanced optical design of a multi-colored LED system which provides the tunable, focusable and collimated while light with dimmable capability. The chapter designates the design aspect of the MA, which has been used as a secondary optics inside the V8 lighting design. It also elaborates on the new fabrication tool used to produce the MA and the characterization technique to investigate the working performance of the same.

Chapter 4: presents the state-of-the-art on additive color mixing techniques and the advantage of using the same concept on subtractive filtering method. The spectral simulation of color mixing technique is verified by taking a simple example of three colored LED system. The V8 system which is more complicated having five color LEDs, however, it essentially uses the same building blocks while simulating the design. The peer-reviewed article is considered to publish the corresponding scientific contributions. The three colored optical system is demonstrated subsequently by making a prototype which is used in the display cases of the exhibition at Rosenborg Castle in Copenhagen, Denmark.

Chapter 5: elaborates on the color consistency aspect of the LED device and the related research on spectral color control of the resulting beam which optimizes the color gamut, color rendering and optical efficiency of the light engine. Initially, the uncertainties in the multi-colored LED device are analyzed by the Monte Carlo simulation and the new algorithm to reduce the uncertainties inside the system is proposed by implementing a color sensor and a feedback control loop, respectively. The spectral model can be validated by proposed experiments. This chapter also describes the published peer-reviewed scientific articles related to the above mentioned study. For laser based color mixed luminaire, the spectrometric information is required to detect the color variation. This chapter therefore discloses the new idea behind a speckle based wavemeter and the related peer reviewed article which can be used to analyze the wavelength change of the lasers being used during the operation.

Chapter 6: establishes the experimental facility and the characterization of the V8 light engine. The experimental results have been validated by the optical simulation. The results also indicate the modification of the shape and size of the optical components used in the V8 design to achieve the target luminous flux from the light engine. There is an extensive investigation of the optical loss encounters from the different optical components inside the system which guides the total loss calculation from the optical system. Finally there is a comparison of light output between the Halogen-Fresnel spot luminaire and the V8 light engine.

Chapter 7: concludes the 3 years study as well as the work for the PhD project. It also indicates the future recommended work plan as outlook on the same field which did not finish within the short period of three years' time. The chapter also gives a market survey on the present scenario of stage lighting and their pros and cons in connection to market demands. There is a thorough discussion on the advantage of using V8 as a stage lighting system over available lighting systems, like Arri, Desisti etc. The chapter also directs the application areas where the V8 light engine could be used as an illuminating device.

Chapter 8: offers the listing of publication details which have followed as reference during the study period.

The next section explains about the basic physics behind the LED technology and its advantages over the traditional lighting.

1.4 LED lighting technology

The illumination from LED is efficient, extremely long lasting, and enormously versatile. As the future lighting technology, LEDs offer maximum flexibility to lighting designers, architect, electricians, and private consumers. The technology provides cost savings in power consumption and maintenance. Light management systems (LMS) with LEDs provide the perfect control for planning valuable LED lighting solutions. The following are the advantages of LED technology over traditional lighting technology:

- Low power consumption

- High efficiency level

- Long lifetime

- Continuous dimming capability

- Smallest possible dimensions and compact module

- High resistance to switching cycles

- Immediate light when switching on

- Wide range in operating temperature

- High impact and vibration resistance

- Reliability on different environmental conditions

- Absence of UV or IR radiation

- High color saturation level without filtering

- No mercury is used in the manufacturing of LEDs. Thus it is mercury free

As a result the LED technology is exploited in many applications in different industries such as indoor lighting (home, office, hospitals, retails, etc.), outdoor lighting (sports, stage, theater, studio, street, etc.), backlighting, automobile lighting (headlight,

indicator, sensor, etc.). For those applications, the efficiency of the LED lighting is attractive. In this context the luminous efficacy is a measure of how well a light source produces visible light for a given electric power. Thus, the luminous efficacy is the ratio of luminous flux to electrical power (lm/ W). The following Figure 1-1 provides the guidelines on efficiency of any range of white light from different kind of light sources. The fraction of electromagnetic power which is useful for lighting can be a measure for luminous efficacy of radiation. The luminous efficacy of radiation can be obtained by dividing the luminous flux by the radiant flux. Since, the light with wavelengths outside the visible spectrum contributes to the radiant flux while the luminous flux of such light is zero, those wavelengths reduces luminous efficacy. Therefore, wavelengths which are near to the peak of the eye's response contribute more strongly than those near to the edges. For the case of monochromatic light at a wavelength of 555 nm (green), the Photopic (explained in 1.5.1) luminous efficacy of radiation has a maximum possible value of 683 lm/W corresponds to an efficiency of 100%, whereas the Scotopic (explained in 1.5.1) luminous efficacy of radiation reaches a maximum of 1700 lm/W for narrowband light of wavelength 507 nm. So the white light which are the mixture of several wavelengths, never can achieve the luminous efficacy of 683 lm /W. The progress of white LEDs is much more prominent nowadays and white LEDs' luminous efficacy has increased from 5 lm/ W to today's commercial white LED of 150 lm/ W which is till now the highest luminous efficacy of all white light sources. However, as explained above, the theoretical limit for white LEDs is about 260-300 lm/W. So the luminous flux efficacy of LEDs continues to reach higher values than other light sources[28]–[31] in laboratory. The available value of 265 lm/ W is already achieved in the laboratory[29]. However, the shortcoming of this specific design is that the luminous flux is about 14.4 lm. By modifying the design, the researchers confirmed two other white LEDs with values of 203 lm and 183 lm/ W at 350 mA, and with values of 1913 lm and 135 lm/W at 1 A, respectively. Figure 1-1 shows the theoretical border of available commercial white LED at the present scenario. The improvement of efficacy in luminous light output by LED leads to annual energy savings of USD1.8 billion in the US market according to the report in 2013 from US department of energy[32]. For the US nation, the potential payoff for the solid state lighting is enormous and it is estimated that converting entirely into LED lighting would save the country USD 39 billion in annual energy cost, reducing the energy consumption from the lighting by more than half and avoid 280 MT of carbon emission each year. Thus, potential demands of using LED as a primary illuminating source is increasing day by day.
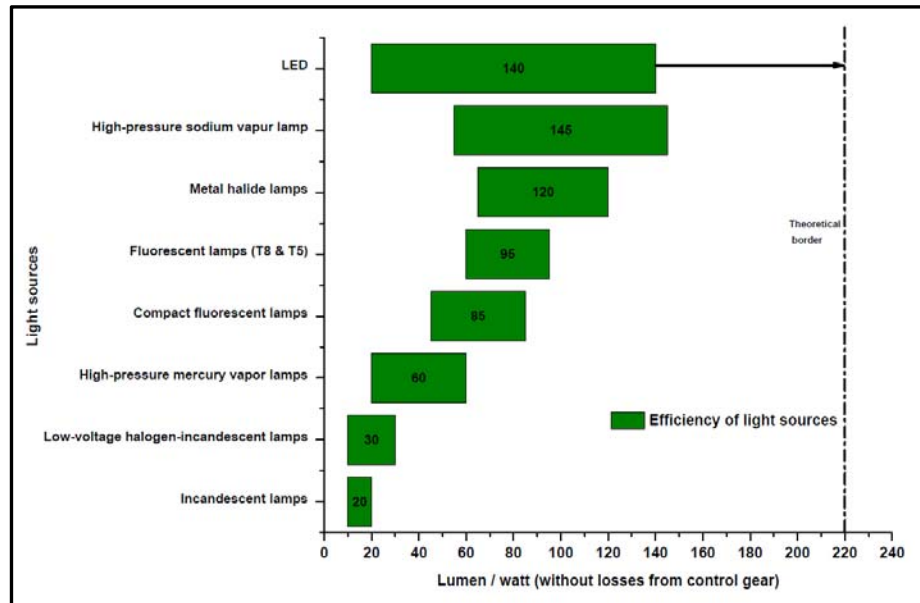
Figure 1-1: The present scenario of optical luminous efficacy for white light from the different kind light sources (Source Ref.[33])

The basic principle of an LED consists of multiple layers of semiconducting material. Light is produced in the active layer while the diode is being used with direct current. The produced light is decoupled directly or emits by reflections. In contrast to continuous spectrum emitting from incandescent reflector lamps, an LED emits light of a distinct wavelength. The light's wavelength or color depends on the composition of the crystal compounds of the semiconductor material used. In order to produce LEDs with a high degree of brightness in all colors from blue to red, two material systems such as phosphide or arsenide are mainly used. These could create various combinations, each of which releases varying amounts of energy according to the material's bandgap. When charge carriers (holes and electrons) are recombined by applying specific voltage in an LED print circuit board, photons are emitted in terms of light according to specific discrete energy levels. This specifies the particular light color for LEDs. For example, blue light is produced if a high level of energy is released and a lower level of energy is responsible for red light emission. Each LED light color is limited to a very narrow range of wavelength called the dominant wavelength of the corresponding color. Since LED produces only monochromatic (single color) light, the only spectrum that cannot be produced directly from the LED print circuit board is the white light spectrum, which represents a mixture of all light colors. There are two methods for producing white LED light: photoluminescence and additive color mixing. Thus the white color is obtained either from luminescence conversion of blue color LED or by mixing red, green and blue LEDs (RGB). The state-of-the-art for additive color mixing is discussed in detail in Chapter 4.

There are few factors which influence the reliability and operating life of the individual LED and also on the entire LED module. When light is produced due to increase of heat in terms of increasing junction temperature, both the life cycle and the LED's luminous flux affects. That is why it is essential to manage the heat by the best possible installation method or by suitable heat sinks. The cooler LED has the longer life cycle, and has a more efficient and brighter light output. The LED operating temperature also can influence the working performance of LED in same way. Every LED can be operated within a specific current range. The lower the current is within this range, the less energy is released and the lower the heat production would be; which has a direct effect on the operating life. The following section would provide the measurement technique of light output from LEDs.

1.5 Measuring techniques for LED lighting

The term called lighting only exists due to the visual perception of the human eye. The radiant energy that is basically an electromagnetic wave, capable of exciting the retina and the construction of a visual sensation inside the retina is called light. There are several distinct regions of this electromagnetic spectrum namely; ultraviolet, visible and infrared, etc., which are designated by the range of wavelengths. The visible portion extends from about 380 nm to 780 nm. In this, we have dealt with visible light emitted from LEDs in the V8 system. To characterize the light, we need to know the basic knowledge behind the photometry and colorimetry as well as the measurement technique which have discussed in this section.

1.5.1 Photometry

Photometry is the science concerned with measuring visible light in terms of its perceived brightness by the human visual response. CIE defines the spectral response of the average human eye by measuring the adapted light by eyes and compiling the data into the photopic curve. The curve indicates that people respond strongly for the color green and are less sensitive to the spectral extreme regions red and violet. The eye has a different response characteristic in the dark-adapted state and as such it has difficulty in defining color. This leads to a second set of measurements and the compiled data is called a scotopic curve. Figure 1-2 shows the response curve for photopic and scotopic, respectively. Both the photopic curves (CIE 1931 [34] and CIE 1978) have peaks at 555 nm, whereas the peaks are shifted to 507 nm for scotopic curve. In this thesis all calculations are based on the photopic response curve by CIE 1931 and CIE 1978, respectively.
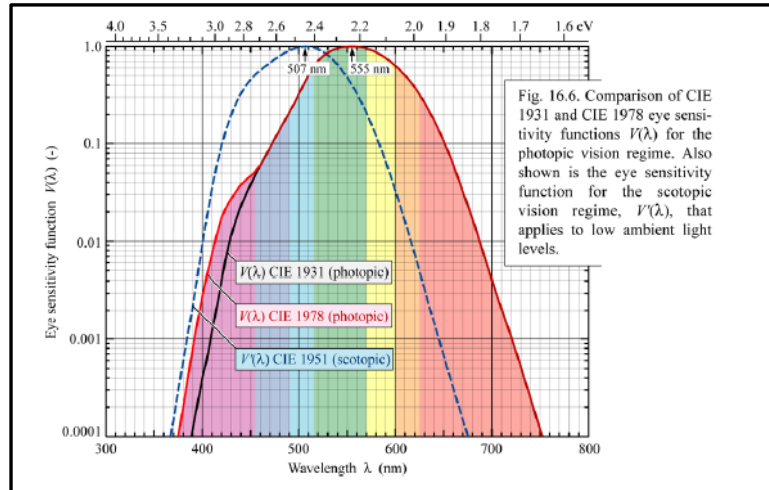
Figure 1-2: The CIE 1931 V(λ), the CIE 1951 V(λ) and the CIE 1978 V(λ) functions are shown (Source Ref.[35])

To define the various photometric quantities it is required to know the terminology of lighting terms, symbols and units (Table 1-1).

Table 1-1: Photometric quantities with the units (Source Ref.[36])

Quantity	Symbol	Metric unit	English unit
Luminous intensity	I	candela (cd)	candela (cd)
Luminous flux	Φ	lumen (lm)	lumen (lm)
Illuminance	E	lux (lm/m²)	fc (lm/ft²)
Luminous exitance	M	lm/m²	lm/ft²
Luminance	L	cd/m²	cd/ft²

Luminous intensity (I): is assumed as the fundamental quantity, defined by the unit called candela (cd). The unit of luminous intensity was established in 1860 by using a certain type of candle of specific weight burning at a specific rate. The first incandescent lamp had a luminous intensity equal to 16 candles, and the corresponding voltage was 110 volts (AC). It is also defined as the quantity of luminous flux emitted uniformly into a solid angle. Thus, 1 cd is equivalent to one lumen per steradian.

Luminous flux (Φ): is another quantity, defined by the unit called lumen (lm). It is the rate at which luminous energy is incident on a 1-m² surface from a distance 1 m from a uniform point source of 1 cd intensity, as shown in Figure 1-3. It is a measure of the total optical output of a visible light source.
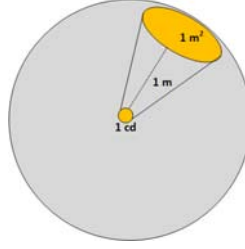
<p align="center">**Figure 1-3: 4 π lumens emits from 1 cd uniform point source (Source Ref.[36])**</p>

Illuminance (E): is the 'Φ' density incident on a surface. In English units, one lumen of flux falling on one square foot is called a footcandle. The metric equivalent, one lumen per square meter, is termed a lux (10.76 lux = 1 footcandle). When light incidence occurs on an object, it has reflection, transmission and absorption depending on the medium of incidence. It also follows certain rules. The following are the common rules considering the measure of the illuminance.

Inverse square law (ISL): for point source is when the illuminance on a surface is inversely proportional to the square of the distance from the source. The largest dimension of the light source is much smaller than the distance where the illuminance is measured. In that case, the illuminance should measure the distance of five times the source size, called the five times rule. However, for the strong directional source such as a laser cannot follow the five times rule. In that case the minimum distance can be ten times to the source size.

Lambert's cosine law: is that the illuminance on any surface depends on the cosine of the light's angle of incidence. The following equation (1) describes the formula:

$$E_\theta = E \, cos\theta \qquad\qquad (1),$$

where incident angle 'θ' is measured with respect to the surface normal.

Luminous Exitance (M): is the density of 'Φ' leaving the surface in all direction known as exitance. The unit is the same as illuminance which is lm / m2. The luminous exitance measurement is most appropriate in emitters with a flat surface.

Luminance (L): is also referred to as the photometric brightness, it is the density of 'Φ' leaving the surface in a particular direction. The technique takes into account the area of the surface measured, and the angle subtended by an observer looking at it. Thus, the following equation (2) defines the formula:

$$L = \frac{I}{ACos \propto}$$

where 'A' is the projected area and 'α' is the subtended angle. For perfectly diffuse (Lambertian) surface both 'M' and 'L' is related to the equation (3).

$$M = \pi L \qquad\qquad (3)$$

1.5.1.1 Luminous flux measurement:

To measure accurately the total radiant flux, the 'Φ' and the spectral power distribution, integrating sphere (IS) photometer is commonly used. By this measurement, the lamp lumen, luminous efficacy, CRI, and color appearance parameters (e.g. CIE x, y, and CCT) can be determined[37]–[39]. An IS is a hollow sphere with its interior uniform reflectance coating by barium sulfate to create nearly perfect diffuse reflectivity as the lambertian surface. The reflectance depends on the thickness of the coating. The coating is thermally stable at approximately 100° C, and generally the commonly available reflectance is from 80% to 95%. Figure 1-4 describes the basic principle of the IS theory. The light reflects multiple times before entering the detector indirectly as the direct light is blocked by the baffle. The measuring total of 'Φ' is found by using an illuminance meter, where the measurement by the photometer is compared to the similar measurement obtained from a calibrated lamp of known output, commonly referred to as the "comparison method". The results of this comparison determine the light output of the test lamp. The following Equation (4) - (6) [36] shows the formulae to measure the flux from the IS:
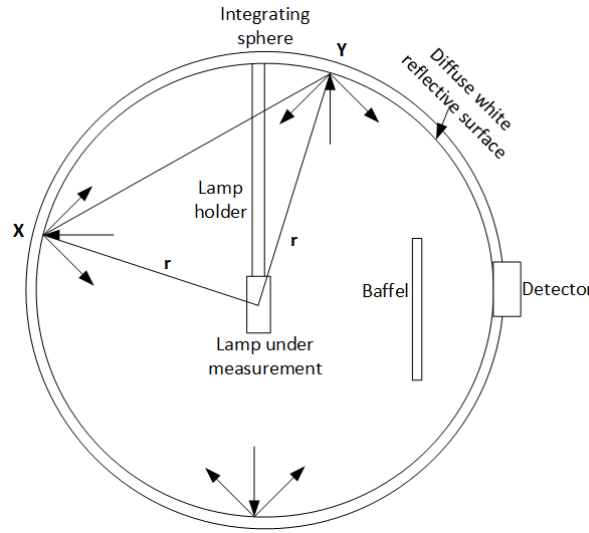
Figure 1-4: Total luminous flux measurement using an integrating sphere

$$\Phi_{ref} = \rho\Phi(1 + \rho + \rho^2 + \cdots . + \rho^n) = (\frac{\rho}{1-\rho})\Phi \qquad (4)$$

$$E = \left[\frac{\rho}{4\pi r^2(1-\rho)}\right]\Phi \qquad (5)$$

$$\Phi = \left(\frac{1}{k}\right)E \qquad (6),$$

where 'ρ' is the reflectance of the interior surface, 'Φ' is the luminous flux of the lamp, 'r' is the radius of the sphere, 'E' is the illuminance on the interior, 'k' is the constant

determined using a standard reference lamp. A spectrometer at the detector port enables flux and color measurements. The measuring total 'Φ' using a spectrometer measures the radiant power as a function of wavelength. The luminous flux interpretations for the sensitivity of the eye by weighing the radiant flux at each wavelength with the human eye response function. Equation (7) is the formula for measuring the total 'Φ' from the spectrometer:

$$\Phi = 683 \int_{360}^{830} S_\lambda V_\lambda d\lambda \qquad (7),$$

where 'λ' is the wavelength, 'S_λ' is the SPD, 'V_λ' is a function representing the wavelength-dependent sensitivity of the eye. The luminous efficacy of a light source is measured by the total 'Φ' emitted by the lamp divided by the total lamp power (electrical) input. It is expressed in lumens per electrical watt. In this thesis, the IS of 1 m and 2m diameters respectively equipped with an array spectroradiometer (CAS-140CT) are used according to the CIE LED test standard[40] by using the quality lab (Q – lab) facility of the Light Quality Measurement Laboratory, at DTU Fotonik. The light was coupled through the side port (15 cm diameter) in a forward flux configuration and a self-absorption correction was applied.

1.5.1.2 Intensity distribution measurement:

The luminous intensity distribution of the luminaires can be measured by a goniophotometer or a goniospectrometer. The goniophotometer and coordinate systems are categorized into three types which are Type A, Type B and Type C. The angular distribution of the spectral and luminous intensity of the luminaire is measured in this thesis by a Type C nearfield goniophoto /spectrometer (RiGO-801)[41], which is equipped with an array spectrometer (specbos1211), a color camera (LMK 98-4 color), and a photometer(PH-ST-C8-TH-L). Figure 1-5 shows the goniometric coordinates system for the Type C. This equipment is also situated in the Quality lab (Q – lab) facility of the Light Quality Measurement Laboratory, DTU Fotonik. The measurement distance is 1.4 m. Thus, the goniometric measurement can be used as far field measurement where the measurement distance 1.4 m is within the five times of source size [40], [42]. The camera captures the images of luminance distributions of the luminaire at different angles using V_λ filters. By changing the filters to X1, X2, and Z, the measurements can analyze the values of X, Y, and Z (tristimulus values) of the light at different angles. The CCT and Duv can be calculated afterwards at different angles from those tristimulus values. The integrated values of measurements with V_λ filter would give the total 'Φ' of the luminaire as V_λ can be taken as 'Φ' of the light. The spectrometric measurement would also provide the information of CCT distribution of the light at different angles, if the luminaire is of small size compared to the measurement distance (followed five times rule), where the goniospectrometer measurement acts as a far field measurement. However, for the larger size of luminaire the spectrometric measurement would introduce an error. The photometer measures the 'E' of light distribution for all directional and integrated value of all distributions provide the total

luminous flux 'Φ' of the luminaire. All measurements are calibrated with a total luminous flux standard lamp from a National Metrological Institute (NMI).
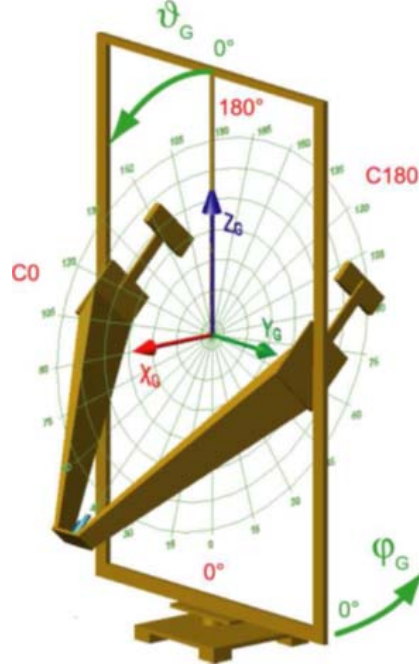
Figure 1-5: Goniometer Coordinate System (Ref. [41]**)**

1.5.2 Colorimetry

The assessment and quantification of color is referred to as colorimetry or the "science of color" [35]. To characterize the light quality of the light output, it is necessary to measure the color parameters like CCT, D_{uv}, CRI, etc. The following would define the parameters which are used in this thesis.

1.5.2.1 Color matching functions ($\overline{x}(\lambda), \overline{y}(\lambda), and \overline{z}(\lambda))$: The CIE has standardized the measurement of color by means of color-matching functions and the chromaticity diagram (CIE, 1931) [34] as the sensation of the color is a subjective quantity. The three color-matching functions are obtained from a series of adjusting the relative intensities of the red, green, and blue light, in which the subject sets the intensities of the three primary lights required to match a series of monochromatic lights across the visible spectrum. The CIE 1931 color-matching functions $\overline{x}(\lambda)$, $\overline{y}(\lambda)$, and $\overline{z}(\lambda)$ are shown in Figure 1-6. The green color-matching function, $\overline{y}(\lambda)$, is chosen to be identical to the eye sensitivity function, V(λ), i.e.:

$$\overline{y}(\lambda) = V(\lambda) \tag{8}$$
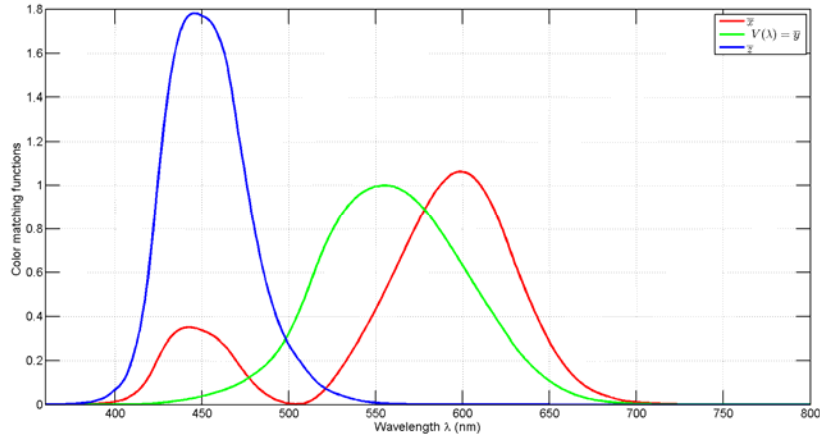
Figure 1-6: CIE (1931) 2° color matching functions (CMFs)

The three color-matching functions portray the fact that human color vision possesses trichromacy, and the color of any light source can be described by just three variables, which are dimensionless quantities. There have been several different versions of the color-matching functions and of the chromaticity diagram as any of them are not unique.

1.5.2.2 Tristimulus values (X, Y, Z): give the stimulation (i.e. power) of each of the three primary red, green, and blue lights needed to match the color of P(λ) which is power spectral density or power spectrum. The relation between P(λ) and the tristimulus values are as follows:

$$X = \int_{360}^{830} \bar{x}(\lambda)P(\lambda)d\lambda \tag{9}$$

$$Y = \int_{360}^{830} \bar{y}(\lambda)P(\lambda)d\lambda \tag{10}$$

$$Z = \int_{360}^{830} \bar{z}(\lambda)P(\lambda)d\lambda \tag{11}$$

According to the above definition, tristimulus values should have the unit of *watt*. However, the tristimulus values are usually considered as dimensionless quantities where there will be a pre-factor of *watt⁻¹* before integral.

1.5.2.3 Chromaticity coordinates (x, y, and z): are the stimulation of each primary light divided by the entire stimulation which are as follows:

$$x = \frac{X}{X + Y + Z} \tag{12}$$

$$y = \frac{Y}{X + Y + Z} \tag{13}$$

$$z = \frac{Z}{X + Y + Z} = 1 - x - y \tag{14}$$

As seen in equation (14), z chromaticity can be found from x and y, though it is not required to use. Thus, the chromaticity diagram is made by the x and y coordinates in Figure 1-7. In this diagram, the reddish, greenish and bluish hues are found for large values of x, y and z. Figure 1-7 also illustrates the location of the Planckian locus, which is the black line in the diagram. All colors can be characterized with respect to their location in the chromaticity diagram. The figure also shows the equal-energy point found in the center of the chromaticity diagram which has (x, y, z) = (1/3, 1/3, 1/3). The optical spectrum corresponding to the equal-energy point has a constant optical energy per wavelength interval dλ across the visible spectrum. The outcome of such spectrum results in equal tristimulus values, i.e. X = Y = Z. The color differences of closely spaced points in the chromaticity diagram must have a minimum geometrical distance to yield a perceptible difference in color. In 1943 MacAdam [43] showed that the colors within a certain small region in the chromaticity diagram appear identical to human subjects and those regions have the shape of ellipses. Such ellipses are called as the MacAdam ellipses. It also indicates that the geometric distance between two points in the (x, y) chromaticity diagram does not scale linearly with the color difference.
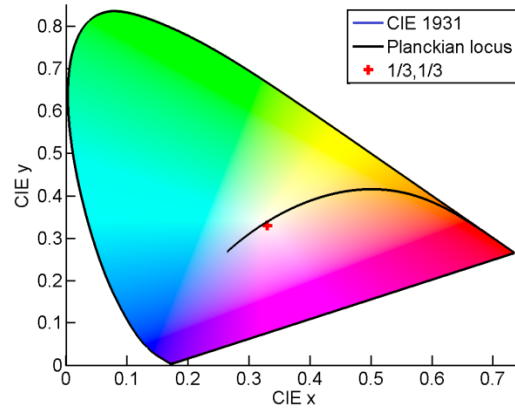
Figure 1-7: CIE 1931 (x,y) chromaticity diagram where monochromatic colors are found at the perimeter and white light is situated in the center of the diagram

1.5.2.4 Uniform chromaticity coordinates (u, v, u′, v′): If the color difference in the chromaticity diagram is proportional to the geometric difference, it is convenient and desirable. In 1960, the CIE introduced the (u, v) and in 1976 the (u′, v′) uniform chromaticity coordinates to form the uniform chromaticity diagram[44][45]. From the tristimulus values, the uniform chromaticity coordinates are calculated according to the

below equations (15)-(16). The CIE 1960 and CIE 1976 (u′, v′) uniform chromaticity diagrams are shown in Figure 1-8 (a-b). The (u, v) and (u′, v′) uniform chromaticity coordinates can also be calculated from the (x, y) chromaticity coordinates and vice versa according to the equations (17)-(20).
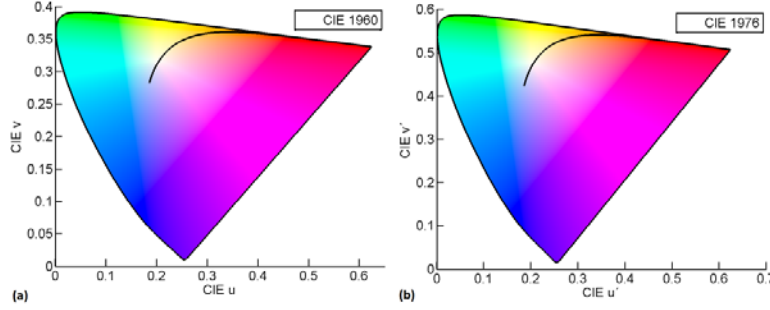
Figure 1-8: (a) CIE 1960 (u, v) and (b) CIE 1976 (u′, v′) uniform chromaticity diagrams calculated using the CIE 1931 2° standard observer respectively

$$u = \frac{4X}{X + 15Y + 3Z} \, , \qquad v = \frac{6Y}{X + 15Y + 3Z} \; and \tag{15}$$

$$u' = \frac{4X}{X + 15Y + 3Z} \, , \qquad v' = \frac{9Y}{X + 15Y + 3Z} \tag{16}$$

$$u = u' = \frac{4x}{-2x + 12y + 3} \tag{17}$$

$$v = \frac{6y}{-2x + 12y + 3} \, , \qquad v' = \frac{9y}{-2x + 12y + 3} \tag{18}$$

$$x = \frac{9u'}{6u' - 16v' + 12} \, , \qquad y = \frac{2v'}{3u' - 8v' + 6} \; and \tag{19}$$

$$x = \frac{3u}{2u - 8v + 4} \, , \qquad y = \frac{2v'}{2u - 8v + 4} \tag{20}$$

The color changes much more rapidly in one direction, e.g. the x-direction, compared to the other direction, e.g. the y-direction in (x, y) chromaticity diagram (Figure 1-7) as the color differences between two points in this diagram are spatially non-uniform. Although the deficiency of the (x, y) chromaticity diagram is not eliminated fully in the (u, v) and (u′, v′) uniform chromaticity diagrams, the color difference between two locations in the uniform chromaticity diagram is (approximately) directly proportional to the geometrical distance between these points.

1.5.2.5 Alternative to the MacAdam Ellipses: The CIE recommends that the (u',v') chromaticity diagram denotes the most uniform color space for light sources. In Figure 1-9, the five-step MacAdam ellipses (solid black line) are plotted in the CIE (u',v')

diagram, on top of which circles with radius of 0,0055 (dashed red line) are plotted. As shown in the figure, these ellipses and the circles are closely overlapping, which indicate that in the white region near the Planckian locus in the (u',v') diagram, circles can be used as an alternative to the MacAdam ellipses. Thus, it was also found that the five-step MacAdam ellipses are approximately equivalent to the circles with radius 0.0055 in (u',v'). The u'v' circle is specified with a center point (u_c', v_c') and radius 'r' on the (u',v') diagram, and expressed by the equation (21) [46]. For consistency within the MacAdam ellipses in the (u', v') chromaticity diagram, the term "n-step u'v' circle" is defined by CIE [46] as a circle in the (u', v') diagram with a radius of n times 0.0011. For a center point (u_c', v_c'), the n-step u', v' circle is calculated by the equation (22) where 'n' corresponds to a n-step MacAdam ellipse.
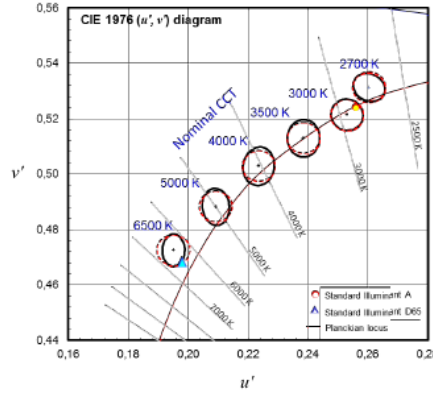
Figure 1-9: Five-step MacAdam ellipses in IEC 60081 (IEC, 1997) and circles (radius 0. 0055) in the CIE 1976 (u',v') chromaticity diagram (Source Ref.[46])

$$(u' - u'_c)^2 + (v' - v'_c)^2 = r^2 \qquad (21)$$
$$(u' - u'_c)^2 + (v' - v'_c)^2 = (0.0011 . n)^2 \qquad (22)$$

A just noticeable difference (JND) is recommended by CIE at 50% probability is considered to be (0.0011 × 1.18 =) 0.0013 in (u',v') coordinates. In the white region of the (u',v') diagram, chromaticity differences between the two points (u_1', v_1') and (u_2', v_2') on the (u', v') diagram which is expressed by the distance in (u',v') coordinates calculated by $\Delta u'v'$ is shown in the equation(23).

$$\Delta u'v' = \sqrt{(u_1' - u_2')^2 + (v_1' - v_2')^2} \qquad (23)$$

1.5.2.6 Chromaticity distance: is the closest distance from the Planckian locus on the (u', 2/3 v') diagram, with '+' sign for above and '-'sign for the below the Planckian locus and denoted by D_{uv}[47]. The Figure 1-10 indicates the D_{uv} sign by arrow.
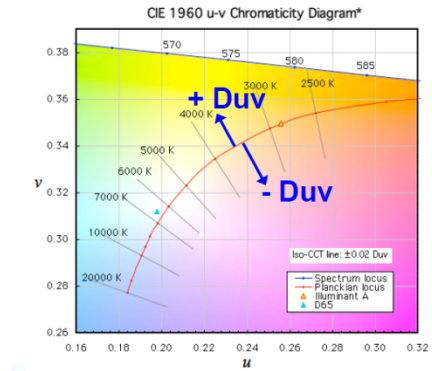
Figure 1-10: magnified CIE 1976 u´- v´ diagram (Source Ref. [48])

1.5.2.7 Color temperature and correlated color temperature: The color temperature (CT) of a white light source is the temperature of a Planckian black-body radiator which has the same chromaticity location as the white light source considered and the unit of CT is kelvin. With increasing temperatures, it glows in the red, orange, yellowish white and finally a bluish white and according to that color variation it is distinguished by few regions called warm white, neutral white and cool white respectively. If the color of a white light source does not fall on the Planckian locus, the correlated color temperature (CCT) is used which is defined as the temperature of a Planckian black-body radiator, whose color is closest to the color of the white light source. The CCT is also given in units of kelvin.

1.5.2.8 Color gamut: The color gamut represents the entire range of colors area that can be created from a set of primary sources. Color gamut is a polygon positioned within the perimeter of the chromaticity diagram. Depending on the number of primary color, the shape of the gamut change as for the case of three primary colors, the color gamut is a triangle. The produced white light for the additive color mixing, all mixing colors created by the vertex points (primary colors) of a gamut, is located inside the same gamut (dash line in Figure 1-11). The wide color gamut is desirable to have flexibility of creating white light in an additive color mixing procedure.
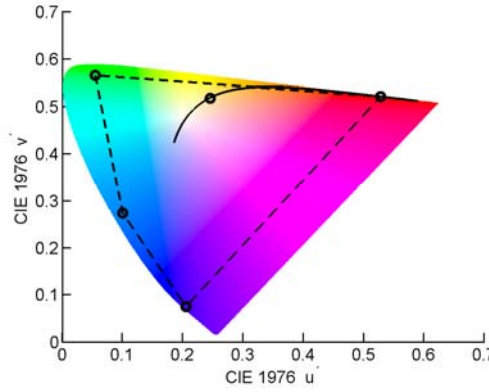
Figure 1-11: The area surrounded by dash line is the color gamut for four primary colors

1.5.2.9 Color rendering index (CRI): The ability to render the true colors of a physical object (e.g., fruits, plants, human skin, flowers, wood, furniture, clothes, etc.) which are being illuminated by the white light source is measured in terms of the color-rendering index (CRI)[49]. The evaluation of CRI is made by comparing the color rendering ability of test light source with the color rendering ability of reference source. The reference source recommended by CIE [49] follows certain rules which are:

(i)   Planckian black-body radiator would be the reference source with the same color temperature as the test source would be considered, if the chromaticity point of the test source is located on the Planckian locus

(ii)   The reference source would be a Planckian black-body radiator with the same correlated color temperature as the test source if the chromaticity point of the test source is located off the Planckian locus

(iii)   For other instances, one of the standardized CIE illuminants would be used as a reference source

(iv)   It is also considered that the test source and the reference source should have the same chromaticity coordinates and luminous flux output

Conventionally, the CRI of the Planckian black-body reference source is anticipated to have CRI = 100 and the test source never has CRI > 100. The sensitivity dependency of CRI indicates that the selection of reference source is always critical while calculating CRI of test sources. As the test-color samples are defined in terms of their spectral reflectivity, the test-color samples play an important role for calculating the CRI of a test source in addition to the reference source and the test source. Thus, in intension of having international standardization, a set of fourteen test color samples has been recommended for the purpose of determining the CRI of the test source. According to the CIE standard, general CRI, which is an average, is calculated as follows[35]:

$$CRI_{general} = \frac{1}{8}\sum_{i=1}^{8} CRI_i, \tag{24}$$

where CRI_i is called as special CRIs for a set of eight test-color samples. The special CRIs are calculated according to the following formula[35]:

$$CRI_i = 100 - 4.6\Delta E_i^*, \tag{25}$$

where ΔE_i^* represents the quantitative color change while a test-color sample is illuminated with, firstly, the reference source, and later with the test source[50]. The general CRI (R_a) is calculated from the eight test color samples (i = 1–8). In addition to the eight test-color samples, six supplemental test-color samples (numbers 9–14) are used to further assess the color rendering abilities of test sources while CRI_9 to CRI_{14} are referred to as the special color rendering indices 9–14. After investigating the reflectivity curves, the colors of the test-color samples 9–14 have particularly strong colors with relatively narrow peaks and thus these supplemental test-color samples have the following colors effect: 9 – strong red; 10 – strong yellow; 11 – strong green; 12 – strong purplish blue; 13 – complexion of white person; 14 – leaf of tree. Although people show several shortcomings of judging the color rendering capabilities of the light source by CIE's CRI method, this is still internationally agreed upon by popular standard. Thus the light quality is characterized in this thesis by calculating general CRI (R_a) and other special CRI (R_9 – R_{14}) considering the CRI for the Planckian locus illumination sources as the V8 light engine produces white light, which can be tuned from 3000 K to 6000 K with low D_{uv} (< 5 * 10^{-3}) values.

1.5.2.10 Color Quality Scale (CQS): The National Institute of Standards and Technology (NIST) has developed another color standard (CIE TC1-69) [51], [52] with close contacts in the lighting industry and the CIE to address the problems of the CIE CRI for solid-state light sources and to meet the new needs in the lighting industry and consumers for communicating color quality of lighting products. CQS evaluates several aspects of the quality of the color of objects illuminated by a light source such as chromatic discrimination and observer preferences. The CQS incorporates important modifications in CRI to overcome its shortcomings and focuses on a broader definition of color quality. The CQS uses a set of 15 Munsell samples having the much higher Chroma, span the entire hue circle in approximately even spacing, and are commercially available. The CRI can result in negative values for some lamps whilst the CQS imposes a 0-100 scale.

1.5.2.11 Television lighting consistency index (TLCI-2012): Another color standard is relevant in this context which is TLCI – 2012 [53]. This program is intended to be used for the assessment of light sources for use in television lighting. The metric defines a 'standard' camera, and then uses it to analyze a set of test colors when illuminated by a standard source and by the source under test. The colorimetric differences between the two exposure conditions, when viewed on a reference display, are calculated according to the principles espoused by W.N.Sproson and E.W.Taylor of BBC R&D, in: 'A color television illuminant consistency index' by BBC R&D Report 1971/45. The primary result from this method provides a single number, ranging from 0-100, representing the TLCI of the test light source. In general the higher number the better, with a perfectly rendering light source having a TLCI of 100 as with CRI and CQS. Usually, any light source with a TLCI of 85 or greater would be usable with a video camera with little

or no adjustments to the camera. As the scale goes down, generally the sources with a TLCI between 50 and 85 would still be usable but would need correction in the video chain setup to get acceptable results. Finally, a source with a TLCI scale less than 50 may not be usable, even with substantial correction, principally when used on sensitive colors like skin tones.

1.5.2.12 IES TM-30-15: Because of the complexity of characterizing the color rendition property of a light source; presently, there is no one metric or scale that can accurately enumerate all aspects of color rendition and/or classify the most desirable light source for every application. Thus, recently IES TM-30-15 [54]–[56] elaborates on a method for evaluating a light source color rendition that quantifies the fidelity (closeness to a reference) and gamut (increase or decrease in Chroma) of a light source by incorporating an objective and statistical approach. However, using Fidelity Index (R_f) and Gamut Index (R_g), user could utilize the two-dimensional characterization to determine what is most appropriate for the specific application in consideration. The method also creates a color vector graphic that specifies the average hue and Chroma shifts, which also interprets the values of R1 and R_9.

1.6 Summary

This chapter describes the background of the project as a motivation of the project. This is followed by the project goal to achieve an advanced optical lighting design for color control in LED stage lighting which would fulfil the present market demand of achieving an energy efficient, tunable white, homogeneous and powerful luminous light output without sacrificing the light color quality. This chapter also provides the substances of the following seven chapters. From section 1.4 onwards the chapter elaborates on the state-of-the-art of the LED technology and the measuring technique of the LED luminaire which is adopted in this thesis. The following chapter covers the state-of-the-art in traditional stage lighting and the pros and cons over LED stage lighting.

Traditional lighting systems

'Deepajyothi parabrahma
Deepa sarva tamopahaha
Deepena saadhyate saram
Sandhyaa deepo namostute

I prostrate to the dawn/dusk lamp; whose light is the Knowledge Principle (the Supreme Lord), which removes the darkness of ignorance and by which all can be achieved in life'

Chapter 2 : Traditional lighting system

2.1 Introduction

As our main purpose to replace the traditional lighting by LED lighting for improvement in energy savings and other critical aspects, according to the application requirements, it is important to know in detail about the pros and cons of both of the lighting systems. Hence, this chapter mainly deals with the traditional lighting systems characterization which is especially used on the stage of a theatre or in a studio. However, before going there, we need to know what stage lighting is and the history behind it.

There are two types of lighting equipment required to illuminate the stage; namely, general illumination and specific illumination. The general illumination provides a diffuse, shadow-less, wash of light over the entire stage space. Candle, oil, gas, and electric lamps are examples of general illumination[57]–[60]. Candles were introduced as theatre lighting in the late 15th century in Italy and England. In the late 17th century, a Swiss chemist developed the modern oil lamp which soon replaced the candles as the primary light sources. The world's first gas stage lighting system was installed at the Chestnut Street Theatre in Philadelphia in 1816. From then on, gas lighting was widely adapted and used in experimental purposes in most countries of the Western World. In the 1880s, the incandescent mantle (burner) was introduced producing a much brighter and safer light. Hereafter, Thomas Edison made the first practical incandescent electric lamp in 1879. By the end of the 19th century, most modern theatres had replaced gas lights by the much safer electric lights. In 1903, the Kliegl Brothers

installed an electric lighting system with 96 resistance dimmers at the Metropolitan Opera House in New York City.

Specific illumination provides a sharp, highly controlled shaft of light, introduced by the lime light in the middle of the 19th century. Those shafts were used to highlight a small area of the stage, a principle actor, or to create the illusion of sunlight or moonlight. The concept of using light as spotlight, floodlight and footlight were started by using lens boxes or other alternatives. Thomas Drummond was the inventor of calcium light, also known as lime light or Drummond light. Later on, the newer and brighter carbon arc lamp began to slowly replace the lime light in the modern theatre. Although the safer incandescent spotlight started to gradually replace the carbon arc lamp, the arc lamp continued to be used as a follow spot until the end of 20th century. The era of electric spotlight started in 1904. Kliegl brothers started to introduce innovative design of planoconvex spotlights, Fresnel lens spotlight and ellipsoidal reflector spotlight which are still being used to this date in stage lighting systems.

Generally, a floodlight produces a large, almost uncontrollable wash of light whereas a spotlight produces a small highly controlled pool of light. Floodlights are mostly used to light the backdrop (such as scenery) while spotlights are used to shine light on the actor. Table 2-1 will explain the category and properties of the instruments [60].

<center>**Table 2-1 Instrument details, using in the stage lighting of theatre**</center>

Instrument	Category	Beam angle	Spill	Edge quality
Ellipsoidal	Reflector spotlight	Fixed	Very little	Hard
Fresnel	Lens spotlight	Variable	Quite a bit	Soft
PARCan	Spotlight	Fixed	Some	Soft
Scoop	Reflector floodlight	Fixed	A lot	Soft
Border light	Floodlight	Fixed	A lot	Soft
Follow spot	Spotlight	Variable	Almost none	Hard

2.1.1 Drawbacks of traditional lighting

Recently the movement of LED light fixtures into the theatre lighting is gradually increasing due to the disadvantages of the standard lighting [2], [3], [6]. The standard lighting fixtures mostly use a halogen light rated from 300 to 1000 W, and are energy inefficient. Although these lights produce a solid color as well as a good brightness at a distance, they have many drawbacks. There is a large amount of energy wasted with halogen lights as a result of the heat produced. This demands to put an extra ventilation system in theatres. Thus, the theatres have to be designed to adequately vent the heat away from the lights. Beside this, the use of halogen lights requires a large energy infrastructure to get a large amount of electricity. The design and infrastructure for the lighting system to accommodate an extra supply of electricity and ventilation increases the initial cost of the theatres. Another drawback of using the halogen lights is the short life span of the light bulbs, rated 2000 – 4000 hours of use[61]. The life span of bulbs is relatively short in terms of hours used by a theatre. Generally, a light used for 3 hours a day, 5 days in a week will have a life span between 130 and 200 days. The replacement cost for bulbs for incandescent lights range from USD15 - USD25/bulb, which in turn need to be replaced about twice a year for each light. Due to not having the color tuning

facility, another drawback to standard theatre lighting is the use of gels to generate other colors. The heat produced from the incandescent light fixtures limits the lifespan of the gel as it is made from plastic materials. The transition from flood position of light to spot, there is almost ~37% energy loss in the traditional lighting which is also a shortcoming.

2.1.2 LED theatre lighting

With advanced technology the use of lights in theatres is growing day by day. There are several advantages of using LED lighting over traditional lighting. Energy consumption is less in LED lighting compared to incandescent lamp. Instead of having 300–1000 W for incandescent lighting, LED lighting consumes only 100 W, the lower energy consumption further reduces the cost of theatre infrastructure. LED lighting produces less heat which helps to reduce energy consumption of the HVAC system. Another more significant benefit of LED lighting system over traditional lighting is the longer life span. The LED modules used in theatres are rated from 50000 hours at 70% operation which is 12.5 to 25 times longer than traditional bulbs. Thus, the LED modules would last for nine years. The maintenance cost and associated problems of changing bulbs are significantly reduced in LED lighting systems. They also eliminate the problems of trapping dust and other particles in lights. To obtain multicolor lighting, gel is not mandatory for LED lighting systems and LED light fixtures contain several color options which are preprogrammed into the light fixture. The color changing and moving LED lights are very popular to obtain various colors in that scenario.

There are few drawbacks of using LED lighting systems in theatres. Basically, LED lighting is more effective in a short distance as it is less bright compared to traditional lighting systems. Thus the use of traditional light fixtures in long range lighting is still superior. The white light from one company is not the same as the white light from another company. The difference in color and quality will keep the customer committed to the same company in the future, should a light fixture need replacing. Beside this, the price of an LED light fixture is more expensive than the traditional lighting systems. On the top of that, the LED lighting technology is booming and the new development in LED theatre lighting is creating better lights every year. The light fixture would likely be replaced instead of the just the bulb as the technology continues to improve, which makes the earlier investment in lighting system wastage.

The aforementioned issue would be resolved by the solution which is described in this thesis. The thesis demonstrates the light engine which would provide the cost effective energy efficient light output conceptualized by the latest LED technology. The intelligent color control inside the light engine regulates the light output within certain limit so that the user cannot distinguish the light variation among several similar light engines within a scene. Another advantage of the described optical design is that the energy loss from flood setting to spot setting is improved by a factor of 6.

There are several types of projectors such as PROFILE SPOTS (fitted with knife edges or a gobo), FOLLOW SPOTS, AMBIANCE SPOTS, etc., used in theatres or on stage. To understand the working functionality of traditional lighting and available LED luminaire, the light output is characterized from the spotlight Halogen-Fresnel luminaire as single lens luminaire (Figure 2-1 (a)) and the commercially available LED

luminaire (Figure 2-1 (b)). The following sections describe the characterization in detail.
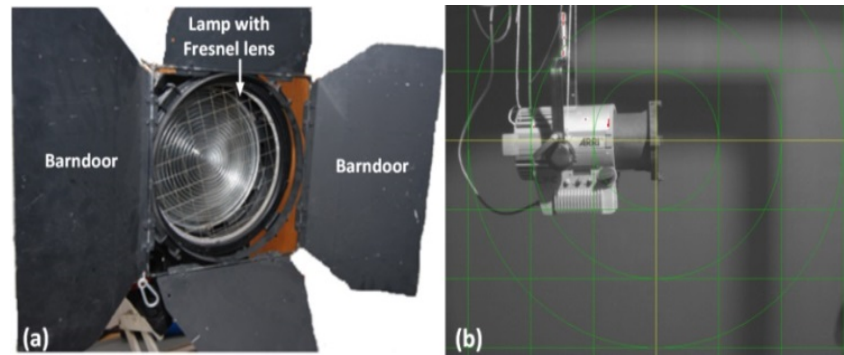
Figure 2-1: (a) Halogen-Fresnel spotlight (b) LED luminaire

2.2 Characterization of 2 kW Halogen-Fresnel luminaire

Compact, highly efficient Fresnel lens spotlight using tungsten–quartz–halogen filament luminaire having maximum power of 2 kW for 120 V is characterized by measuring its light output. During the operating time, the luminaire was powered by 1.8 kW in the Q–lab at the Technical University of Denmark. Both photometric and radiometric measurements were recorded by a 2 m IS and photo-goniometer and the measurement techniques are already explained in Chapter 1 under section 1.5.1.1 and 1.5.1.2, respectively. The photometric integrating sphere measurement done by 2 π measurements is shown in Figure 2-2(a). Figure 2-2 (b) and (c) show the luminaire alignment during the near-field goniometric measurement. The size of the pool of light is determined by the throw and the position of the focusing knob: Spot to Flood. The experimental results are shown in Table 2-2. The maximum measurement deviation between two measurements is 0.4%. From this result it is clear that the measurement results have consistent values between the two measurements. From the table it is seen that there is ~37% loss in luminous flux while the flood lighting position changes to the spot lighting position.
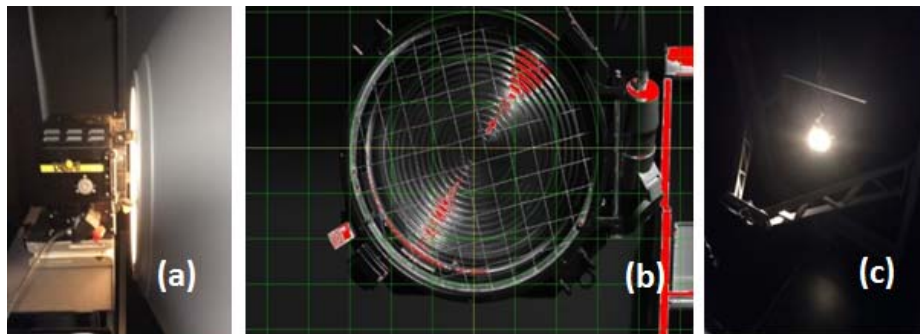
Figure 2-2: (a) 2 π photometric measurements by 2 m integrating sphere; (b) Near field goniometer alignment of the luminaire; (c) Near field goniometric measurement

Table 2-2 : Compared measured value of flux by an integrating sphere and goniometer, respectively

Halogen-Fresnel luminaire at 1.8 kW electrical power	Φ Measured by Integrating sphere [lm]	Φ Measured by goniometer [lm]	ΔΦ%
Flood	18745	18803	0.3
Spot	11777	11717	0.3

Hand held Luxmeter (PRC- RdioLux 111) were used to measure the illuminance value of the luminaire at a field distance of 5.28 m after setting the spot and flood positions of the luminaire. For a different angle of illuminance, the intensity of the luminaire was also calculated by using the following equations: (26)-(28) where 'r' is shown in Figure 2-3. The luminance can be measured by the equation (29). If $\theta = 0$, then the intensity was calculated according to equation (30), where 'D' is shown in Figure 2-3. The experimented results are documented in Table 2-3.

$$I_\theta = E_\theta r^2 \tag{26}$$

$$Now, E_\theta = \frac{E_{\theta=0}}{Cos\theta} \tag{27}$$

$$I_\theta = \left(\frac{E_{\theta=0}}{Cos\theta}\right) r^2 \tag{28}$$

$$L = \frac{I_\theta}{ACos\theta} \tag{29}$$

$$I_{\theta=0} = E_{\theta=0}D^2 \tag{30}$$
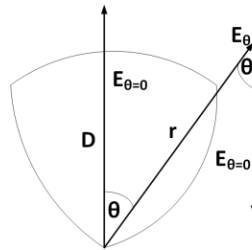
Figure 2-3 : Diagram of LID for different angle of θ

Table 2-3: Comparison of the experimental illuminance and intensity value for flood and spot position

Halogen-Fresnel spot lamp @ 1.8 kW	$E_{\theta=0}$ [lux] @ 3m (calculated)	$E_{\theta=0}$ [lux] @ 5.28 m (measured)	$E_{\theta=0}$ [lux] @ 6 m (calculated)	$E_{\theta=0}$ [lux] @ 9 m (calculated)	$I_{\theta=0}$ [cd]	Field angle [deg.]	FWHM [deg.] @ 50%
Flood by luxmeter	3763	1212	941	418	33902	69	50.6
Flood by goniometer					28345		
Spot by luxmeter	26364	8510	6591	2929	237273	24	10.8
Spot by goniometer					243075		

In the table, the illuminance ($E_{\theta=0}$) at different distances for flood and spot position of the luminaire as well as the intensity of the light by the luxmeter is reported. The measurement value of intensity by goniometer is verified and the deviation between two measurements is maximum 2%. The experimented LID for flood and spot position from the luxmeter and goniometer measurements, respectively, has been graphically plotted in Figure 2-4. The measured CRI was 99.9 and average CCT value was 3055 K.
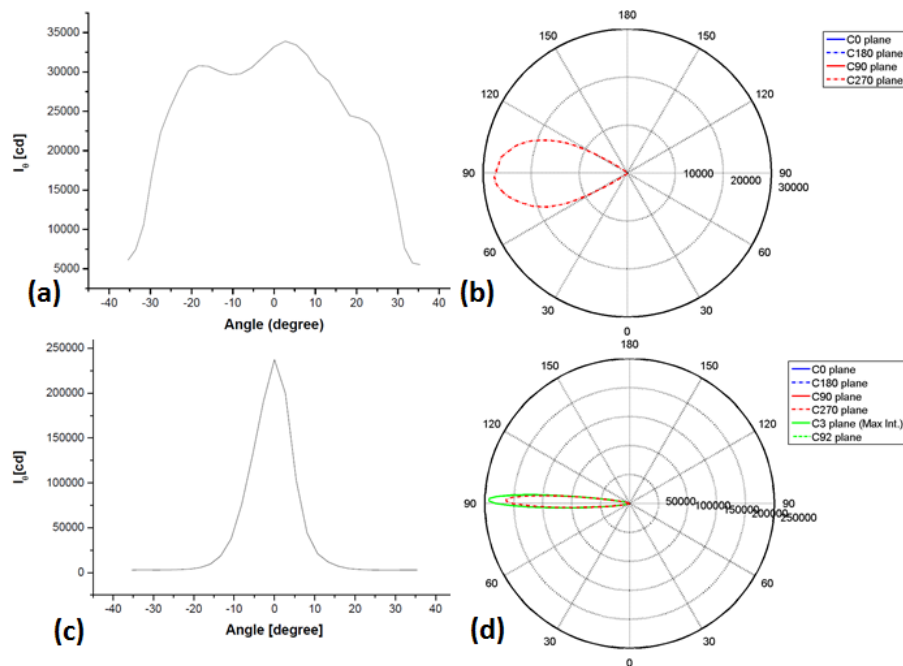
Figure 2-4: (a) & (c) represent LID at different angles for flood and spot position respectively, measured by a luxmeter; (b) & (d) depict the same LID measured by goniometer, where the c-planes are depending on luminaire mounting direction

2.3 Characterization of LED luminaire

The light output from the LED luminaire has a maximum of $\Phi = 4000$ lm. Therefore, the present LED luminaire is also not fulfilling the current demand of stage lighting.

However, the total Φ and LID are measured by using a 2m IS and goniometer. The Φ for flood and spot positions at 3000 K are 4052 lm and 3412 lm, respectively. Figure 2-5 (a) shows the measured Φ and corresponding measured CCT of actual CCT tuning from 2800 K to 5800 K at flood position. The measured CCT has a linear relation with actual CCT, R^2 = 0.99. For the flood position, the maximum Φ is 4975 lm at 4000 K and the minimum Φ is 3465 lm at 2800 K. The CRI at all CCT ranges is between 97 and 90, seen in Figure 2-5(b).
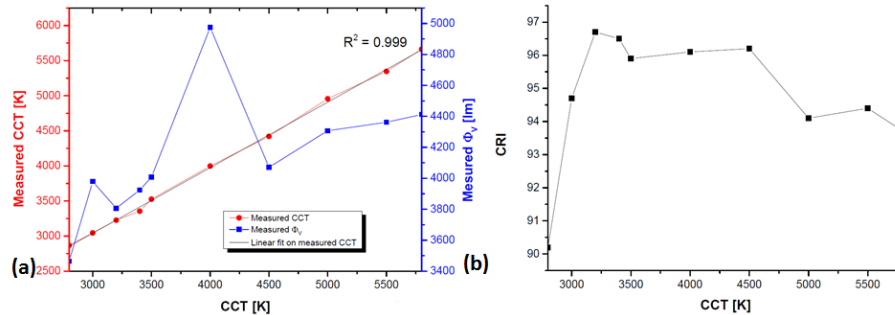
Figure 2-5 (a) Measured CCT and measured Φ for tuned CCT (2800 K – 5800 K); (b) Measured CRI for tuned CCT (2800 K – 5800 K)

The goniometric measurements are shown in Figure 2-6 for flood and spot positions. The energy loss from the flood lighting position to the spot lighting position is 18%.
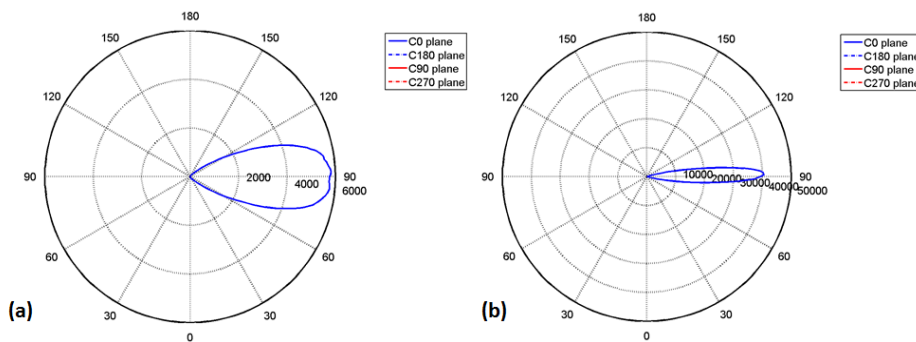
Figure 2-6:(a) LID at flood (b) spot positions respectively for the LED luminaire where the c-planes are depending on the luminaire mounting direction

2.4 Summary

This chapter describes the pros and cons of traditional stage lighting and compared those properties with an LED luminaire. There are two examples of light characterization of the two luminaires, one is the traditional Halogen-Fresnel luminaire and the other one is the LED luminaire. Both the luminaire shows the high energy loss during the transition from the flood lighting position to the spot lighting position. The experimental results prove that the present LED luminaire cannot fulfil the immediate market requirements of LED stage lighting with a high luminous flux (>10,000 lm)

without compromising the light quality. The following chapters will introduce with the V8 light engine by elaborating on the optical design (Chapter 3), color mixing technique (Chapter 4) and control system (Chapter 5) of the luminaire. The experimental results from the V8 light engine (Chapter 6) will show the betterment of stage lighting over traditional lighting.

Optical design and modelling of V8 light engine

*'Music is the arithmetic of sounds
as optics is the geometry of the
light.' – Claude Debussy*
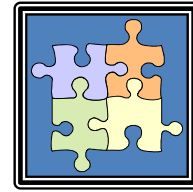
Chapter 3 : Optical design and modelling of V8 light engine

3.1 Introduction

As mentioned in the section 1.2 in Chapter 1, the aims of the V8 optical design are; (1) to replace the traditional stage lighting by improving the optical efficiency, (2) to obtain compact focusable, homogeneous and high luminous flux, (3) to provide dimmable intensity and tunable white light output from 3000 K to 6000 K, (4) to have high light quality in terms of CRI (> 85), (5) to improve the energy loss from flood setting to spot setting and last not the least, (6) to get intelligent spectral control to provide output stability. This chapter deals with the optical design and modelling of the V8 light engine to simulate optical efficiency of the entire light engine, which would address the aforementioned goals. In principle, the modelling will lead to an overall estimate of the luminous light output from the outer end of the optics. The V8 light engine is the integration of more than one optical component. The simulation will be taking care of optimization of critical optical component in terms of obtaining maximum luminous light output, proper color mixing and optimum color homogeneity of the entire optical system. The next paragraph will describe the V8 light engine followed by the details of optimization of the component used in the V8 optical system.

3.2 Description of V8 light engine

The objective of the V8 light engine is to be a powerful, focusable light engine in stage lighting application which could be used in theatres, auditoriums, or similar other stage shows. It is designed to produce the luminous light output (Φ) from the light engine to exceed 20,000 lm with an extremely high color homogeneity in the aimed region, which is going to be published in a scientific journal [14]. The schematic diagram of the light

engine is seen in Figure 3-1 (a) which consists of: (1) Printed circuit board (PCB), (2) LEDs, (3) Total internal reflection (TIR) lenses, (4) Parabolic reflector, (5) Optical gate, (6) Microlens array (MA), and (7) Fresnel lens. The parabolic reflector and TIR lenses are used as primary optics and the MA, and Fresnel lens are used as secondary optics. The optical gate is surrounded by different colored LEDs and TIR lenses which are sitting on the PCB, making an LED cluster of seven rings inside the V8 light engine (as seen in Figure 3-1 (b)). The quasi-collimated beam from the individual LEDs transmitted through the total internal reflection lens (TIR) is reflected by the parabolic reflector and is directed towards the optical gate, which is situated at the focal plane of the reflector. The optical gate is acting as an aperture and limits some of the reflected beam to pass through the gate. The hexagonal patterned double-sided convex MA, called a Kohler integrator, is used at the gate position to combine a large number of quasi-collimated beams from the individual colored LEDs arriving at the MA at different angles into a homogenous color mixed beam. To obtain better color mixing and color homogenization from the light engine, the MA is customized, which is also going to be published in a scientific journal [13] and discussed in 3.3.6. The light engine mixes the color from four colored LEDs (Green, Red, Blue, and Royal Blue) with several white LEDs to produce intensity dimming (minimum 5% of total luminous flux) and color tuning (3000 K to 6000 K with a 100 K resolution) white light. Finally, the Fresnel lens is used to collect all light output from the gate and to provide collimated light output from the light engine. The transition of the Fresnel lens towards the gate can change the focusable spot position to flood setting.

To maximize the light output such as Φ and to achieve a good light quality with a high CRI (>85) and a low D_{uv} (< 10^{-3}), the used components inside the light engine need to be optimized. A spectral model for optimizing the color mixing of LED beam is described in Chapter 4. The optimization on the geometrical optical design to accomplish a high Φ is done by using the optical software Zemax which is elaborated on the next section. The component description and functionality used inside the V8 light engine is also particularized on the next section. The V8 light engine also incorporates the color feedback system which will help to get a good consistency of luminous light output as well as color over operational time which is described in Chapter 5.

(a)

(b)
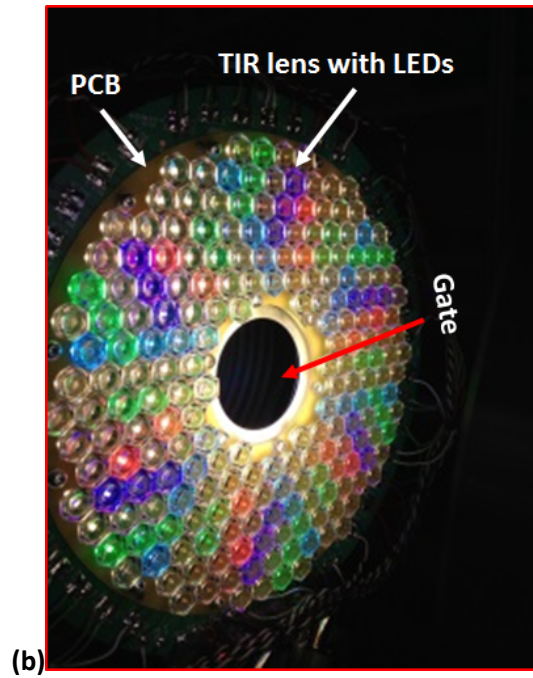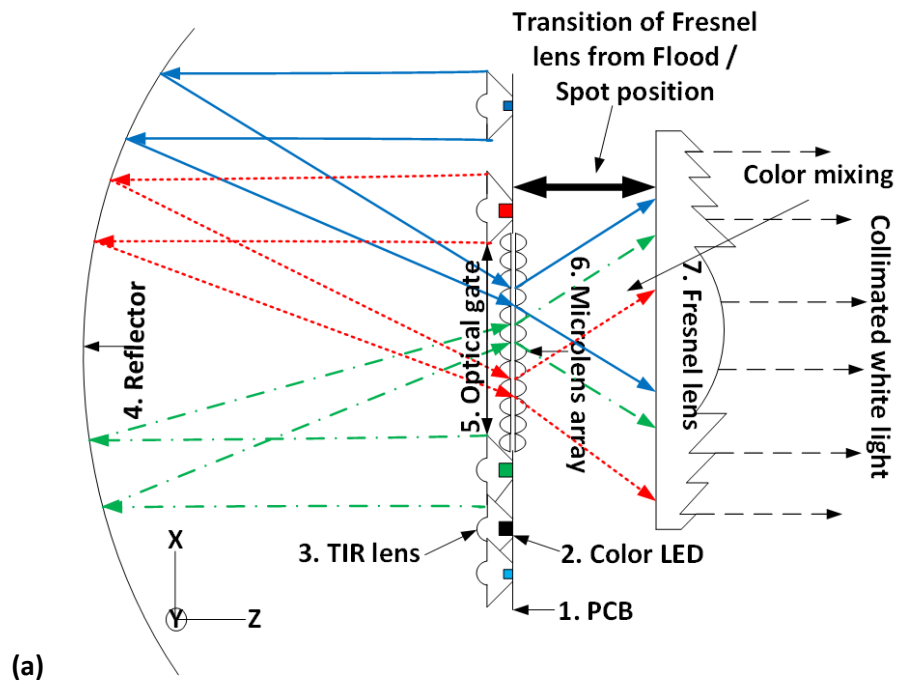
Figure 3-1: (a) Schematic diagram of the V8 light engine design with the position of optical components (not in scale); (b) Seating arrangements of four colored and the white LEDs on the PCB forming seven rings where beams coming from the LEDs are collimated through the individual TIR lenses; (Ref. Figure 1 of Chakrabarti et. al [14])

3.3 V8 light engine components and design optimization

The optimization parameters for the components used in the V8 light engine are listed in Figure 3-2, elaborates on the methods and outcomes from the optimization process.

Optimization components	Optimization parameters	Outcome from Optimization	Optimization tool
1. Printed circuit board (PCB) shape & size	a. Ring numbers b. LED numbers c. LED position	i. Accomodate maximum number of LEDs using minimum space	SolidWorks 2013 x64 Edition
2. LEDs	a. Type b. Size c. Color	i. Maximize the luminous output ii. Maximize color mixing to produce good quality white light	Spectral model (Chapter 4)
3. Reflector	a. Type b. Material c. Shape and size	i. Maximize the luminous output ii. Minimize reflection loss iii. Optimize loss from outer ring of PCB	Radiant Zemax 13 ®
4. Lens	a. Type b. Material c. Shape and size	i. Maximize light extraction ii. Minimize reflection / transmission loss iii. Optimize spread angle and collimation better	Mathematica
5. Optical gate	a. Size b. Position	i. Maximize the luminous output ii. Optimize light collection for beam (> ±40°)	Radiant Zemax 13 ®
6. Microlens array	a. Material b. Shape and size	i. Minimize reflection / transmission loss ii. Maximize acceptance angle iii. Maximize luminous output	Radiant Zemax 13 ®
7. Fresnel lens	a. Material b. Shape and size	i. Minimize reflection / transmission loss ii. Maximize light collection and collimation	Radiant Zemax 13 ®

Figure 3-2: Description of the component optimization order, parameters, outcome, and the process tool

3.3.1 PCB shape and size

The PCB used in V8 is made by two layers using metal core PCB (MCPCB)[62]–[64]. The first layer is made in aluminum. Then there is an isolation layer made by dielectricum[65] on which a copper layer is placed and then a photoresist and etching process is applied. After that, solder mask or solder resist is applied for protection against oxidation and to prevent solder bridges from forming between closely spaced solder pads and finally, it is silk printed. There are six segments to where the color LEDs is distributed in a pattern to optimize the color mixing (Figure 3-3). The LEDs are connected to each other by serial electrical connection to avoid thermal runway by parallel connection. Each LED string has a maximum voltage of 60V/string due to LED driver limitations and high voltage safety regulations.
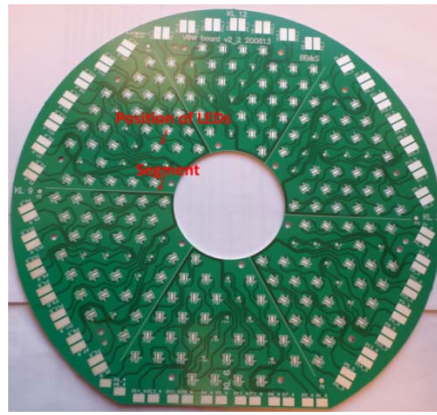
Figure 3-3: The PCB used in V8 distributing LEDs within six segments (made by Brothers & Brothers Sons)

The size and shape of the PCB was designed using SolidWorks in order to accommodate maximum number of LEDs within a given space. The following Figure 3-4 (a) indicates the relation found in terms of PCB size and the LED numbers to be accommodated where y is the LED number and x is the PCB size in mm. Figure 3-4 (b) shows the probable LED position on the PCB.
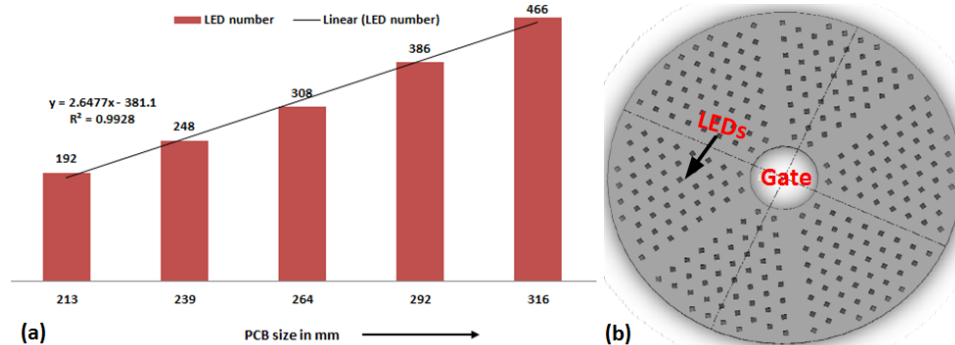
Figure 3-4: (a) The relation between PCB size and number of LEDs to accommodate within the PCB (b) The pictorial indication of LED position on the PCB

3.3.2 LEDs

Keeping in mind of achieving ~20,000 lm of luminous flux, 210 numbers of LEDs are distributed in numbers of 18, 24, 30, 12, and 126 Royal-blue, Blue, Green, Red, and White LEDs, respectively. The different colored LED's are positioned inside the cluster making a pattern (as seen in Figure 3-5) by which the mixture of beams from different colored LEDs provide a good overlap with each other.
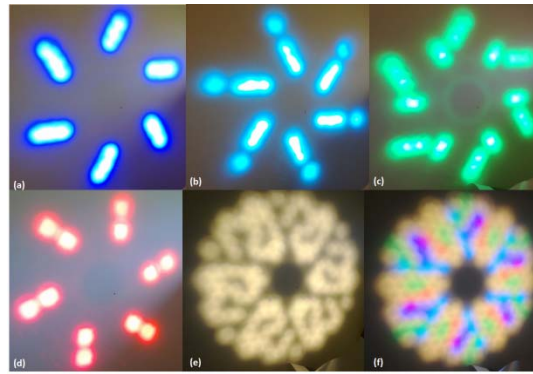
Figure 3-5: Projected light on the wall from the V8 light engine when all (a) Royal-blue, (b) Blue, (c) Green, (d) Red, (e) White, and (f) All LEDs are on at 100% DMX value

Generally, a bared LED has a large viewing angle (~110°-130°), which makes it difficult to tailor the light for processing. Hence, a TIR lens is used on top of each LED to collimate the LED beam coming from the individual colored and white LEDs, which is later focused into the optical gate by the parabolic reflector as seen in Figure 3-1. Chapter 4(Section 4.2.2) and Chapter 6 (Section 6.2) describe more about the LEDs and their properties related to the V8 light engine.

3.3.3 Reflector

The reflector as primary optics inside the V8 light engine plays a significant role to maximize the light output. The light extracted from the TIR lens is reflected and afterwards directed towards the gate by the reflector. To direct almost all reflected beams towards the gate, the important parameters to be considered are: (a) reflector type, (b) shape and size, and (c) material. There are different types of reflectors. Among them parabolic reflector and freeform reflector are popular. A parabolic reflector has the shape of a parabola with the light source typically located at the reflector's focal point. Therefore, the light rays parallel to one another in a symmetrical pattern and can focus the available light into a tight beam. In the parabolic reflector, moving the light source toward the reflector will spread the light, whereas moving the source of light away from the reflector will cause the light rays to converge. The parabolic reflector is utmost efficient in applications that don't require sharp cut-offs; however, allow all of the reflector size to be utilized. Thus, a larger parabolic reflector projects more light for those applications which are not restricted by available installation space. Freeform reflector [66], [67] allows the reflector's surface to be calculated point by point to illuminate certain areas of interest. The design of freeform reflector surface technique has made it possible to achieve a favorable beam pattern solely produced by the shape of the reflector. The investigations on the freeform reflector and the parabolic reflector by simulation are carried out to maximize the light reflection from the reflector. The reflector size and shape are optimized by simulation in order to obtain more light output from the light engine. That means the comparison was made by evaluating the optical efficiency of the simulated light engine by using both types of reflectors (parabolic and freeform). Optical efficiency of a system is generally defined by measuring how much lumens of the total lumens sent into that system come out of it. As

an example, if optical efficiency of a common collimator lens for an LED has taken, it means that first the total lumens of the LED are measured separately in an integrating sphere. As a second step, all the lumens out of this system are measured in the same integrating sphere where the lens to be measured is placed on top of the LED. Finally, the optical efficiency is the ratio of these two lumen values, multiplied with 100, to get out the result in %. In the V8 light design, it is observed in simulation that the parabolic reflector provides higher optical efficiency than a reflector designed by the free form optics. This is because the parabolic reflector in overall delivers higher optical efficiencies for the TIR lenses that are near to the optical gate than the free formed reflector (Figure 3-6). In Figure 3-6, the TIR lenses positioned at first and ninth ring are situated at 6.45 mm and 110 mm away from the edge of the optical gate, respectively while the other ring numbers are situated in between of the first and the ninth ring. However, the optical efficiency decreases gradually for the parabolic reflector when the position of the TIR lens is far from the gate. Irrespective of position of the TIR lens with respect to the gate, the efficiency is constant until the seven ring position for the free formed reflector. As seen in Figure 3-6, at the eight ring position, the efficiency is higher for the free formed reflector compared to the parabolic reflector. This is because the shape of the free formed reflector is optimized in order to receive maximum optical efficiency only at the eighth ring position whereas the shape of the parabolic reflector is optimized to receive over all maximum optical efficiency from the system which is irrespective of the particular position.
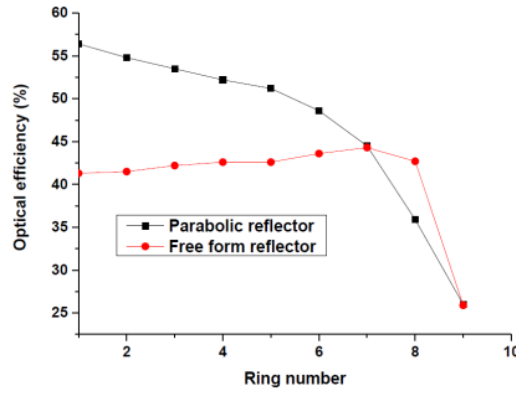
Figure 3-6: Simulated optical efficiency vs LED position in the ring (Ref. Figure 6 of Chakrabarti et. al [14])

   To design a parabolic reflector the basic equation of parabola needs to be considered is equation (31):

$$y = Ax^2 + C \tag{31},$$

where y is the symmetry axis of the parabola, directrix is on x axis and A and C are the constants:

$$\therefore \frac{dy}{dx} = 2\,Ax \tag{32}$$

$$\therefore f = Ax^2 + \frac{x(1 - 4A^2x^2)}{4Ax} = \frac{1}{4A} \tag{33},$$

where f is the focal length of the reflector. From equation (33), we see that the focal length is independent of x and thus all rays parallel to the y axis will pass through the focus after reflecting from the mirror. That also means the off-axis rays, which are not parallel to the axis, will not pass through the focus after reflection. Although the divergence angle of rays coming from LEDs through TIR optics is less ($\sim \pm 5° – \pm 8°$), they are not considered as purely collimated light when they fall into the surface of parabolic reflector. So most of the light reflected from the parabolic reflector cannot meet at the focal point of the parabolic reflector and thus eventually at the focal plane there will be a spread of meeting beams. This is exploited to decide on the gate size from where the final light output is to be extracted. To maximize the light extraction from the gate, the gate is placed at the focal length of the reflector. The parabolic reflected surface is made by two layers. Initially, it is spin coated by hydrogen silsesquioxane (HSQ) and then a physical vapor deposition (PVD) of hard coating of aluminum is applied by sputtering mode[68]. Initially, the process of coating was not good and because of that the light engine had 30% of reflectance loss from the non – uniformity in the reflector. Thereafter, the reflector was modified with a controlled coating of aluminum and the process helped to get a good surface uniformity with reflectance of ~89% (Figure 3-7), which eventually improved an average of 24% in luminous flux output. Although the flatness of the reflector is not a critical parameter for the V8 light engine application, the reflected light variation from different part of the reflector is within ~2%.
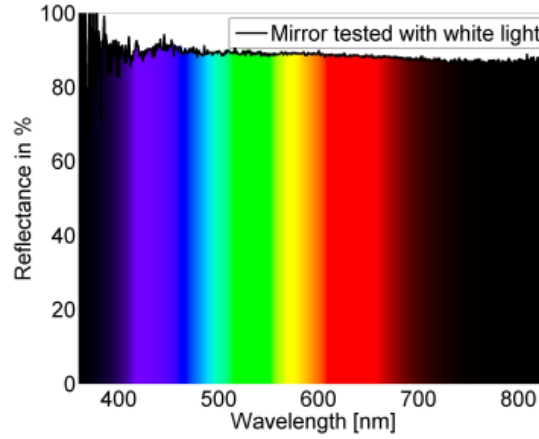
Figure 3-7: The uniform reflectance of the parabolic reflector at visible wavelengths

3.3.4 Lens

The viewing angle of an LED is normally ~110° – 130° which for beam shaping is extremely difficult to work with. Thus, the TIR lens is used in the V8 light engine design, so that when the LED beams incident on the surfaces of the TIR lens, after having several reflections; the transmitted beam can be collimated. However, before using the TIR lens, the collimation from a normal collimated lens is also examined and compared

with the optical efficiency of the TIR lens (Figure 3-8). From the figure it is seen that the TIR lens has almost the same ~78% optical efficiency (higher than collimated lens) at the exit angle from 20° to 70° which is useful for the V8 light engine application.
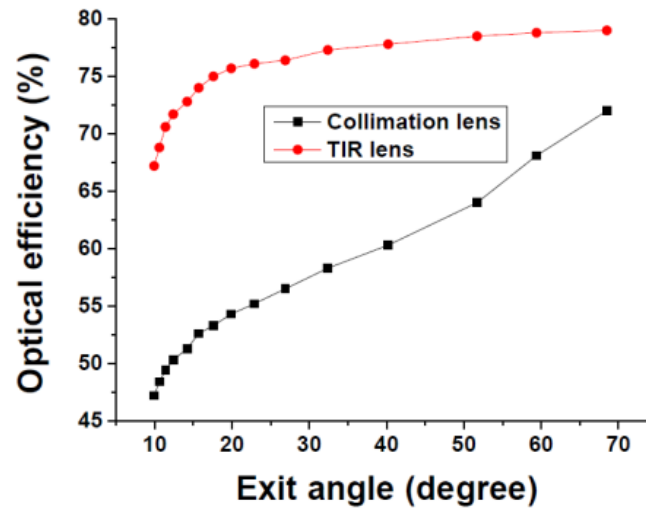
Figure 3-8: Optical efficiency comparison between a TIR lens and a normal collimating lens

The TIR lens is designed by free-form optics using Mathematica where the surfaces of the lens is optimized through a piece-by-piece optimization process considering a point source ray angles ranging from 0° to 90° with a step of 1° in each time. Initially the prototype of the V8 light engine used a TIR lens of dimension 11.7 mm (± 0.2 mm), which later was modified with a bigger size of dimension of 12.7 mm (± 0.2 mm) (Figure 3-9) to improve the overall optical efficiency of the V8 light engine.
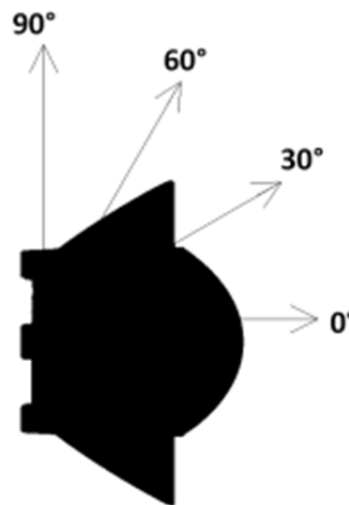
Figure 3-9: The TIR lens showing a point source at 0° and then tilted by 30°, 60° and 90°, respectively

For the two different sizes of TIR lenses, Figure 3-10 ((a)-(b)) shows the experimental optical efficiency for white and blue LEDs according to their position at PCB with respect to the gate. The experimental method is explained in the 6.4 section in Chapter 6. As seen in both figures, the optical efficiency is higher for both LEDs (white and blue) when the system is assembled without a MA. That means that the MA obstructs the light from being transmitted through the gate, which we believe is due to the cutoff angle from the MA. The TIR lenses have a divergence of maximum ±8° with respect to the parallel beam. Due to this divergence, the incoming beam towards the gate after reflection from the parabolic mirror becomes more oblique if the LEDs are situated far from the gate. The viewing angle of the blue LED is higher than for the white LED. Thus, the divergence is also higher for the blue LEDs than for the white. That explains that the optical efficiency of the blue LEDs is always higher than for the white LEDs, while the system is not using a MA. The size of the lens also influences the light extraction from the lens which consequently contributes to the final light output from the system. The Figure 3-10(c) shows the simulated comparison of light transmission between two different sizes of the TIR lenses while a light collecting detector is set at a constant distance. The figure shows that the light transmission from a bigger TIR lens is almost constant for the LED print circuit board size up to 2 mm whereas the LED print circuit board size influences the light transmission for a smaller TIR lens. Thus the optimal lens size of 12.7 mm (±0.2 mm) is used in the modified design. The increased lens size aided to improve the light output from the lens by average of ~56% compared to the prototype. We have optimized the TIR lens size with respect to the illumination from the white LEDs. Hence, there is a maximum of ~50% optical efficiency hike for the white LEDs by using the larger sized TIR lens. The bigger TIR lens also helps the blue LEDs to increase their optical efficiency by ~65%. However, the light extraction from the blue LEDs still needs to be optimized for a higher efficiency which is planned for future research project. Although the MA and the TIR lens size are optimized to enhance the light output from the system, the position of the LEDs with respect to the gate still influences the LED efficiency. Thus, the LED efficiency decreases while going away from the gate which is indicated in the Figure 3-10 (a) (b). However, by using white LED, it is noticed that the transmission from TIR lens with 12.7 mm size is 86%. Therefore, 188 lm light was obtained out of the TIR lens if the driving current of the white LED is 1A.
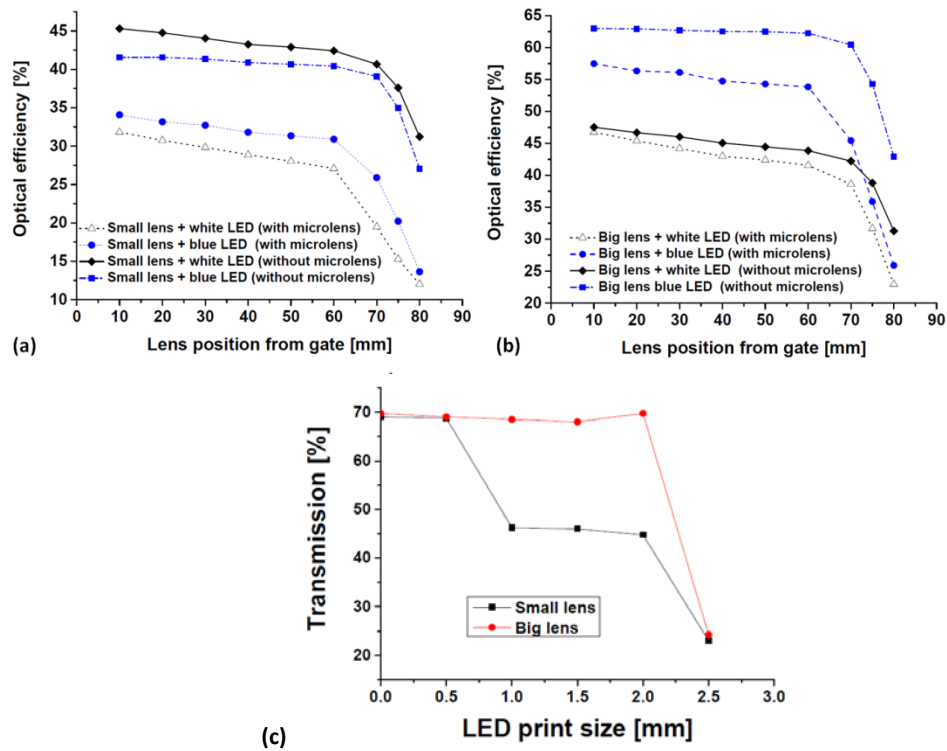
Figure 3-10: (a) and (b) Optical efficiency vs LED position to the gate for small and big TIR lenses, respectively (Ref. Figure 7 of Chakrabarti et. al [14]) (c) Optical transmission from the TIR lens vary according to LED print circuit board size

Further light transmission from different parts of the TIR lens is investigated rigorously by simulation using Zemax. As expected the dispersion of rays at the gate due to marginal rays with regard to the TIR lens is lesser than the central or principle rays (Figure 3-11). Due to the transition of the TIR lens from one surface to another, the rays cannot transit properly leading to unrealistic data results which are disregarded.
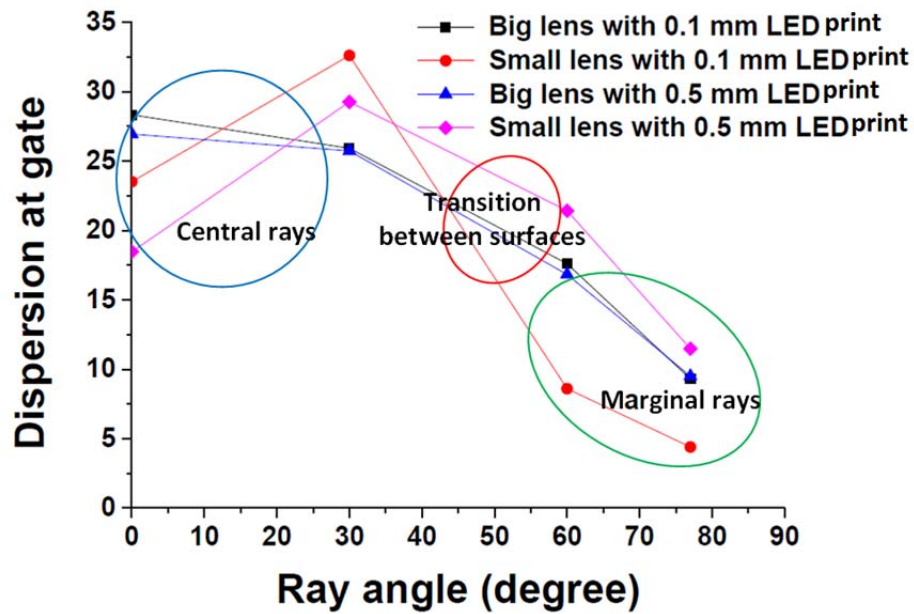
Figure 3-11: Dispersion of ray angles at the gate due to displacement of the ray from a center position of the TIR lens due to LED print circuit board size

In the V8 light engine design, each LED is encapsulated by the individual TIR lens which is also placed on the PCB inserting its 3 legs into the holes in the PCB, and is fixed by applying glue as seen in Figure 3-12 (a). The material used for TIR was Polymethyl Methacrylate (PMMA) and the injection mold technique was adopted to make the TIR lens[69]–[71].

(a)   (b)
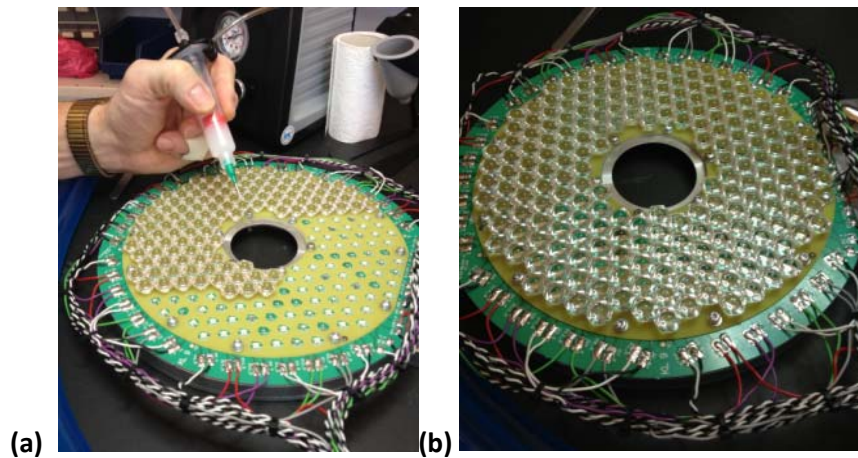
Figure 3-12: (a) The TIR lens is placed by applying glue (b) 210 TIR lenses were placed in the first prototype of V8

3.3.5 Gate

The optimization of the size of the gate and its position with respect to the reflector in order to maximize the light extraction from the output end of the gate (Figure 3-1) is done by using simulations in Zemax. Figure 3-13 shows the simulated cumulative Φ in lm at the output end of the gate while varying the gate size. However, the position of the gate was kept constant which is at the focal plane of the reflector. The figure also shows the total Φ at individual ring position for the aforementioned cases. Although a 55m gate size is having the highest cumulative Φ value, the reflector size needs to be 0.8 times larger than the used reflector size for the gate size of 50 mm which is the second highest Φ contributor. Therefore, the optimized gate size is chosen as 50 mm for the parabolic reflector. Although at the eighth ring position, the free-form reflector provides the highest total Φ, it is seen that the used free-form reflector is having the lowest cumulative Φ value with a gate size of 50 mm.
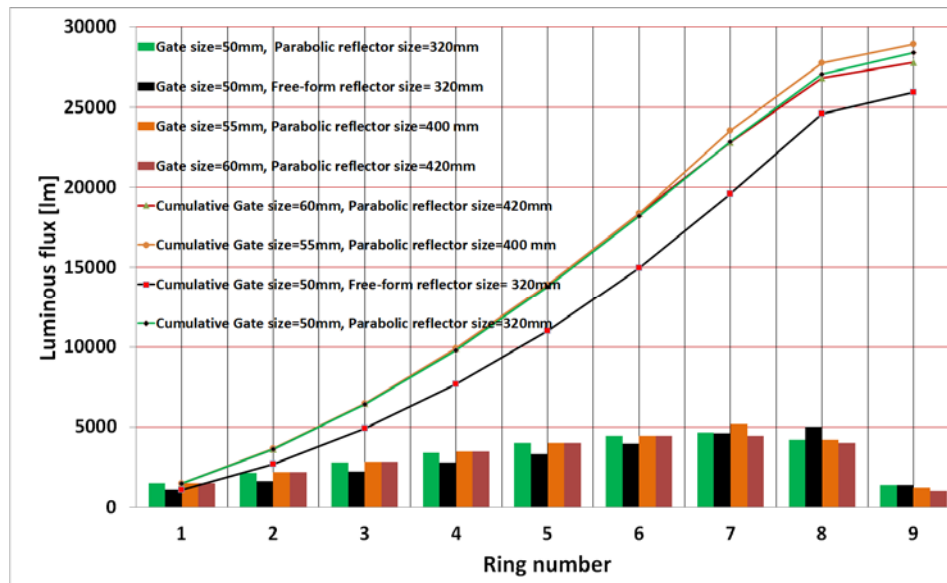
Figure 3-13: Considering the varying gate size, cumulative as well as individual luminous flux for each ring number

3.3.6 Microlens arrays (MA)

The V8 light engine design uses a double-sided hexagonal patterned convex MA, to perform color mixing. The purpose of the MA, called a Kohler integrator[72], [73], is to combine a large number of quasi-collimated beams from the individual colored LEDs entering the MA at different angles into a homogenous color mixed beam.

3.3.6.1 The Köhler Integrator

The Köhler integrator or related illumination system consists of two lens arrays and a condenser lens forming side-by-side multiple Köhler illumination systems as seen in

Figure 3-14. Initially a first lens array shown as LA1 divides the incident light and creates multiple images of the light sources in the aperture plane. The first lens array LA1 also assists as an array of field diaphragms describing the illuminated area in the object plane. The following conditions can apply for the Köhler integrator as explained in Voelkel et. al [70]:

A. The LA1 acting as a collector lens images the light source to the plane of the aperture plane.

B. The aperture plane is positioned in the front focal plane of the LA2 and condenser lens. By this, each point in the aperture plane is imaged to infinity at object plane.

C. The field plane is imaged to the target plane by proper adjustment of the distance from the condenser lens to the object plane.

This adjustment ensures a uniform illumination of both the object and the image plane. In the object plane, real images of the sub-apertures of the LA1 superimpose to LA2. Assuming that the light irradiance is approximately uniform and symmetric over each sub-aperture of LA1, the overlapping of all images provides a uniform intensity distribution in the object plane. Generally, 10x10 microlens arrays are sufficient to achieve good flat-top uniformity. Therefore, in the V8 light engine design, several LEDs act as light sources incident light on the first surface of the double sided MA after reflecting from parabolic reflector. After that the real images of microlenslet array produced by the first surface of MA superimpose to the second surface of MA to constructing uniform illumination. Fresnel lens is used as objective lens.
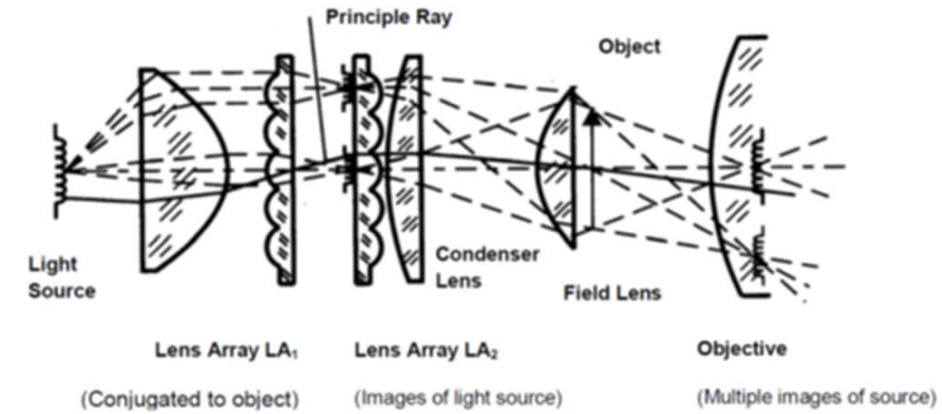
Figure 3-14: Köhler Integrator for uniform illumination (Ref..[74])

As the MA is a critical component for V8 light engine design, the extensive research was done for the lens design and on the fabrication process. Finally a cost effective prototype of the MA was made in-house which is reported through scientific publication[13]. The work was partially funded by the Danish Council for Technology and Innovation under the Innovation Consortium LICQOP, grant #2416669 and The Danish National Advanced Technology Foundation under the V8 light engine project (037-2011-3).

This section along with the following subsections, will describe a novel process, for tool fabrication utilized for injection molding of the microlens structures based on the previously published article by Chakrabarti et. al[13]. The process exploits standard CNC milling to make a first rough mold in steel. After that, a surface treatment is introduced by spray coating with photoresist to obtain an optical surface quality required for MA mold and hence inexpensive injection molding replication process. The fabrication process is demonstrated by the production of ø50 mm double-sided MA designed for color mixing for the V8 light engine. The MA is designed and optimized the lenslet parameters for large angular acceptance angle and the molding tool is produced from these. The MA is then injection molded in PMMA from both the uncoated rough mold and the photoresist coated mold. The injection molded MA are characterized through surface measurement by 3D microscopy. The working performance is observed by angular dependent transmission and investigation of light scattering.

3.3.6.2 Design of MA

Figure 3-15 illustrates the basic functionality of the MA by looking at the ray paths in an optical simulation, using Radiant Zemax® software, for three collimated beams incident on a single lenslet demonstrated by three different colored beams and the microlens array is simulated here with five lenslets. Figure 3-15 (a) shows the color mixing mechanism for collimated beams at incident angles of $0°$, $\Theta_1°$ and $- \Theta_1°$, respectively. The three color beams are all focused on the second surface of the same lenslet. The displacements in position of the focal points in the focal plane are dependent on the incidence angles. The maximum incident angle Θ is governed by numerical aperture (NA) of the lenslet (equation (34)) and is expressed by equation (35). From the second surface the three color beams exit the lenslet in the same direction with the same external divergence half-angle, as Θ.

$$NA = \sin(\Theta) = n \frac{D}{2 * \sqrt{\left(\frac{D}{2}\right)^2 + f^2}} \cong n \frac{D}{2f} \;\; when \; \left(\frac{D^2}{2}\right) \ll f^2 \qquad (34),$$

$$\therefore \Theta = \mathrm{asin}(NA) \cong \mathrm{asin}(n \frac{D}{2f}) \qquad (35),$$

Here D is the width, and f is the focal length of the lenslet and n is the refractive index of the lens material, as indicated in Figure 3-15 (a). Here r is the radius of curvature and t is the separation distance between two opposite lenslet as seen in Figure 3-15 (a), respectively. t needs to be equal to f, so that a collimated beam is focused on the second surface of the lenslet. It is seen that a large divergence angle Θ requires a large numerical aperture, e.g. large n and D compared to f. In the normal operational situation, the incident collimated beams are larger in diameter and hence illuminate a large number of lenslets, and the beams are split into a corresponding number of 'emitters' from each lenslet. Hence, the different colored beams incident at different angles on the MA, are spatially split into a multitude of emitters with equal divergence and direction, and results in a uniform color mixing of the incoming beams.
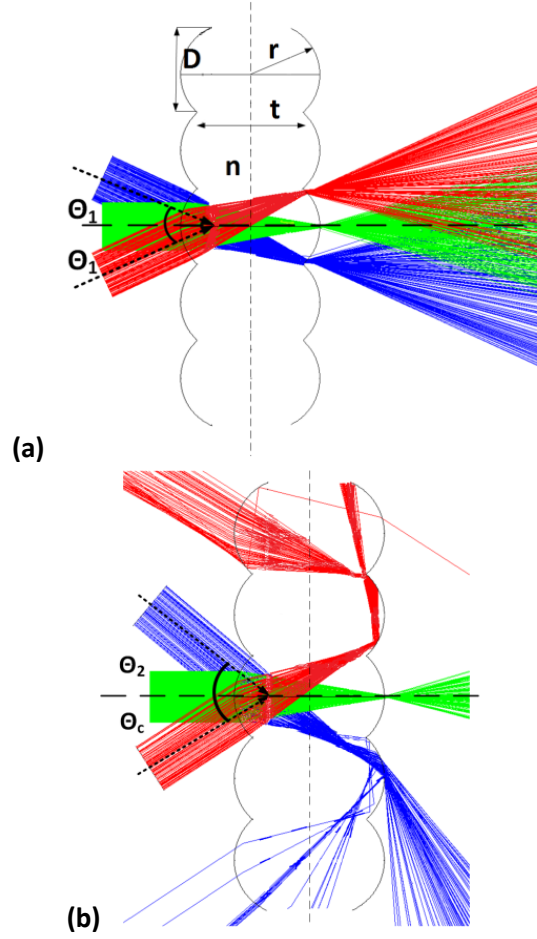
Figure 3-15: Basic color mixing functionality of a double-sided, convex microlens array, with incident beams at angles (a) lower than and (b) higher that the acceptance angle. (Ref. Figure 1 of Chakrabarti et. al [13]**)**

If the incidence angle is larger than the angle Θ given in Eq. (35), the incident collimated beam is focused and coupled into the neighbor lenslet. This is illustrated in Figure 3-15 (b) by the collimated beam coming from below (red rays). It is seen that if the incident angle exceeds the critical angle at the interface of the second lens surface, the beam is entirely internally reflected, where a part of the beam returns in the backward direction. In that scenario, ideally there will be no transmittance from the second surface of the MA. Thus, this angle can be called the cutoff angle, $\Theta = \Theta_c$, or equivalently; the acceptance angle of the MA as within that angle the MA allows beams to be transmitted from the second surface of the lenslet[72]. Figure 3-15 (b) illustrates the case where a collimated beam is incident at an angle larger than the acceptance angle, $\Theta_2 > \Theta_c$ (blue rays). In this case the rays are transmitted in the forward direction from the neighboring lenslet, but at large angles larger than the divergence angle, $\Theta = \Theta_c$. Therefore those rays do not contribute to the effective color mixing within the divergence angle, Θ_c.

According to the above, the transmission of the MA would therefore be high for angles lower than Θ_c and close to zero at this angle, and then increase again at larger angles. Figure 3-15 only illustrates the principle, so in order to get a better idea about the efficiency of the system, a simulation is made of the transmission through the MA using a collimated large beam and varying the incidence angle from 0 to 50°. In order to investigate the output efficiency as a function of exit angle, the simulation is done for a detector that measures the light transmitted, within an exit cone of varying angle. Figure 3-16 shows the transmission efficiency of the MA for the varying incident angles and for varying exit cone half angles. It can be seen that for incidence angles from 0-30°, more than 90% of the light is transmitted when the exit cone half angle is larger than 40°. This corresponds to the case in Figure 3-15 (a), where the beams are incident at angles lower than the acceptance angle and where the exit cone covers the acceptance angle. For incidence angles around 40° almost no light is transmitted within the exit cone of 40°. This corresponds to the case where the incidence angle is close to the acceptance angle as illustrated in Figure 3-15 (b) by the red rays. The top part of the graph in Figure 3-16 corresponds to a large exit cone angle of around 80° e.g. collecting all the transmitted light. Here efficiency higher than 40% is observed for incidence angles around 45°, corresponding to the case in Figure 3-15 (b) (blue rays), however, this transmitted light does not contribute to the mixed light within the divergence angle.
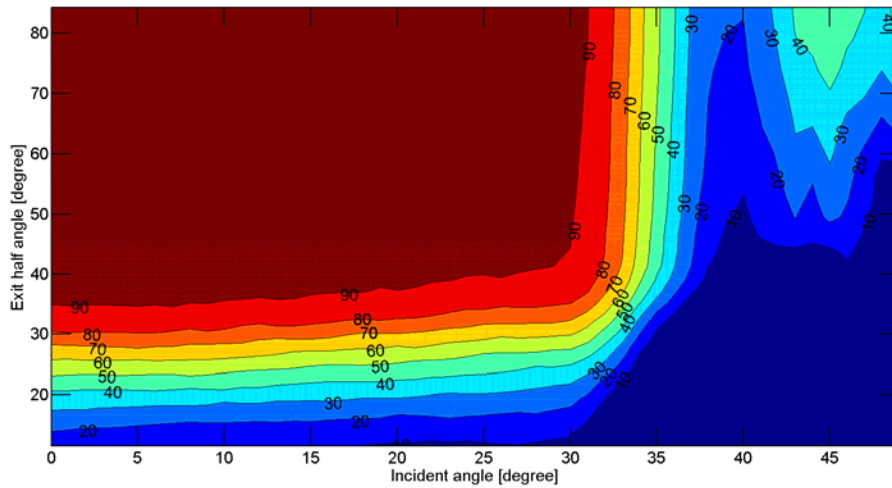
Figure 3-16: Simulated optical efficiency in % of double-sided microlens array as a function of incident angle while exit angle varies (Ref. Figure 2 of Chakrabarti et. al [13])

To achieve a high optical efficiency of the light output from the light engine, the acceptance angle of the MA needs to be optimized. Therefore the MA for the V8 light engine has been designed to have a large acceptance angle. It is seen from Equation (35) that a large divergence angle Θ requires a large numerical aperture NA, e.g. large n and D compared to f. However, the overall transmittance decreases linearly with the increase of n of the material due to Fresnel loss, i.e. reflections at surface air interfaces. Thus there would be a tradeoff between transmittance and acceptance angle. For

injection molding the choices of materials most widely used are poly carbonate (PC) or PMMA. Although the higher n of PC yields a larger acceptance angle than using PMMA, the transmittance is lower. A simulation of the transmittance of the MA for the two different materials have been performed using an incident cone of light integrating over all angles within the cone angle and a large exit cone angle. Figure 3-17 shows this simulated transmittance as a function of the incident cone angle for PC and PMMA respectively. It shows that the transmittance of the PMMA MA is higher than the one using PC for all incidence cone angles. The transmission through PMMA microlens is ~3% higher than for PC at almost perpendicular incidence. PMMA also has ~5% larger efficiency at high incident cone angle of 50°. In our application the transmittance is prioritize and chose PMMA as the material for the microlens fabrication.
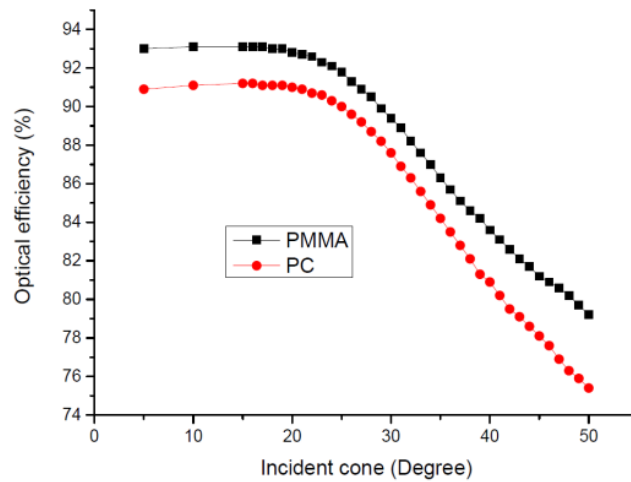
Figure 3-17: Material refractive index dependence transmission for double-sided microlens array as a function of incidence cone (Ref. Figure 3 of Chakrabarti et. al [13])

In order to enhance the optical efficiency in the V8 light engine, the high NA value is also required. The lenslets are spherical with a radius of curvature, r, and the diameter D of the single lenslet varies with the sag [75] which is also responsible to give a spherical shape of the lenslet. A thorough study was done on different lenslet parameters (Figure 3-18) targeting the enhancement of the acceptance angle and finally, the design was optimized by simulation. The Figure 3-18(a) indicates that low $f_{\#}$ yields a high acceptance angle as for low $f_{\#}$ the lens width is high. The high sag provides high acceptance angle raising the lenslet width (in Figure 3-18 (b)). However, when the sag almost appears close to r, the acceptance angle becomes low.

(a)   (b)
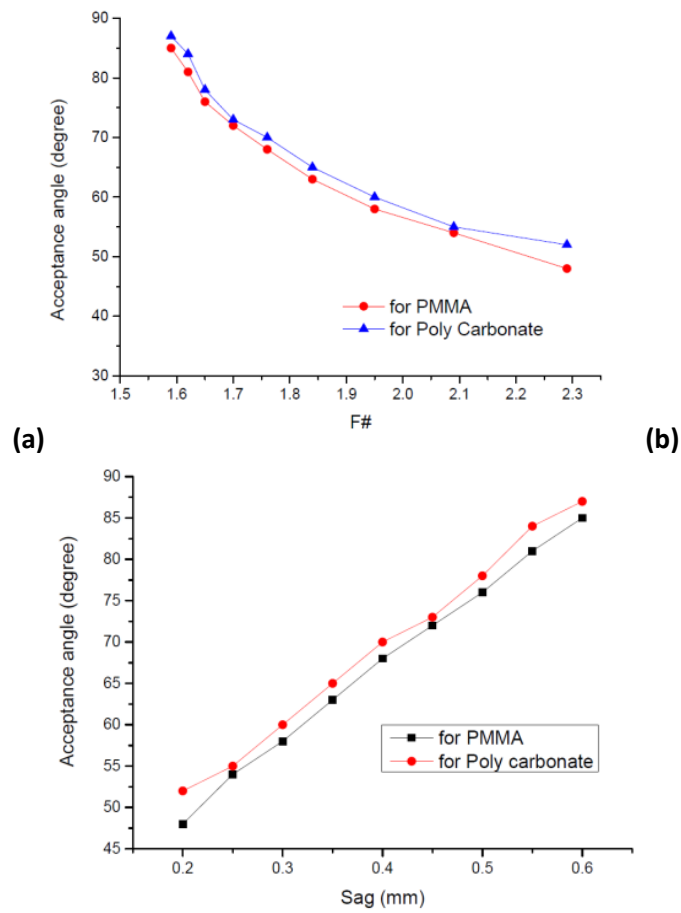
Figure 3-18: The variation of acceptance angle with respect to (a) f$_{\#}$ and (b) sag of the lenslet respectively

The following Table 3-1 describes the designed lens parameters used for the MA fabrication after optimizing the parameters using simulation by Radiant ® Zemax software.

Table 3-1: Lens parameters for fabricated Microlens (Ref. Table 1 of Chakrabarti et. al [13])

Material	Microlens array size [mm]	Total thickness (double sided) [mm]	Lenslet curvature [mm]	Sag [mm]	Lenslet width [mm]	Focal length (mm)	Acceptance angle [°]
PMMA	65	2.1	0.85	0.55	1.45	1.4	82

3.3.6.3 Fabrication process

In this section the fabrication of the double-sided MA is described, from the Computer Numerical Control (CNC) fabrication of mold, the coating procedure with photoresist and the injection molding. Computer numerical control (CNC) machine performs both the functions of drilling and turning machines. CNC mills are categorized according to their number of axis and are conventionally programmed using a set of computer generated codes that represent specific functions. Therefore, the CNC machine was loaded by the computer generated drawing file, made by SolidWorks software, which holds the design optimized lens parameters information (Table 3-1) about the MA. After that the CNC machine inscribes the loaded MA structures on a steel block as shown in Figure 3-19. A similar kind of block needs to be made and held on top of the bottom block. The alignment of the two blocks requires precision so that the positions of the microlens structures in both blocks can overlap each other. As shown in the figure, there is an inlet for injection molding at the edge of the microlens structure. The accuracy of the CNC machine is +/-50 μm.
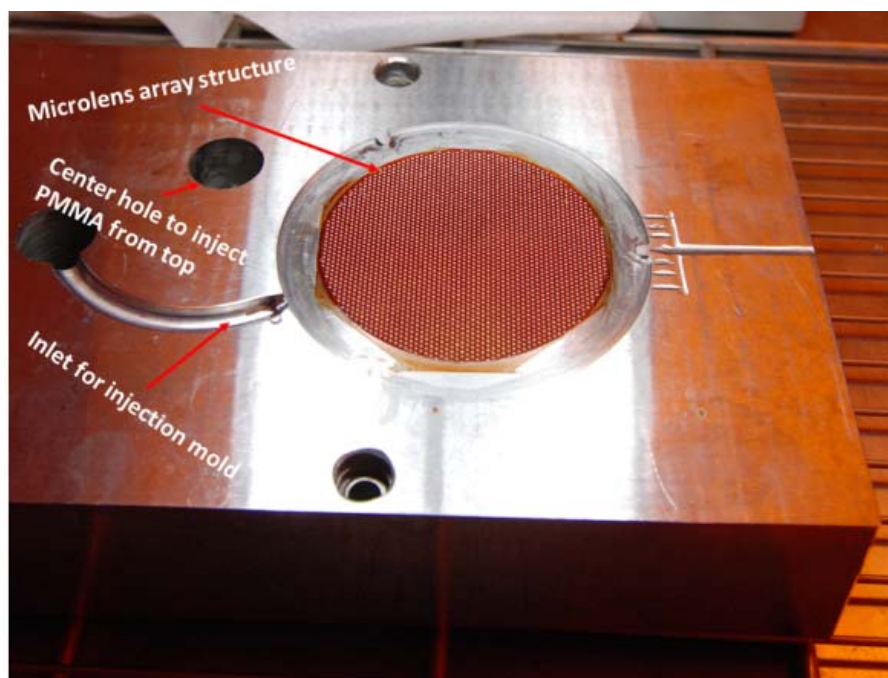
Figure 3-19: Inscribed microlens array structure on a steel block (Ref. Figure 4 of Chakrabarti et. al [13])

The surface roughness of the steel mold can be reduced by photoresist coating. Photoresist is defined as a viscous polymer resin (solution) which contains photochemical active polymer (PAC). There are two types of Photoresist, namely, negative and positive photoresist, respectively. Spin or spray coating is the most

common way of applying Photoresist on wafer or any substrate. Spin coating is not possible for this application and in order to overcome this problem MicroSpray photoresist is used. Microspray[76] is a positive acting, aerosol novolak resist and suits our application. It is cost effective, easy to use and spray eliminates the irregularities and peak–valley variations on the surface of the mold in accordance with the project requirements. For the best use, the Microspray was placed at room temperature (~20°) for an hour prior to use. Before applying, the Microspray needs to be shaken strongly for 10 times and further needs to wait for 5 minutes to remove any air bubbles. Before coating, the steel mold needs to be cleaned by a metal cleaner. After applying the coating, the mold requires to be soft and hard baked. The thermal crosslinking achieved through the hard baking makes the photoresist robust during the injection molding. The block diagram in Figure 3-20 shows the entire coating process.

Clean the steel mold
1.Metal cleaner (DL – 44 and MA - 4000)
2. Iso-Propyl Alcohol (IPA)
3. Blow dry
4. Bake at 110 ° over night
5. Cool down to room temperature

Coat
1. Spray MicroSpray ™ (start 30 cm above vertical from the surface of coating)
2. Coating needs 1 pass with 1m/s speed
(either from left to right or vice versa)

Delay
Need to stay for 5 minute

Soft bake
1. Heat up to110 ° C
2.Stay for 30 minutes

Hard bake
175 °C for 2 & ½ hr.

Figure 3-20: Photoresist process sequence (Ref. figure 5 of Chakrabarti et. al [13])

The coating thickness was inspected through Dektak measurements on a separate sample, to be between 10-14 μm, where the standard deviation of the thickness is ~2.6 %. The polymer PMMA is the best candidate to use as the material for the MA for the application as explained above. It also holds the advantages of the material properties especially the versatile polymeric material is well suited for imaging / non-imaging application. The mold was installed in a standard injection molding machine, in which the second steel block was aligned by dowel pins with 50 micron accuracy and placed on the top of the first block, and PMMA was injected through the center hole of the top block.When the second steel block is aligned precisely and placed on the top of the first block, PMMA was injected through the center hole of the top block. The PMMA was then channelized through the inlet (Figure 3-19). Afterwards a heavy pressure of 2500 bar was applied to the polymer melt. The process cycle of the microlens array is ~20 sec. Melting temperature of PMMA was 210 ℃ and the mold temperature was 70 ℃. Injection molded microlens arrays were produced in the first iteration using the uncoated rough mold. After photoresist coating of both steel molds (top and bottom one) a second

iteration of injection molding of microlens arrays was performed. About 100 microlens arrays were produced without any sign of wear off the photoresist, and without any measurable differences between the item 1 and 100.

The injection molding was performed by the Danish company JJ Kühn.After fabrication of the MA, the surface quality is characterized looking at pre and after coating process result. The lens parameters of the fabricated lenslets were measured by analyzing the array under 3D confocal and interferometric microscopy. The analytical results for surface quality and the quantitative measurement on lens parameters are discussed in Chapter 6 under section 6.6.

3.3.6.3.1 Fabrication process utility

To achieve the high optical surface quality, direct fabrication of lens arrays by diamond turning in polymer materials have been demonstrated [77]–[82]. The advantage of direct diamond turning process is that it is a one step process. However, due to process difficulty and expensive tooling, the fabrication process cost could be in the order of USD 100 – 1000 /mm². Presently, electrostatic-induced lithography [83] and inkjet printing [84] have been explored for direct fabrication of polymer-based shape controlled lenses. The Optical efficiency can considerably reduce due to the large dead space between lenslets. This has been observed in fabricating the microlens arrays which considered initially in this project. Through 3D optical printing process, the microlens arrays are unsuitable for the application.

Since such direct writing processes are not suitable, a way of improving the surface quality of a CNC machined mold is explored and reprted in this thesis. For any replication technique, the critical parameter is the surface quality of the mold which considerably affects the quality of the final microstructures and the applicability for optical components. The CNC machining is easy and inexpensive; however, the surface quality is not good enough for optical components. In many cases the CNC machined mold is polished manually, which is basically tedious, expensive and not applicable for large microlens arrays and also mass production. The procedure of spray-coated hydrogen silsesquioxane coatings to reduce surface roughness was presented recently [85]. This process needs heating the mold part up to 400 °C in an inert gas atmosphere. Such a high temperature may be not useful for the steel molds as some of the steel impurities may segregate and cause embrittlement of the steel.

Therefore the thesis describes a novel process, for tool fabrication utilized for injection molding of microlens structures. To make a first rough mold in steel, the process exploits standard CNC milling. After that a surface treatment by spray coating with photoresist is introduced to obtain an optical surface quality required for microlens arrays. By this way, the expensive tedious manual polishing or shortcoming of direct diamond turning process can overcome. The process also provides an easy and inexpensive mold and hence directs for cheap injection molding replication process. The added advantage is that the coating process only requires a heat treatment of the mold part up to 175 °C.

3.3.7 Fresnel lens

An off-the-shelf positive focal length Fresnel lens is used at grooves-in position in the V8 design. The grooves are with constant width. The Fresnel lens is made by colorless Borosilicate glass with Ø250 mm and focal length of 100 mm which is able to capture all light output emerging from the output end of the gate with a maximum oblique angle of ±40° and provide the required collimation to produce spot light for the V8 light engine (Figure 3-21). The transmission loss from the Fresnel less is ~8%. Future Fresnel lens will be made from PMMA Acrylic which is discussed in Chapter 7.

Figure 3-21: Fresnel lens made by Borosilicate glass

3.3.8 Electronic Driver

Presently, the digital multiplex signal (DMX) 512-A[86] universe is used in the V8 light engine to control the electrical power input to LED channels using a DMX Decoder/Driver. DMX512-A is the current standard and is maintained by ESTA (Entertainment Services and Technology Association). The DMX 512 signal is a set of 512 separate intensity levels (channels) that are constantly being updated. One single V8 light engine requires 4 channels. However, it is a one way communication and as a lighting desk it can handle several similar V8s by using a distinct address from 1-512, each level has either 8 bit (2^8 =256) or 16 bit (2^{16} =65536) steps divided over a range of 0 to 100 percent. As an example if we take 12 similar V8s, then the total channels required would be: 12*4 = 48 channels, where the second V8 light engine will start from the fifth channel and so on. Presently, new DMXRDM is available in the market which has extended the DMX as it supports limited bi-directional communication.

In the prototype of the V8 light engine, there are 206 LEDs which need ~ 666 W electrical powers to drive the LEDs under a full load. The LED driver utilizing the boost from Linear Technology creates DC current with triangular current ripple of 10% with a frequency of 500 KHz., which is the reason there is no flickering observed and that is why it is better than switching ON/OFF in pulse width modulation (PWM). Step-Up (Boost) regulator LED drivers generally produce the high voltages crucial to drive multiple LEDs in series, confirming current and therefore brightness matching between the LEDs. The advantage of boost regulator LED drivers from Linear Technology is that they offer the highest efficiency, lowest noise, and the smallest footprints. Other features include integrated Schottky diodes, which provide accurate LED current matching and multiple output capability. To facilitate the dimming effect, the V8 light engine uses a personalized file of virtual dimming, which is square dimming calculated out of linear dimming as a compensator. A square law dimming applies a multiple derived from the

square root of the control level (with full output equal to 1.00) to increase voltage response at low control levels to compensate for the infrared loss.

3.3.9 Heat sink

A heatsink is a device that is attached to a lighting device to keep it from overheating by absorbing its heat and dissipating into the air. Generally to avoid the failure from the components, any device temperature should not run in excess of 50-55 °C while under a full load. Especially for luminaires made by an LED module is sensitive to the temperature. Thus, water cooling is used in the prototype of the V8 light engine to transport heat from LED module to the outer surface of the V8 light engine so that excess heat can be dissipated and also maintain the water temperature at 10 °C. Although water cooling is very effective, it is inconvenient for handling. Thus, in future a proposal of using a heat pipe as well as an electric fan is discussed in Chapter 7. For theater application, noise from fan can be an issue.

3.4 Optical modelling in Zemax

The purpose of doing optical simulations of the optical design is to provide design flexibility and optimization of light throughput. It also helps to finalize the position and size of the optical components. Optical simulation of the V8 light engine design has been done using Zemax optical software. As the V8 light engine is a complicated system to simulate, initially as an example; the geometrical simulation of a simple optical system based on the color mixing of three LEDs is considered, which is documented by Chakrabarti et. al in scientific article[16]. The article describes the investigation and optimization procedure for the angular distribution of the luminous intensity as well as the color distribution, considering a 3D geometrical ray–tracing model of the LED optical system using the optical modelling software Zemax. The result of the angular distribution is analyzed for luminous intensity and homogeneity of chromaticity and CCT. The three LEDs are modelled by using ray source files provided by the manufacturers with 500,000 rays in each, and the measured SPD for the LEDs are included as spectral weights for the rays. The reflectance of the Ba_2SO_4 coating is modelled by using the Lambertian scattering model. The three colored LED system also used a diffuser plate (5 mm x 5 mm x 1mm). The diffuser helps to create homogeneous color mixing from the tri-color LED system as explained by Chakrabarti et. al[16]. The bidirectional scatter distribution function (BSDF) of the diffuser has been experimentally measured and the scatter model data is included in the model. Appendix B shows the technique of the BSDF calculation. A virtual polar detector is used to analyze the spatial light distribution. This is done by summing up the number of rays hitting the angular spaced detector elements. From this analysis, the luminous intensity distribution and the tristimulus values of the light for the different angular directions can be found. By adjusting the radiometric power of each LED ray emitter, the model to the specific optimized settings is able to tunable through the found settings of spectral mapping. The chromaticity coordinates are calculated from the angular spaced data for the tristimulus values of the polar detector, and they are used to calculate the CCT of the light in directions corresponding to the Θ and φ angles, where the Z-axis is considered as the optical axis, corresponding to $\Theta = 0°$, where the origin is at the center of the optical model (Figure 3-22(a)). The X axis is given by $\varphi = 0°$ and $\Theta = -90°$, respectively.

To simulate the V8 light engine design, a similar method is adopted. To represent the parabolic reflector and the TIR lenses, corresponding CAD files are loaded as *.stl* files. The material of the TIR lens is defined as the PMMA while the reflector is defined as a mirror where reflection losses are considered. The other optical components (e.g., PCB, gate, MA) are defined as Zemax objects. Initially, the design consisted of 7 rings on which 210 LEDs were placed as seen in Figure 3-22. The ray files for the LEDs are loaded into the Zemax file from the respective source files which is available from the corresponding supplier's websites. Each colored LED with their respective ring position was simulated separately through the TIR lens to investigate the radiation loss as well as the total light output from an individual scenario of color tuning between 3000 K and 6000 K. However, to ease the simulation process for the entire V8 light engine, instead of simulating 210 LEDs, one white LED with an individual TIR lens at each ring is considered. This method saves computational time as well as reduces the complexity. The ray file with 500, 000 rays for white LED are loaded into the Zemax file from the respective source file. The total light output was finally estimated by considering the other colored LEDs with their respective position in the ring and their corresponding light output. The total light output from the simulation was investigated by placing a virtual detector as a screen at a 5 m distance from the optical gate where the exit cone was ±40°. Figure 3-23(a) represents the simulated beam spot from the V8 light engine while the light is projected at a 5 m distance. The figure indicates that the light output has a homogeneous intensity in the middle except for one red spot and then it gradually fades out towards the perimeter. As mentioned earlier, the simulation is done by considering few white LEDs inside the optical design; the light output cannot be uniformly distributed and shows the highest intensity where beams from the white LEDs influence the most. The beam spot has hexagonal shape, which is because of the hexagonal shape of the MA. The issue is discussed in Chapter 7 under section 7.2.1 and the shape is experimentally validated (Figure 6-25).
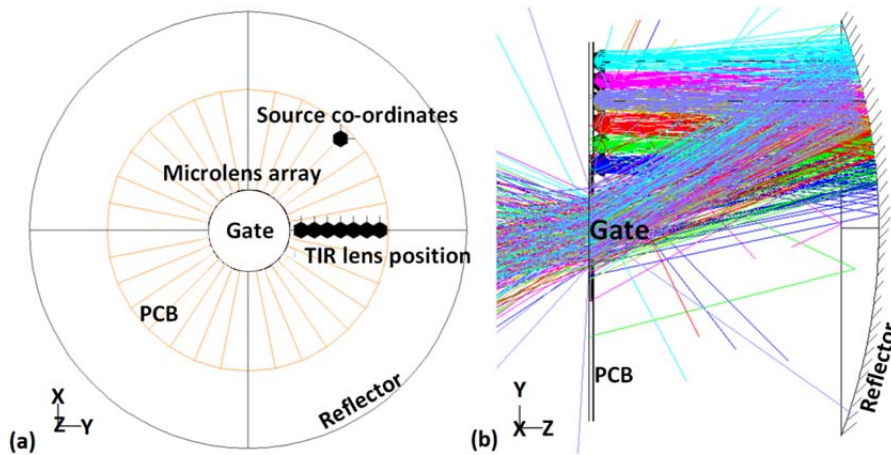
Figure 3-22: (a) Top view of TIR lens position on the PCB in simulation software (b) Color mixing light coming out from the gate (Ref. figure 3 of Chakrabarti et. al [14]

When the total light output was estimated by the simulated system, the spectral information such as the CCT of the light was unable to be investigated. Thus, there is no scope of tuning the CCT ranging from 3000 K to 6000 K by the simulation. However, 4350 K white light was simulated by mixing of few color LEDs inside the light engine and the color homogeneity is observed by checking the viewing angle ($\Theta = \pm 50°$). The two planes XZ and YZ are considered where XZ represents $\varphi = 0°$ and YZ represents $\varphi = 90°$ (Figure 3-23(b)). The variation in CCT is maximum $\sim 4\%$ within $\Theta = \pm 50°$.
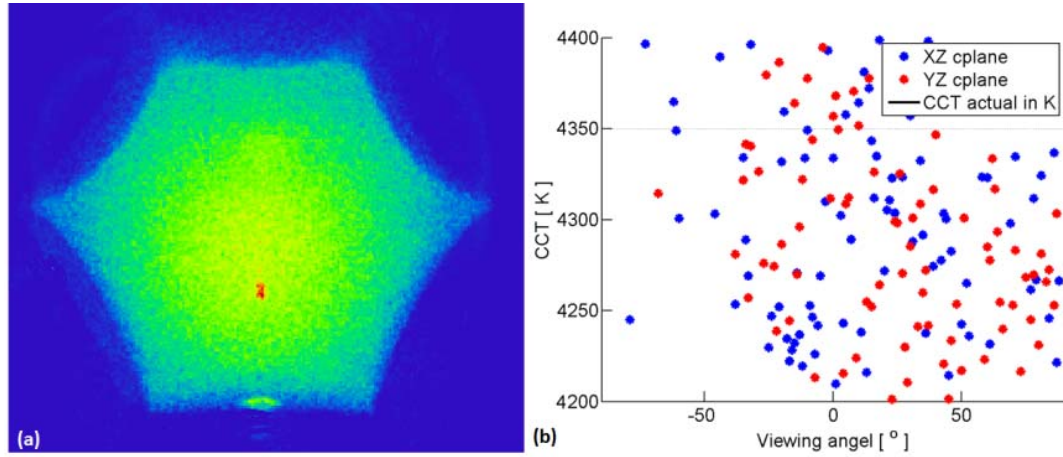
Figure 3-23: (a) Simulated light output from the V8 light engine when the virtual detector is placed at 5 m from the gate (b) Simulated white light at 4350 K from the V8 light engine

The beam homogeneity of the white light output is also checked by simulating an optical design using Unified Optical Design software (Wyrowski VirtualLab Fusion) from LightTrans UG, where the collimated beam from Red-Green-Blue(RGB) LED print circuit boards (coming from different angles) are directed towards the MA [87], [88]. One virtual detector is placed at 5 m from the MA so that the project light creates the beam spot. Figure 3-24 represents the beam spot where the beam size along the X and the Y directions are same ($\sim \pm 2.5$ m). The spot looks homogeneous in the middle and shows the chromatic aberration at the periphery due to the dispersion of light. This issue is discussed in 7.2.1 in Chapter 7. The beam spot shape is hexagonal due to the shape of the MA.
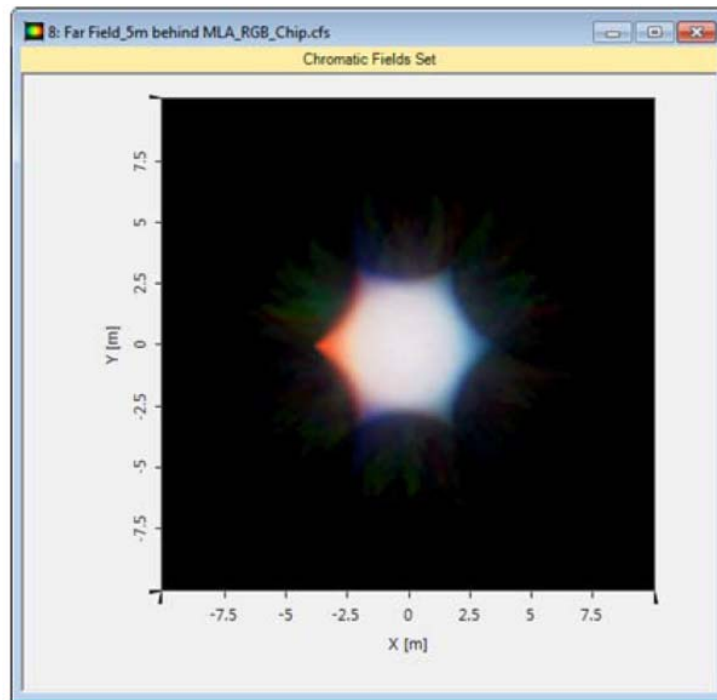
Figure 3-24:, White beam spot created by color mixing of RGB LEDs using the MA projected at 5 m distance (Ref. [87], [88]**)**

The parameters of the reflector, the TIR lens and the MA have been optimized with respect to obtaining a high light throughput from the optical gate. The section 3.3 has already discussed the benefits of the optimization.

3.5 Optical component parameters for V8 light engine design

The dimensions of the individual optical components along with the LED numbers used in the optical design of the prototype of the V8 light engine are listed in Table 3-2. To obtain higher light output from the optical system, Table 1 also indicates the optimized dimensions of the corresponding optical components.

Table 3-2: The dimensions of the optical components in the V8 lighting design (Ref. [14])

Optical system	Numbers		Parabolic reflector [mm]			PCB size [mm]	Lens size [mm]	Gate size [mm]	Fresnel lens size [mm]	MA width [mm]
	LED	Ring	Diameter	Curvature	Focal length					
Original Prototype	210	7	240	-380	170	206	11.7±0.2	50	250	1.2
Modified design 1	210	7	240	-330	165	206	12.7±0.2	50	180	1.45
Modified design 2	288	9	340	-400	180	270	12.7±0.2	50	180	1.45

The luminous efficacy of the white LEDs at each ring position is simulated according to the modified design 1 (Table 3-2). Figure 3-25 directs the cumulative luminous flux at each ring after adding the total light output from the LEDs at each ring position. The individual luminous flux decreases gradually as the ring number increases (far from gate). However, the cumulative luminous flux increases initially with increasing ring number. This is because the ring size increases gradually giving room to hold more LEDs than the previous one. After ring number 7, the cumulative luminous flux again decreases as the high TIR lens loss cannot compensate the effect of increase in LED number. The figure indicates that the total luminous flux from the V8 light engine is ~25900 lm before Fresnel lens. The average deviation in optical efficiency of the light engine between the simulation and experimental results is ~9.7%, which is discussed in section 6.7.1 in Chapter 6.
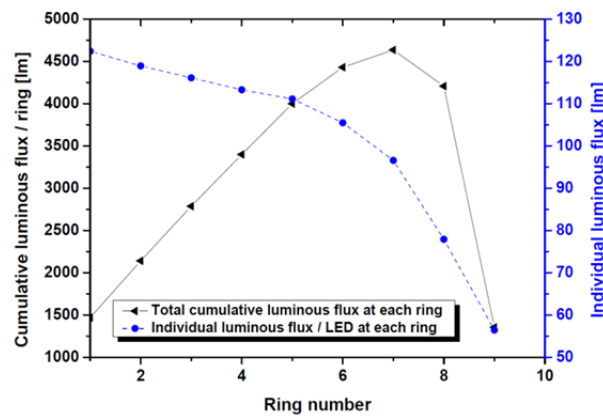
Figure 3-25: Cumulative luminous flux and individual luminous flux at each ring respectively (Ref. Figure 7 of Chakrabarti et. al [14]**)**

3.6 Summary

This chapter introduces the V8 light engine by defining the components and their respective functionalities to produce a desired white light output from the V8 light engine, which has a stage application. The geometrical design of the V8 light engine is optically simulated using Zemax and used optical components are optimized in order to yield > 20,000 lm light output from the light engine, which is one of the critical goals of the project. The MA used inside the V8 light engine design as a beam homogenizer is designed for this application to maximize the optical efficiency. It is fabricated in house and characterized for the lenslet parameters, surface quality, light scattering, and acceptance angle. The fabrication process of the MA overcomes the expensive and tedious manual polishing or direct diamond turning. The process provides an easy and inexpensive mold and hence inexpensive injection molding replication process by far. The final dimensions of the used components are documented in a table. The simulated light output indicates that the V8 light engine is capable of producing a luminous flux of >20,000 lm. The following chapter will be about the color mixing technique and the application in the V8 light engine design required in order to get an effective color mixing with good light quality.

Modelling of color mixing

'Every so often change your palette. Introduce new colors and discard others. You will gain knowledge of color mixing and your work will have added variety.' – Kenneth Denton
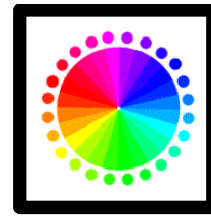
Chapter 4 : Modelling of color mixing

4.1 Introduction

This chapter will provide the basic insight of the color mixing technique adopted in the modelling of color mixing for the V8 light engine. Since the V8 light engine collimates and combines the light beams from a number of colored high power LED arrays into a single focusable beam, the system needs to mix the individual colored LEDs including white LED in adept way so that the resultant of the color mixing would cover a large color gamut area and at the same time cover a range of white light corresponding to different color temperatures which should be characterized by high color rendering properties. Other critical requirements for the V8 light engine are; (1) the resultant white light needs to be free from color shadows, (2) focusable spot light output. However, initially the color mixing of laser light has been investigated, as spot light can easily be made from laser light due to the collimated nature[12][89]. The laser has a much narrower spectral linewidth than the broad spectrum of light emitted from LEDs. Thus during color mixing time, LED spectrums have capacity to overlap each other while laser spectrums rather stay discrete after mixing. Therefore, the white light produced by the laser could provide discomfort in a visual perception of color while seeing the color objects which does not attract the people preference. It could affect the color rendering of the overall light output. Secondly, LEDs are a cost effective solution compared to laser. For an example, a green laser of 1 W provides ~ 600 lm, whereas a blue laser of 1W provides ~20 lm, and a red laser of 1 W provides 219 lm luminous flux[90]. Thus, to obtain a 20,000 lm light output from the V8 light engine, we need more than 20 lasers [91]which are costly compared to the price of an LED. Hence, the color mixing from the LED illuminations were used for designing the V8 light engine.

4.1.1 Color mixing technique

White light can be generated by proper mixing with red, green and blue LEDs[8], [92], [93]. But nowadays people prefer to use an additive color mixing method where more than three LEDs are used to generate the desired white light[94]. The white light can also be produced by the different colored LEDs with white LEDs itself. The advantages

of using this additive color mixing method are to achieve as high a color rendering as possible, and as low a chromatic distance to the Planckian locus. In this context, it is assumed that the power distribution of the LEDs is much narrower than the variations in any of the three color matching functions ($\bar{x}(\lambda)$, $\bar{y}(\lambda)$, and $\bar{z}(\lambda)$). The chromaticity coordinates of the multi-colored light (e.g. three components of light) are in a linear combination of the individual chromaticity coordinates weighted by the L_i (i=1,2,3) factors where P_i (i=1,2,3) is the corresponding optical power emitted by the sources and ($\bar{x}(\lambda_i)$, $\bar{y}(\lambda_i)$, and $\bar{z}(\lambda_i)$) are the color matching functions corresponding to the peak wavelength in the equations (36) - (38) [95].

$$L_1 = \bar{x}(\lambda_1)P_1 + \bar{y}(\lambda_1)P_1 + \bar{z}(\lambda_1)P_1 \tag{36}$$
$$L_2 = \bar{x}(\lambda_2)P_2 + \bar{y}(\lambda_2)P_2 + \bar{z}(\lambda_2)P_2 \tag{37}$$
$$L_3 = \bar{x}(\lambda_3)P_3 + \bar{y}(\lambda_3)P_3 + \bar{z}(\lambda_3)P_3 \tag{38}$$

Using the abbreviations, the chromaticity coordinates of the mixed light can be calculated from the tristimulus values to yield (x, y) coordinates in equations (39) - (40).

$$x = \frac{x_1 L_1 + x_2 L_2 + x_3 L_3}{L_1 + L_2 + L_3} \tag{39}$$

$$y = \frac{y_1 L_1 + y_2 L_2 + y_3 L_3}{L_1 + L_2 + L_3} \tag{40}$$

Figure 4-1 (a) shows the example of three color mixing LEDs producing resultant SPD of white light (2200 K) on the Plankian locus and corresponding CIE 1931 (x, y) chromaticity diagram at Figure 4-1(b).
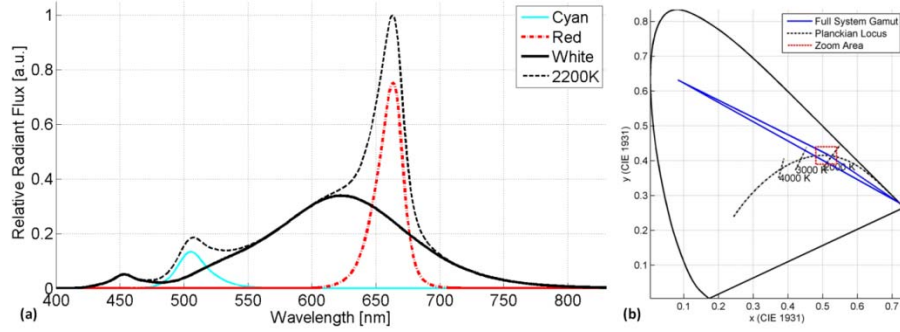
Figure 4-1: (a) The resultant spectral power distribution (dashed line), and spectral power distributions of the individual LEDs (cyan, white and deep red) normalized to the peak of the resultant SPD (b) CIE 1931 chromaticity diagram for the tri-color LED optical system where solid blue line of triangle shows the full gamut of the LED system, white (2152 K)-cyan (502 nm) – deep red (666 nm) (Ref. Chakrabarti et. al [16])

4.2 Color mixing portfolio for V8 light engine

The V8 light engine uses the method of additive color mixing of four colored LEDs and a warm white LED with their specific SPDs, where resultant 'SPD' represents the linear summation of SPD(λ) per unit wavelength emitted for the entire range of wavelengths

from 360 nm to 830 nm. It is believed that the adding of power of light emitted per unit wavelength for each LED will produce a more accurate resultant SPD than adding only SPD (λ_P) at λ_P of each LED, where λ_P is the peak wavelength of each colored LED. Moreover, since the white LED is used as the mixing color component, for the white LED, there will be an uncertainty of finding the precise peak wavelength within the broad spectrum. Thus, equations (36) - (38) cannot be used to simulate the resultant tristimulus functions of the produced white light output. To find out the resultant tristimulus function of the produced white light, the following equations need to be derived. Let us assume that $S_1(\lambda), S_2(\lambda), ... S_5(\lambda)$ [96] are the spectral power distributions per unit wavelength for the five LED components. The resultant spectral power distribution 'S(λ)' per unit wavelength can then be calculated by equation (41).

$$S(\lambda) = S_1(\lambda) + S_2(\lambda) + S_3(\lambda) + S_4(\lambda) + S_5(\lambda) \qquad (41)$$

The tristimulus values from equation (41) are given by the equations (9)-(11), where $\bar{x}(\lambda), \bar{y}(\lambda), \bar{z}(\lambda)$ are the color matching functions at corresponding wavelength. From tristimuls value, CIE 1931 (x, y) chromaticity coordinates can be calculated by using (12) - (14). Finally, from CIE 1976 (u', v') [97] and CIE 1960 (u, v) uniform chromaticity coordinates can be derived from the equations (17) - (18).

4.2.1 Spectral modelling

To realize and analyze the above mentioned method, the spectral mixing of a simple tri-color LED optical system has been used as a tool of LED spectral modelling which is documented in the article of chakrabarti et. al[16]. Instead of a tri-color system, the V8 light engine is designed for five different color LEDs. However, the basic methodology was implemented in a same manner. The basic methodology for the tri-color optical system is elaborated in the following paragraph.

Spectral modelling of the light output has been performed by extensive mapping of the possible resulting SPD of the LED optical system. The goal of this was to obtain white light with a low D_{uv} and a good color rendering at low CCT with commercially available LEDs. For color rendering, the thesis considers mainly the general color rendering index, R_a, and the widely used supplementary specific CRI for red objects, R_9, as well as other metrics, R_{10} and CQS. Similarly to Corell et al[98], it is assumed that this could be obtained in the tri-color system by using a cyan LED to fill the gap between the blue and the green spectral regions in the SPD and by using a red LED to adjust the red spectral content. This assumption was verified by the simulation method shown in this section. There is a tradeoff between the simplicity of the tri-color system and broader parameter range of color qualities of white light from the tri-color LED system over a system with more than three colored LEDs. This mapping method is based on the spectral characterization of the individual LEDs which is modified from reference [99] and described more thoroughly in reference [100]. The results are visualized as an overview of the colorimetric possibilities and make the identification of individual settings for the LEDs with suitable color characteristics easily accessible. This simulation is not in itself optimized towards a single parameter; however, it is carried out in an exhaustive numerical mapping of all the possible color characteristics that the system can produce. This is done by simulating a constant current setting (700 mA) for the warm white LED and then calculating the colorimetric results from different scaling

combinations [Equations (42) and (43)] of the red and cyan LEDs using additive color mixing.

$$\Phi_{red}(\lambda, \alpha_{red}) = \alpha_{red}\Phi_{red,0}(\lambda) \qquad (42)$$

$$\Phi_{cyan}(\lambda, \alpha_{cyan}) = \alpha_{cyan}\Phi_{cyan,0}(\lambda) \qquad (43)$$

where Φ_{red} and Φ_{cyan} are radiant flux, α_{red} and α_{cyan} are scale factors, λ is the wavelength and $\Phi_{red,0}(\lambda)$ spectral radiant flux at 300mA, $\Phi_{cyan,0}(\lambda)$ spectral radiant flux at 90mA from LEDs for equation Equations (42) and (43), respectively. The resultant SPD is obtained by adding contributions from the three LEDs (Equation (44).

$$\Phi(\lambda) = \Phi_{white}(\lambda) + \Phi_{red}(\lambda, \alpha_{red}) + \Phi_{cyan}(\lambda, \alpha_{cyan}) \qquad (44)$$

where $\Phi(\lambda)$ is the resultant spectral radiant flux of the three combined LEDs and Φ_{white} (λ) the spectral radiant flux for the white LED at 700 mA. The resulting maps of the general CRI, and specific CRI R_9, CCT, and D_{uv} can be seen in Figure 4-2. Using this method, the mapping of the characteristics to a two–dimensional problem reduces, that can be calculated relatively fast for the whole parameter space. Finding optimal solutions for color characteristics can then be done by searching for the desired characteristics within the available gamut area of the LED optical system. The main focus was on the solutions where the chromaticity is closest to the Planckian locus, i.e. the lowest possible D_{uv} with high color rendering. Figure 4-2 shows the result of the calculation where the horizontal and vertical axes of the four subplots are α_{red} and α_{cyan} for red and cyan respectively, whereas the white LED is kept at a constant scaling value. The optimization of the LED settings for the desired CCTs is discussed in the following paragraph.
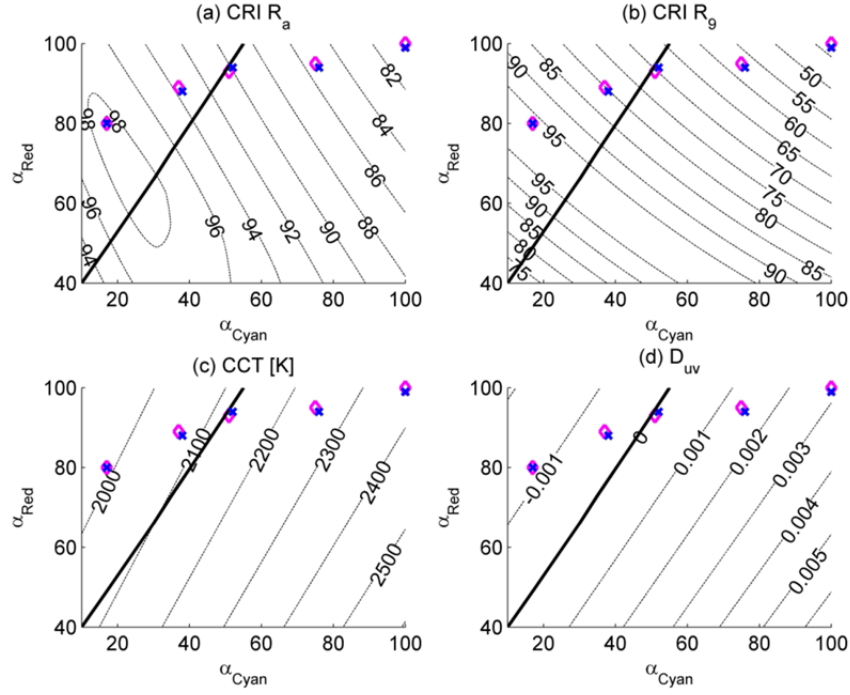
Figure 4-2: Spectral mapping of the possible color characteristics of the optical system. Mapping of the general CRI R_a(a), special CRI R_9 (b), CCT (c) and D_{uv} (d) for varying content of red and cyan LED light in the LED optical system. Experimental validation results are represented by 's' while 'x' shows the locations of simulations with corresponding CCT and D_{uv} values from the exhaustive numerical simulation. The solid thick black line represents parameter sets which have zero D_{uv}. From Figure 4-3 (c), the black line corresponds to a narrow CCT range from 2094 K to 2106 K (Ref. Figure 4 Chakrabarti et. al [16])

    The spectral modelling produces the mapping of the colorimetric parameters CRI R_a, CRI R_9, CCT and D_{uv} for relevant settings of the α_{cyan} (20% to 100%), α_{red} (40% to 100%), and constant warm white LEDs as shown in Figure 4-2. The optimal settings of all abovementioned colorimetric parameters are found. CRI R_a and R_9 are mapped with the spectral content of a deep red LED versus the spectral content of the cyan LED according to Figure 4-2(a) and (b), respectively. The specific CRI for golden objects as yellow objects, R_{10}, is equally important. However, a close correlation in the spectral mapping between the R_{10} and R_a was found and hence only graphs for R_a and R_9 are shown. The CQS shows a similar correlation with R_a. The interesting observation is that the optimum CRI regions, where both $R_a > 95$ and $R_9 > 90$ appear as lines with a negative slope of α_{red} and while α_{cyan} is limited up to 40% for R_a and 80% for R_9, respectively. The maximum achievable R_a and R_9 by spectral mappings are 98.6 and 99.9, respectively.

    As seen in Figure 4-2(c) and 4d, both CCT and D_{uv} levels increase with a negative gradient across the map. Figure 4-2(c) presents CCT mapping where the intended CCT ranges from 2000 K to 2400 K could be achieved by linearly increasing scaling factors of

both cyan and deep red. In order to reach 2000 K, α_{red} should be 80% and the corresponding α_{cyan} 20%. At 2400 K, both α_{cyan} and α_{red} is at 100%. Hence, for that particular CCT setting R_a and R_9 values cannot be greater than 90. The presence of minimum D_{uv} and optimum CRI are only found at one specific CCT, where the optimum lines intersect with each other. For this particular tri-color system, the intersection has a CCT value of 2090 K and CRI is at 98.6, respectively. However, this can compromise CRI and D_{uv} in order to achieve a larger tuning range of CCTs. In this case, if the CCT increases, the cyan level increases and D_{uv} becomes higher (Figure 4-2(d)) and that affects the quality of the white light output. So with the present tricolor LED color mixing system there will be a limit to achieving the desired values (low D_{uv} and high CRI) for the above mentioned CCT range. This limitation is overruled in the V8 light engine where the system is designed for five different colors covering a large spectral range. However, recent findings[101], [102] show that human preference for low CCT favors a negative D_{uv} and that the optimum might not be at zero D_{uv}.

4.2.2 Color choice and color gamut

The technical datasheet values for the used LEDs in the V8 light engine is documented in Table 4-1. The corresponding experimentally measured SPDs at 350 mA driving current for the five LEDs are represented by Figure 4-4(a). The corresponding measured experimental values are documented in Chapter 6. As seen in Figure 4-4(b); the produced wide color gamut by the above mentioned five LEDs are indicated in 1976 $(u´, v´)$ uniform chromaticity co-ordinates. The wide gamut produced by the five LEDs is capable of providing the tunable white CCT range from 3000 K to 6000 K.

Table 4-1: LED portfolio according to technical data sheet used in the V8 light engine [103]–[105]

LED type	LED colors	Part number	Data sheet in 2014		
			Current [mA] @ 85°C	Luminous flux [lm]	Peak wavelength λ_p [nm]
Luxeon Z	Royal blue	LXZ1-PR01-0600	700	823 mW	447.5
Luxeon Z	Blue	LXZ1-PB-01-0048	500	40	470
CREE XPE	Green	XPEGRN-L1-0000-00E03	350	105	528
CREE XPE	Red	XPERED-L1-R250-00801	350	54	625
CREE XPE2	White	XPEBWT-H1-0000-00BE7CT-ND	350	97	3000 K, 82 CRI

(a)

(b)
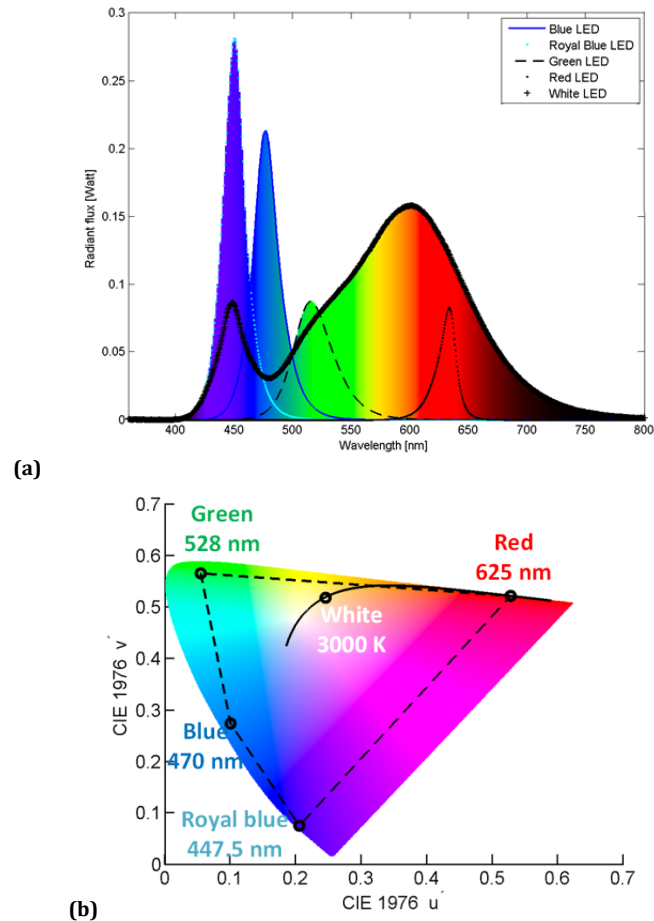
Figure 4-4 (a) SPDs for five used LEDS at 350mA driving current (b) Color gamut produced by five color LEDSs in CIE 1976 (u', v') uniform chromaticity diagram

4.2.3 Color quality in V8 light engine

By varying the proportional power output generated by five color LEDs, all the best possible SPDs for white light ranging from 3000 K to 6000 K for the V8 light engine are simulated using the optimization criteria listed in Table 4-2. The light qualities of those

simulated white light are also validated by experimental findings. Figure 4-5 shows the experimentally generated three CCTs and Table 4-3 represents the corresponding color qualities. It indicates the color quality of light by evaluating in CRI [49] and TLCI 12 [53] scale which are defined in 1.5.2.9 and 1.5.2.11 sections in Chapter 1. According to the application, the metric score for CRI and TLCI 12 are good for three CCT settings. To evaluate the score for TLCI 12, the TLCI 2012 software is used which is published by the EBU technical committee[53]. The obtained luminous flux was low (< 10,000 lm) for three CCT settings because of the losses encountered inside the system of the prototype which is modified afterwards by optimizing optical components, discussed in the section of 3.3 in Chapter 3 and Chapter 6, section 6.7.1.

Table 4-2: Optimization criteria for spectral simulation

Luminous flux	CCT	DUV	CRI
Highest achievable luminous flux at target CCT	Target CCT +/- 20K	< 5 * 10^{-3}	> 85
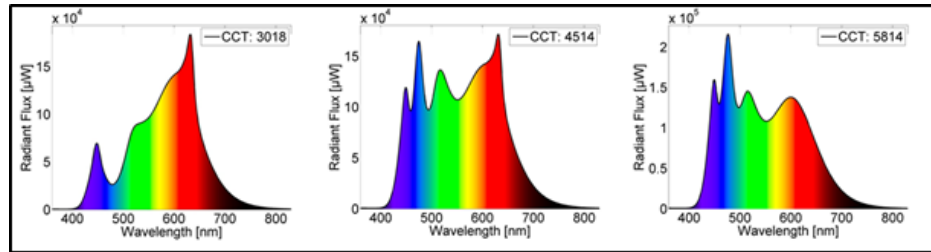
Figure 4-5: Experimental results of white light at three CCTs

Table 4-3: Light Output from V8 Light Engine at Three CCT Settings (Ref. Table 3 of Chakrabarti et. al [14])

Target CCT	Proportion of used color components					CCT	Produced light quality				
	Royal Blue	Blue	Green	Red	White		CRI (R_a)	CRI (R_9)	D_{uv} (10^{-4})	TLCI 12	Luminous flux [lm]
3000	1	0.5	17.3	100	100	3018	89.2	41.9	-6.6	75	7901
4500	14.2	45.9	77.5	79.3	100	4514	91.1	89.1	0.88	91	9295
5800	22.6	90.3	100	3.5	100	5814	88.5	76.2	1.5	87	9315

The produced CCTs are plotted at the Planckian locus in CIE 1960 (u, v) uniform chromaticity diagram in Figure 4-6. There are eight quadrangle BINs seen in Figure 4-6 by red color which include warm (2700K, 3000K, 3500K), normal (4000K, 4500K), and cold (5000K, 5700K, 6000K) range of CCT as a quadrangle for Solid State Lighting (SSL) products[106], [47]. These eight BINs are approved by the ENERGY STAR and a standard is documented as ANSI C78.377 (American National Standard Institute). This standard specifies the range of chromaticities recommended for general lighting while the chromaticity of light is represented by chromaticity coordinates (x,y and u',v'). The standard also defines the 7-steps from Planckain locus. According to the plot, the experimental solution for 4500 K is located on the Planckian locus and the solutions for 3000 K and 5800 K are having a negative and positive D_{uv} value respectively. Since all

D_{uv} values are $< \pm 10^{-3}$, they indicate white lights. However, the light which is having negative D_{uv} value has pinkish tint whereas the D_{uv} with positive value has greenish tint.
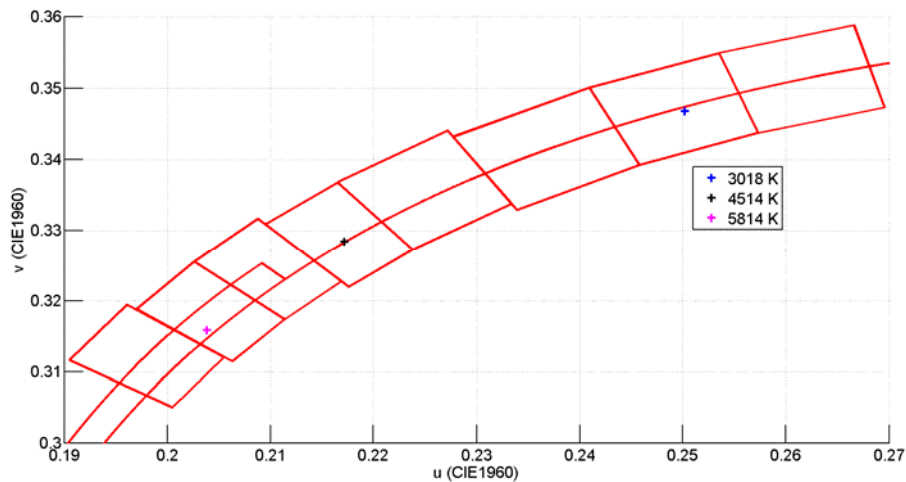

Figure 4-6: Three experimentally found CCT points on the CIE 1960 (u, v) uniform chromaticity diagram (Ref. Figure 5 of Chakrabarti et. al [14])

4.3 Discussion on the utility of the technique

The ability to create a great variety of colors is an important quality for displays. The color gamut represents the entire range of colors that can be created from a set of primary sources. Color gamut is a polygon positioned within the perimeter of the chromaticity diagram. All colors created by additive mixtures of the vertex points (primary colors) of a gamut are necessarily located inside the gamut. In our case, it is desirable that the color gamut provided by the five light sources is as large as possible to create displays which are able to show brilliant saturated colors. The color consistency within 360 nm to 800 nm can obtain in the resultant SPD of produced white light by using five color components which can be seen in Figure 4-4(a). The color gamut created by the five colors LEDs in Figure 4-4(b) is chosen to provide a large color gamut area including highly saturated colors and covers a range of white light corresponding to different color temperatures and characterized by high color rendering properties. The blue and the red LEDs are used with other three LEDs (royal blue, green, and white LEDs) to cover the entire blackbody radiated color temperature from 3000 K to 6000 K. A warm white LED is added in the gamut to provide base CRI (~82) and then CRI could improve by adding more red. Though more red cannot be used as it will decrease the efficiency of the system, there will be still having flexibility to optimize the CRI, as well as the efficiency by other remaining colors (namely, royal blue, blue, and green) and that is the unique advantage of the spectral mixing procedures reported in this thesis. Table 4-3 indicates the high color qualities of the produced white light at three different CCTs. Good specific CRI R_a (>85) at each CCT will help to render color effectively. Good specific

CRI R_9 (>40) implies important red content and helps to light raw meat or interior lighting decorations in display lighting. The score of TLCI 12 > 75 signifies that the produced white light can be used in a studio without having any corrections done by camera. The luminous flux in a warm color temperature regime would not be as high as in a cold color temperature regime because in warm color temperature regime, the proportion of used red LEDs would be higher than other LEDs. However, the luminous flux will be improved gradually as it moves towards a colder color temperature using more proportions of green, blue, and royal blue LEDs by compromising with having a higher D_{uv} value. However, CRI will improve more than in a warm CCT regime. To optimize the CCT point again with high light qualities, the simulated resultant SPD use the optimization criteria described in Table 4-2.

4.4 Summary

This chapter provides the methodology for the color mixing technique adopted in designing the V8 light engine. The spectral modelling is based on the optimization of color qualities e.g., high CRI indices (R_a>85, R_9 >40) and low D_{uv} (< ±10^{-3}) at the corresponding desired CCT. To provide an example for the experimental validation of the simulated SPDs, the measured light quality and luminous flux for three target CCT settings (3000 K, 4500 K and 5800 K) with their corresponding SPDs from the V8 light engine are documented. The created wide color gamut in 1976 (u´,v´) uniform chromaticity diagram by five different multi-colored LEDs is projected to show the capability of the V8 light engine to tune the CCT ranging from 3000 K to 6000 K. The following chapter will explain the color control mechanism of the V8 light engine.

Color consistency of the V8 light engine

*'Consistency is the last refuge of
the unimaginative.' – Oscar
Wilde*

Chapter 5 : Color consistency of V8 light engine

5.1 Introduction

Upon till now the subject has been on the advantages of the V8 light engine as a stage lighting luminaire over the traditional lighting system, the light engine could have deficiencies in terms of the lighting system's stability in luminous flux, and color (e.g, CCT, D_{uv}, CRI, etc.) during the operational time if the system does not encompass any control system. Since the V8 light engine comprises multi-colored LEDs, there are also often noticeable luminous flux and color variations in light output for similar V8 systems. The long term and short term operational stability of the light output depends on many influencing factors i.e. LED binning (wavelength and flux) and aging, ambient temperature, LED junction temperature, driver electronic such as digital control of current, system run time, etc.[99]. Thus, the luminous flux and color variations from lamp to lamp and stability over both short and long time operation are very critical and should be controlled to remain within certain limits. To provide controlled light output without compromising the efficiency and light quality, several methods were implemented based on temperature feedback, optical feedback such as flux and color feedback, or a combination of temperature and optical feedback[107]–[112]. To provide optical feedback, in many cases, simple color sensors are preferably used to examine the instability and to provide information of color values to a feedback system. These could be: CCT, D_{uv}, and luminous flux [17], [18], [113]. Therefore, the feedback control system could work effectively if known uncertainties of the influencing parameters could be investigated and used as input into the feedback loop[20], [114].

5.2 Monte Carlo simulation

The uncertainties of the above mentioned influencing parameters are experimentally studied and evaluated by use of the Monte Carlo simulation as explained in the articles by Chakrabarti et. al [23]–[25]. Since the Monte Carlo method avoids the analytical propagation of uncertainty by combination of simulated and experimental findings of the uncertainties of individual input parameters of colored LEDs, there is no requirement for deriving the partial derivatives of the complicated equations. Furthermore, the uncertainty can be examined for any color quantities in an easy way. Thus many applications could use this Monte Carlo Simulation to estimate and analyze

measurement uncertainty based on the propagation of distributions[115]–[117]. The Monte Carlo method can provide and analyze the uncertainties of chromaticity coordinates over the tunable range, and can relate them to the colorimetric values e.g. CCT and D_{uv}, and CRIs for the multicolored V8 LED engine. The Monte Carlo analysis presented here is based on an experimental investigation of the basic sensitivities to external changes which was carried out on the V8 LED light engine. It was also aimed to analyze the achievable stability by implementing a color sensor. Therefore, the analysis incorporates many of the factors influencing the color uncertainty for similar system, i.e. LED binning and aging, ambient temperature, driver electronic as digital current control, and color sensor spectral response.

A method that makes use of a Monte Carlo simulation approach to estimate the resulting propagation of uncertainties of any color quantity of the multi-colored V8 light engine will be described in this section. The first step of the method is to build a model of the LED system. The second step is to obtain experimentally or otherwise the uncertainty of the controllable parameters as well as the uncertainty of the inherent properties of each LED (peak wavelength bin, wavelength shift with temperature, flux bin, expected aging, etc.). The third step is to apply the Monte Carlo Method on this model, calculating a set of resulting spectral power distributions (SPDs) from the model with random values taken from the probability distribution of each input parameter and deriving the colorimetric results. By implementing a feedback and control loops in the model of the V8 light engine, the uncertainty in the colorimetric values is decreased. The associated uncertainties related to control sensors and electronic circuits will have to be included when the control feedback loop is applied.

5.2.1 LED model and pre-calibrated lookup table

The model of the LED system is simulating the spectral radiant flux for each colored LED used in the V8 light engine as input to mix the spectral content of a LED color mixing model which is reported in the articles by Chakrabarti et. al [23]–[25]. It is the model using four colored LEDs to supplement and change the SPD from the warm white LED at 3000 K (Table 4-1). The output from individual LEDs is added to produce the resultant SPD. The resultant SPD provides white light output from the light engine with option of light intensity dimming, achieving a minimum lower dimming to 13%, and varying the CCT ranging from 3000 K to 6000 K. There is a pre-calibrated lookup table which is associated with the white tunable multicolored V8 light engine. The lookup table consists of target CCTs (3000 K to 6000 K in 1% step size of previous one) and corresponding target luminous flux, Φ_V, (1000 lm to 8000 lm in 3% step size of its precursor) at optimized D_{uv} ($< \pm 2 \times 10^{-3}$) (seen in Figure 5-1). The black dots in the figure represent the possible guided points in the lookup table for the CCT ranging from 3000 K to 6000 K with dimmable capability from 1000 lm to 9000 lm corresponding to each CCT setting. The green dots imply the found solutions from the V8 light engine corresponding to black dots. As seen in the figure, there were some difficulties to find solutions for the region above 6500 lm for ~3000 K. A similar occurrence is observed in the region from ~4200 K to 4300 K. This could appear due to the limitation of the LEDs used in the color mixture.
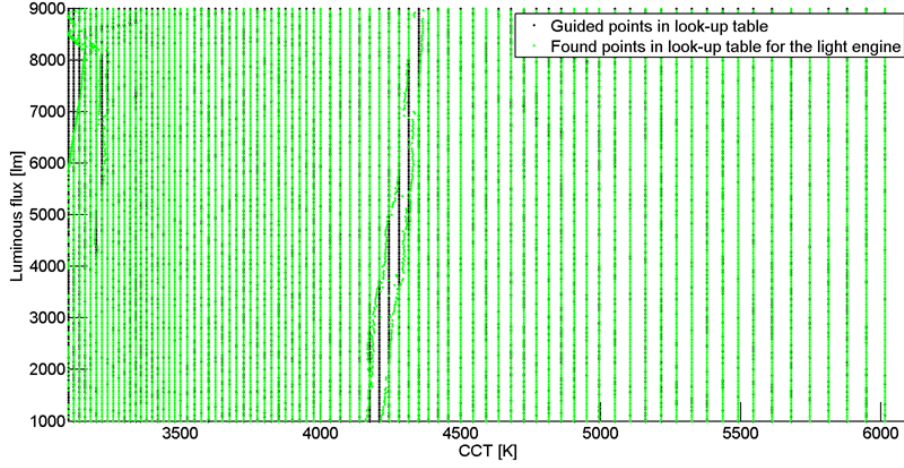
Figure 5-1: Pre–calibrated lookup table consists of target CCTs (3000 K to 6000 K in 1% step size of the previous CCT and corresponding target luminous flux 1000 lm to 9000 lm in 3% step size of the previous Φ_V) at optimized D_{uv} (< ±2 x 10^{-3}) (Ref. Figure 1 of Chakrabarti et. al [24])

The lookup table is generated from a spectral calibration of the LED color mixing model. After setting the target of CCT and Φ_V as reference, the lookup table is used to find the optimum adjustments for the individual LEDs which are optimized to lowest D_{uv}, and close to target CCTs. The target color settings for the light output are also optimized by a high general color rendering index (CRI) $R_a > 85$ and specific CRI $R_9 > 40$ for rendering the strong red objects (seen in Figure 5-2). In Figure 5-2 (a) and (c), for each CCT setting, the found D_{uv} and CRI (R_a) for different Φ_V are distributed in vertically. As expected, the CRI (R_a) in Figure 5-2 (c) is low in the warm white region compared to the cool white region. However, D_{uv} are low (< ± 2 x 10^{-3}) throughout the operating range in Figure 5-2 (a). Similarly in Figure 5-2 (b) and (d), for one Φ_V setting, the found D_{uv} and CRI (R_a) for CCT ranging from 3000 K to 6000 K are distributed vertically. No such patterns similar to Figure 5-2 (a) and (c) are found for D_{uv} and CRI (R_a).
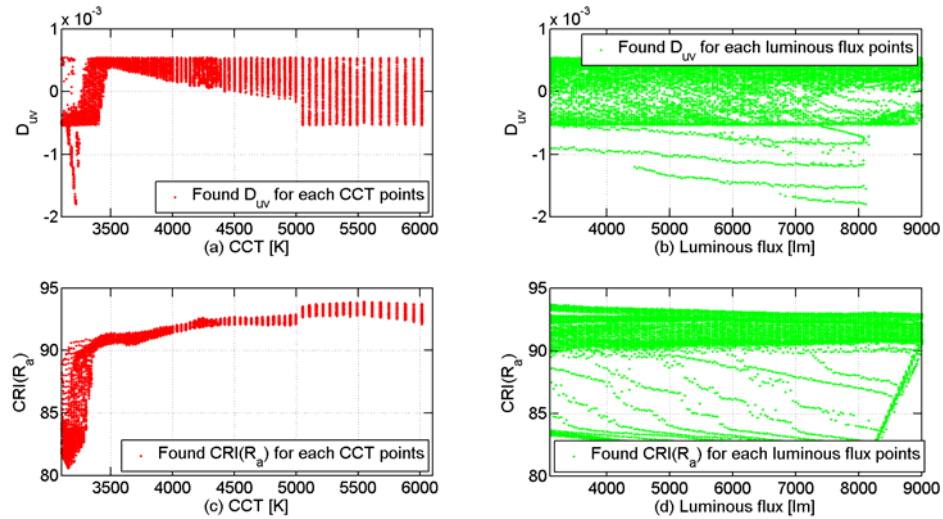
Figure 5-2: (a and b) Optimized D$_{uv}$, (c and d) and CRI (R$_a$) vs target CCTs and Φ$_V$ respectively (Ref. Figure 2 of Chakrabarti et. al [24]**)**

The target point in the lookup table offers information about the corresponding DMX values for the individual color channels (seen in Figure 5-3). In Figure 5-3 (a)-(e), for each CCT setting, the contribution from different LEDs for different Φ$_V$ are vertically distributed. Figure 5-3 (f) represents the same result while plotting every color LED in the same graph. As expected, to construct the warm white, the contribution from the red LED is more than the green and the blue LEDs and it decreases gradually towards the cool white. Similarly, the green and the blue LED contributes more in the cool white region than the red LED. The contribution from the white LED is almost the same throughout the entire the CCT range as it is used as a base LED.
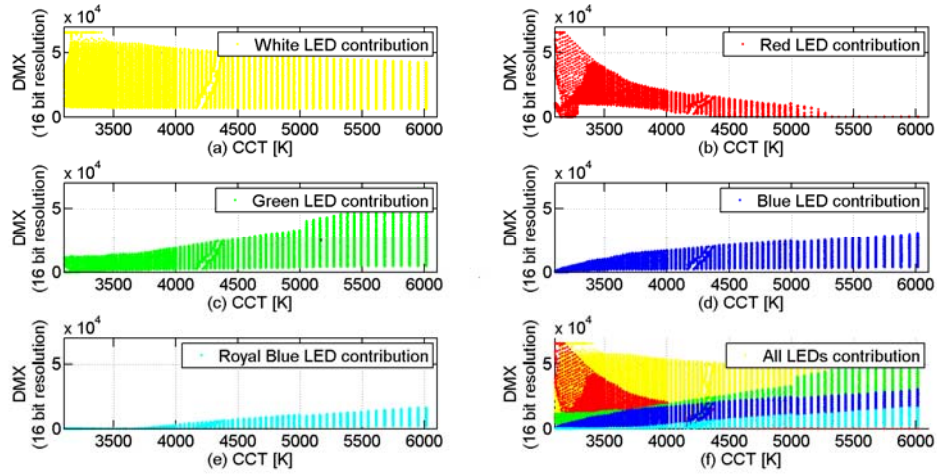
Figure 5-3: Corresponding driving current information for individual LEDs for target CCTs for different Φ$_v$ (Ref. Figure 3 of Chakrabarti et. al [24])

Figure 5-4 shows the best found solutions for four CCTs (3000 K, 4000 K, 5000 K, and 5800 K) at 8000 lumen and these SPDs are considered as target SPDs as black line. In Figure 5-4, the purple lines are reference SPDs, which for CCT < 5000 K are represented by Planckian radiation spectrum and SPDs for CCT > 5000 K are represented by D – illuminant. The rest of the colored spectrums in Figure 5-4 represent the contribution from individual colored LEDs to produce the target SPD. The SPDs from individual LEDs used in the model are calculated from spectral measurements (Chapter 6), with variation in the various controllable parameters (current, junction temperature etc.) which are already explained in Chapter 4 and in the articles of Chakrabarti et. al [23].
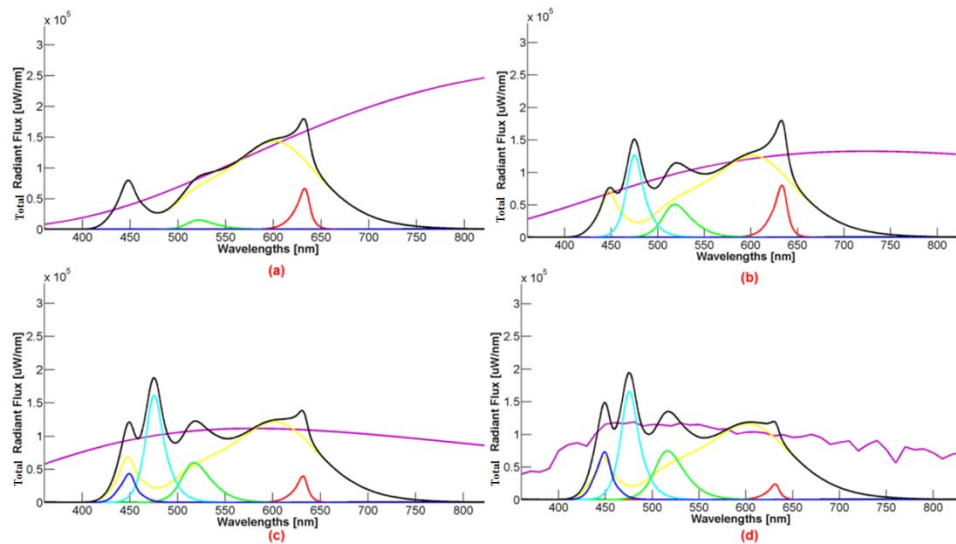
Figure 5-4: Resulting target SPDs (black line) of five color mixing LED system at four different target CCTs (3000 K, 4000 K, 5000 K and 5800 K in (a) – (d), respectively) and the corresponding reference SPDs (purple line). Individual SPDs for the colored LEDs are also shown by different colors (Ref. Figure 1 of Chakrabarti et. al [23])

5.2.2 Uncertainty analysis by the Monte-Carlo simulation

The Monte Carlo simulation is developed by incorporating many of the input parameters i.e. LED binning, ambient temperature and driver electronics such as digital control on current, which influence the color uncertainty within the light engine. The above mentioned input components are distinguished by three categories (system, loop and history) based on their inherent nature of influence. Although LED aging, abrupt failure of LEDs, and contamination inside the system may cause variations in light output, this thesis did not consider those influences into the simulation and future work will address those issues. The following Table 5-1 describes the individual components in detail which is also reported in the article of Chakrabarti et. al[23].

Table 5-1: Components responsible for uncertainties in light output from light engine (Ref. Table 1 of Chakrabarti et. al [23])

Component Description / unit	Type of parameter	Sensitivity from (Cause)	Sensitivity to (effect)	Relation
LED bin Flux(Φ) in lm, wavelength(λ) in nm	System and Static	Bin width	Φ, λ	linear
Driver current in mA	Loop and Dynamic	Digital current controller	Φ, λ	linear
Digital current controller in number	Loop and Dynamic	Current, driving controller	Φ, λ	Droop curve with steps
LED junction temperature in ℃	Loop and Dynamic	Current, run time, and environment	Φ, λ	linear
Temperature in ℃	History and Dynamic	Ambient temperature	Φ, λ	linear
Color sensor spectral response in number	System and Static	Tristimulus values	Φ, λ	linear

The simulation has run continuously to create a realistic scenario for the V8 light engine in case the engine would be exposed to different varieties of LED bin, environment, etc. The flow chart in Figure 5-5 describes the method of the Monte Carlo analysis of the multi-colored V8 light engine. The chromaticity coordinates (u´,v´) of the simulated SPDs will be plotted in the CIE 1976 chromaticity diagram and Δu´v´ will be compared in the n–step u´v´ circle (where n=1.18 and just noticeable chromaticity difference Δu´v´=0.0013) as defined in CIE TN001:2014[46]. The uncertainties of the u´, v´ chromaticity, CCT, D_{uv}, and Φ_V have been calculated as output parameters from the simulation using the probability distribution of the input parameters for each colored LED. The outputs from the simulation are analyzed subsequently by calculating the coverage interval and their sensitivity to the input parameters at different CCT settings of the dynamic light engine.
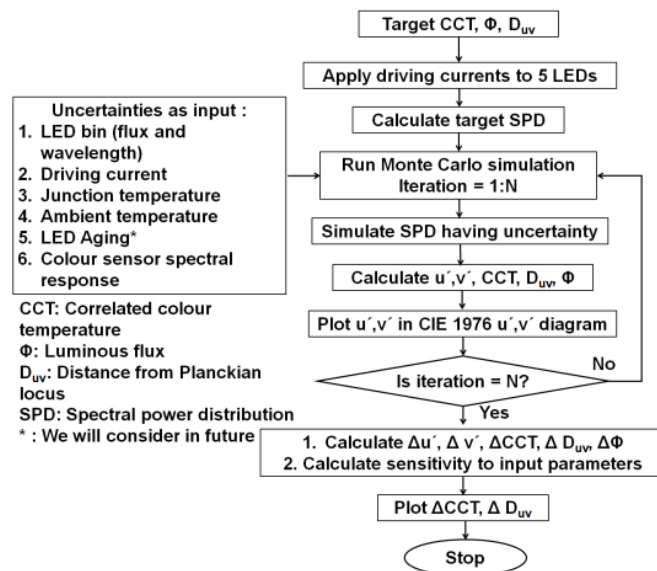
Figure 5-5: Block diagram of the Monte Carlo simulation with N iteration for the multi-colored LED system (Ref. Figure 2 of Chakrabarti et. al [23])

The experiments on the individual LED provide the variation in light output and peak/dominated wavelength due to changes in the input parameters for each colored LED. The graphs in Figure 5-6 illustrates the radiant flux and peak wavelength variation with respect to changes in the driving current (top) and case temperature (bottom) for individual LEDs at a constant case temperature (top) and driving current (bottom). The radiant flux and peak wavelength variations are compared with values obtained at a 300 mA driving current in Figure 5-6 (a) and (b). Figure 5-6 (a), shows the radiant flux increase almost linearly to the increased driving current. However, the slope of the curve is much higher for a red LED than other colored LEDs. In Figure 5-6 (b), the peak wavelength shifts towards higher values with the increase of the driving current for the blue and red LEDs. However, the effect is opposite for a green LED. For Figure 5-6 (c) and (d), the radiant flux and peak wavelength variations are compared to values obtained at case temperature of 20 ℃. Figure 5-6 (c) shows, the radiant flux decrease for each colored LED almost linearly by increasing the case temperature. In this case, the slope of the curve for the royal-blue LED is higher than other colored LEDs. Figure 5-6 (d) represents the sensitivity of the peak wavelength with respect to changes in the case temperature for each individual colored LED. In this graph, peak wavelength shifts towards higher wavelength for each colored LEDs by increasing case temperature. As expected, the sensitivity is higher for the red LED compared to other colored LEDs.
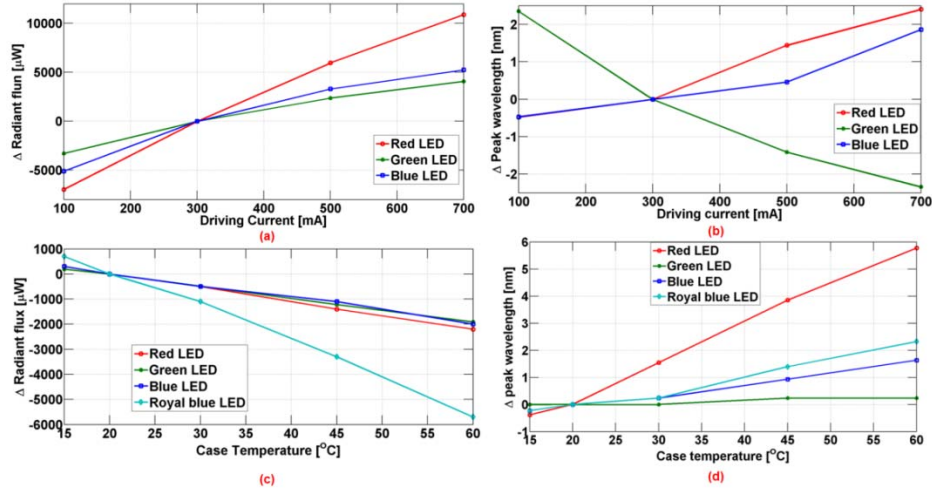
Figure 5-6: Sensitivity of radiant flux (a) and peak wavelength (b) for the individual colored LED by varying driving current to 300mA when the case temperature is at 20 °C. Sensitivity of radiant flux (c) and peak wavelength (d) for the individual colored LED by varying the case temperature to 20 °C when the driving current is at 700mA (Ref. Figure 3 of Chakrabarti et. al [23])

As we understand from the above experimental results that the LED performance varies with operating condition, there is a challenge to get a stable light output from the LED lighting system without considering any controlled operating conditions. Thus, it is critical to investigate and consider the uncertainties in the operating conditions of individual LEDs. Due to the uncertainties in the operation condition on the individual driving current of LEDs, the light engine could not produce the light output with desirable target values. The Monte Carlo simulation simulates and applies the variation on operating conditions of the individual LED internally for N = 2000 iterations by considering the uncertainties (mentioned in Figure 5-5) as input parameters. These results lead to simulate 2000 resultant SPDs of the LED color mixing system, acting as a 2000 virtual V8 light engines. Figure 5-7 shows an example of the variation of SPDs from the individual LEDs due to the above mentioned uncertainties as input parameters. By using the estimated uncertainties in output parameters due to the uncertainties in input parameters, the Monte Carlo simulation calculates corresponding color quantities as output (namely u´, v´, CCT, D_{uv}, Φ_V).
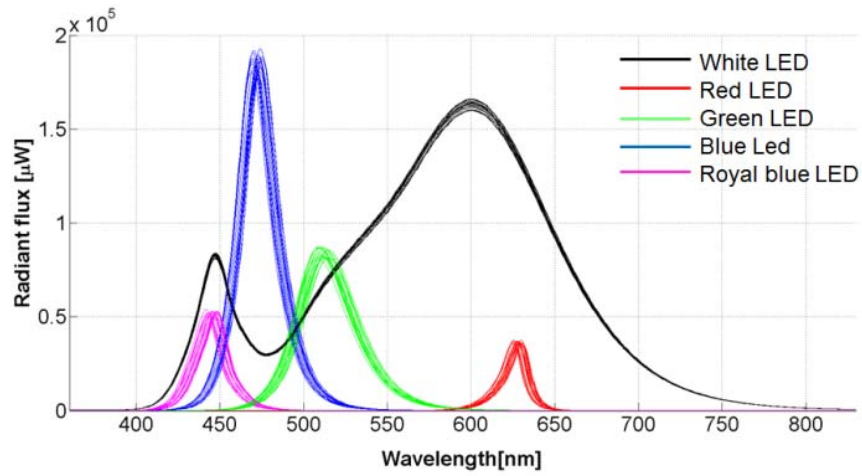
Figure 5-7: Illustration of variation of SPDs with the variation of uncertainties as input parameters (Ref. Figure 4 of Chakrabarti et. al [23]**)**

As an example to illustrate the output of the Monte Carlo simulation, 5000 K with 8000 lm as target CCT and Φ_V is considered (Figure 5-4 (c) and the corresponding values are shown in the look-up table). After, the Monte Carlo simulation is applied on the target SPD. From the result of the 2000 SPDs, the chromaticity coordinates (u',v') are calculated and plotted into the CIE 1976 diagram in Figure 5-8 (b) as green dots along with the mean point (blue '+') of those variations. In Figure 5-8 (a) and (c) the corresponding probability distribution of variations in v´ and u´ are plotted and indicate the lower and upper bound of 95% coverage interval area by red arrows. In Figure 5-8 (b), the isothermal line (red line) represents ΔD_{uv} and the Planckian locus (black line) represents ΔCCT, which is analyzed in Figure 5-9. By taking the mean point as the central point (blue '+'), a circle with a radius of 0.0013 (u´v´ circle in CIE TN001:2014[46]) is drawn in Figure 5-8 (b). The found outcomes are mostly outside from the just noticeable chromaticity difference circle (blue). Even the target point represented by the brown '+' is also outside the just noticeable chromaticity difference circle indicating an offset from the lookup values. The CCT and D_{uv} are calculated from (u´, v´) for the 2000 iterations. The probability distribution of the variations in CCT and D_{uv} are shown in Figure 5-9 (a) and (b), respectively. Considering a 95% coverage area, ΔD_{uv} = 0.0095 with the mean of -0.0046 and ΔCCT = 339 K with the mean of CCT 5068 K are found. Similarly the Monte Carlo simulations are repeated for the target settings from 3000 K to 6000 K with target Φ_V values at 8000 lm to obtain the similar output parameters as mentioned above. Each time the simulation runs for 2000 iterations.
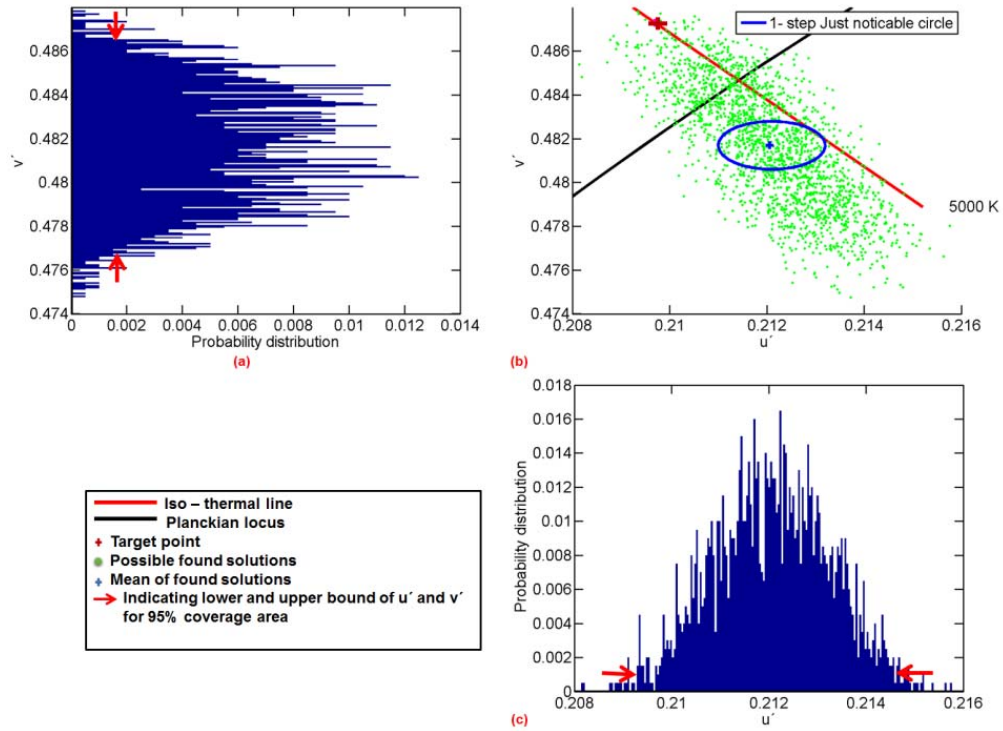
Figure 5-8: (a) and (c): represent probability distributions for v´ and u´ where the red arrows are indicating lower and upper bound of u´, for a 95% coverage area respectively. (b): All possible outcomes for the 2000 iterations of the Monte Carlo simulation are plotted into u´,v´ diagram (CIE-1976 chromaticity coordinates) at 5000 K (2:1 axes) (Ref. Figure 5 of Chakrabarti et. al [23])
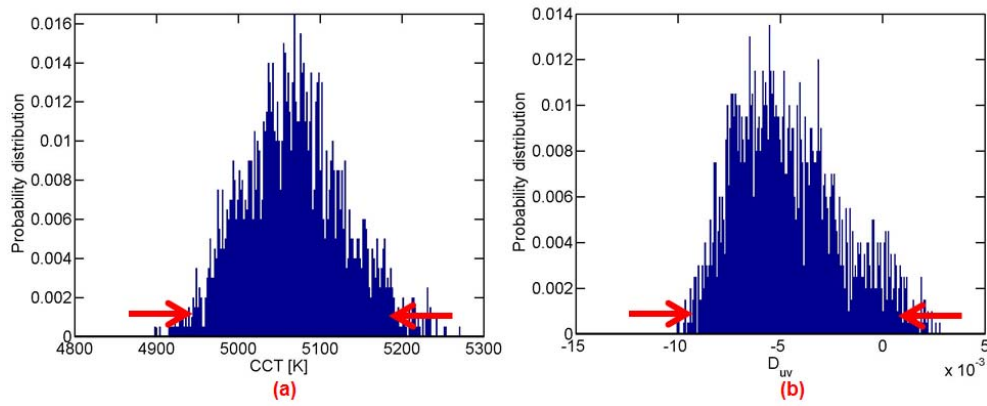
Figure 5-9: Probability distribution functions of CCT (a) and D_{uv} (b) at 5000 K CCT settings by calculating the coverage interval of the corresponding colorimetric quantities where ΔCCT=339K and $ΔD_{uv}$=0.0095 for 95% coverage interval (Ref. Figure 6 of Chakrabarti et. al [23])

The Monte Carlo simulation is analyzed to find the correlation and sensitivity between the input parameters for each colored LED to output parameters of the V8 light engine. The sensitivity estimations are used to find the critical parts in the system for correction and system stability of the light engine at different CCT settings. The results are analyzed and plotted in Figure 5-10 for the sensitivity to output parameters CCT and D_{uv}. In general within the warm white region, the contribution from the red LED is higher than for the cool white region. Similarly, in order to obtain an SPD in the cool white region, the blue LED contributes more compared to the red LED (as seen in Figure 5-3 and Figure 5-4). As an example, in Figure 5-10 the sensitivity in CCT and D_{uv}, with respect to used individual current for each colored LED are plotted for the target CCTs ranging from 2800 K to 6000 K. The sensitivity of CCT (S_{CCT}) in K / mA and S_{Duv} mA^{-1} for D_{uv} are measured according to following equations.

$$S_{CCT} = \frac{\Delta CCT}{\Delta I} \tag{45},$$

Where ΔCCT is the change in CCT (K) for change in current ΔI (mA) of the individual colored LED. Therefore, the unit of S_{CCT} is K / mA.

$$S_{Duv} = \frac{\Delta Duv}{\Delta I} \tag{46},$$

Where ΔDuv is the change in D_{uv} for change in current ΔI (mA) of the individual colored LED. Therefore, the unit of S_{Duv} is mA^{-1}.

As expected, CCT and D_{uv} are very sensitive to the red LED in the warm white region in Figure 5-10 and it is almost zero towards 6000 K. Similarly the effect will be reversed in the case of the blue/royal blue LED. The two different colored blue LEDs are more sensitive with the change in CCT and D_{uv} at 5000 K compared to the other colored LEDs. The green and the white LED contributions are always required in both above mentioned regions. The CCT is sensitive in the white LED more than D_{uv}. The green LED influences both CCT and D_{uv}. The blue and the royal blue LEDs have almost the same influence on CCT and D_{uv}.
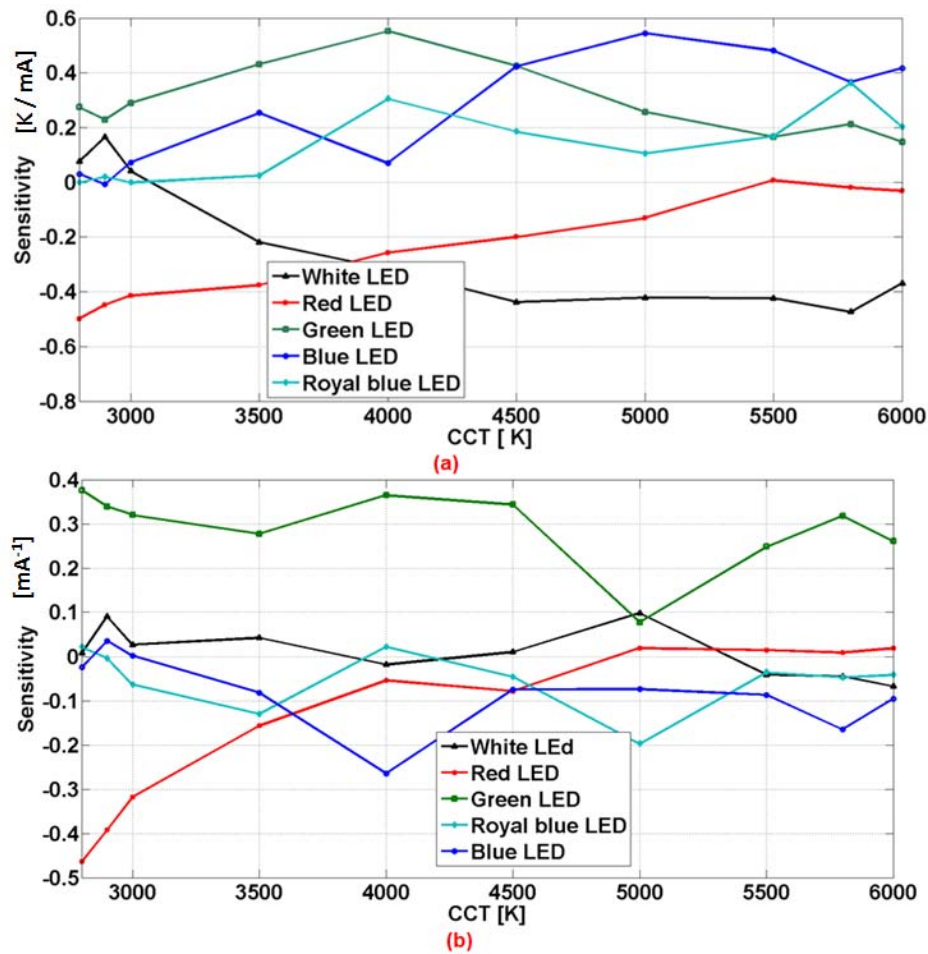
Figure 5-10: Sensitivity of output parameters namely in CCT (top) and D_{uv} (bottom) at CCT settings ranging from 2800 K to 6000 K due to the individual five colored LEDs (Ref. figure 7 of Chakrabarti et. al [23])

5.3 Color and luminous flux control mechanism

As seen in Figure 5-8 (b), the size of the distribution of the possible found outcomes for the 2000 iterations has a much larger spread than the just noticeable chromaticity difference (JND) circle (as defined in CIE TN001:2014[46]). The variations corresponds to n= 8 step circles (according to equation (47)) which is far from the just noticeable chromaticity difference variations of n = 1.18. Hence the average human eye could easily notice the difference of light output for the same target CCT setting. A large offset between the mean value and the target values is observed. Therefore, the variation of chromaticity and luminous flux need to control. A color control system needs to be

implemented and the developed Monte Carlo simulation will need to evaluate the color feedback system.

$$n = \frac{\Delta u'v'}{0.0011} \tag{47}$$

Therefore, the color control mechanism presented here is divided into three parts which are: 1) control algorithm, 2) hardware, and 3) statistical analysis of uncertainty contributors/components, called as "uncertainty parameters" (listed in Table 5-1). The color control mechanism incorporates the pre-calibrated lookup table and a calibrated color sensor that monitors the chromaticity of the uncorrected resulting white light output providing a feedback to the control system to regulate the color and the light output variations within a certain limit. In order to correct the light output, the control unit offers a new set of driving currents to the individual color channel by choosing a new lookup point. The stability of the system is characterized by evaluating the resulting chromaticities in the uniform chromaticity diagram (CIE 1976 [46]) with a target tolerance within a circle radius of 0.0026 (n=2). A schematic diagram of the color control system is shown in Figure 5-11. The following paragraph elaborate on the process again in detail which is all reported in the article by Chakrabarti et. al[25].
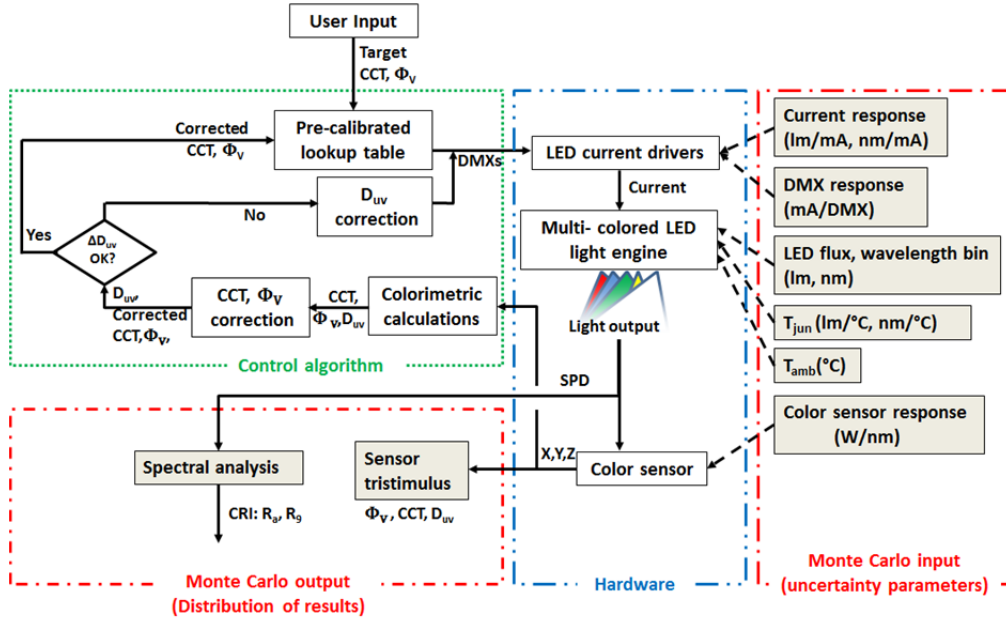
Figure 5-11 Schematic diagram of the color control system of the multi-colored tunable (3000 K to 6000 K) V8 light engine, T_{amb} = ambient temperature and T_{jun} = junction temperature of the LEDs (Ref. Figure 1 of Chakrabarti et. al [25])

First, the user sets the target CCT (3000 K – 6000 K) and Φ_V (1000 lm – 8000 lm) for the V8 light engine as reference. The control algorithm finds a match in the lookup table closest to the target values. In the ideal case, the lighting system delivers the target by using corresponding DMX values of individual color channels from that lookup point.

The aforementioned uncertainty parameters (Table 5-1) inside the system influence the light output which will be analyzed by the statistical analysis using the Monte Carlo simulation process with iteration N= 2000 (explained in the section 5.2). Thereafter, the Monte Carlo simulation process investigates the colorimetric and photometric variations of the spectral light output (u′, v′, and corresponding CCT, D_{uv}, and Φ_V) based on the uncertainties such as current response (lm/mA, nm/mA), DMX response (mA/DMX), LED flux and wavelength bin (lm, nm), junction temperature of LED (T_{jun}, °C), ambient temperature (T_{amb}, °C), and color sensor response (W/nm) as shown in Figure 5-11(extreme right red block). To control the CCT and Φ_V variations in real-time, the color sensor has been implemented to monitor and get feedback from the light output (as seen in Figure 5-11). The color sensor used has approximate tristimulus responsivity ($\overline{X}$, $\overline{Y}$ and $\overline{Z}$) and needs to be calibrated close to the operating chromaticity range (explained in the section 6.5.1 in Chapter 6) in order to minimize spectral mismatch errors. The color sensor was calibrated by using a handheld spectrometer (GS-1150)[118]. After having the measured tristimulus values of the resulting white light[119], the control unit calculates the corresponding error correction for CCT and Φ_V which directs to use a new lookup point from the lookup table. The new lookup point provides the corrected driving information for the individual color channels to deliver a corrected light output which is closer to the target CCT and Φ_V values. The lookup table has already the optimized D_{uv} values (< ±5 x 10^{-3}) for each lookup point. Thus, the new lookup point should have D_{uv} value < ±5 x 10^{-3}. However, if the corrected light output cannot provide the controlled light output within a certain limit[46], the D_{uv} needs to be controlled using the individual color sensitivity to D_{uv}(Figure 5-10 (b)). If the obtained D_{uv} shows the higher value than the desired D_{uv} value, the green channel needs to go down along with adding more from red and/or blue channels depending on the CCT region. For negative D_{uv} correction, the green channel needs to go up while the red and / or blue need to drive less than the earlier settings. Finally, the changes in driving currents at the respective color channels leads to choose new lookup point which is evaluated by plotting in the CIE 1976 (u′,v′) diagram. The controlled point inside the CIE 1976(u′,v′) are not within JND circle. However, 95% of controlled points are within n=2 circle. they are The proposed control mechanism cannot control color rendering indices (CRI(R_a), CRI(R_9)[120]. However, the controlled light output has good light quality in terms of CRI R_a (> 85) and R_9 (> 40) observed. The control mechanism can be generalized to be used in any other SSL system (such as additive laser color mixing system) where instead of using the color sensor, a spectrometer may use for sensing the spectral information.

5.4 Discussion on color control

The simulated light output for tuning range 4000 K to 6000 K shows an average of 8.5% variation on Φ_V within a 95% coverage interval over initial setting of 8000 lm due to uncertainties of the input parameters if the T_{amb} changes from 20°C to 45°C. Generally, red LEDs are highly sensitive towards a change in current and temperature compared to other LEDs (Figure 5-6). Thus, due to larger content of red LEDs than other LEDs in the warm and neutral white region, the higher color variation is observed within that region. The highest uncertainty on the CCT at 4000 K is found 1020 K. As an example to illustrate the color variation and the corresponding color control in the V8 light engine,

the values of 5500 K and 8000 lm as target CCT and Φ_V, respectively, are used and the corresponding DMX values for individual color channels from the lookup point are transferred to the lighting system to simulatete target SPD. Afterwards, the Monte Carlo method is applied on the target SPD to impose the variations due to input parameters for 2000 iterations. For example, based on 2000 iterations Figure 5-12 represents the random distribution of heatsink temperatures between 25 °C and 50 °C. Due to the variation of the heatsink temperature, the junction temperature of the LED also varies. Figure 5-13 illustrates the change in the junction temperature for individual LEDs due to changes in the heatsink temperature.
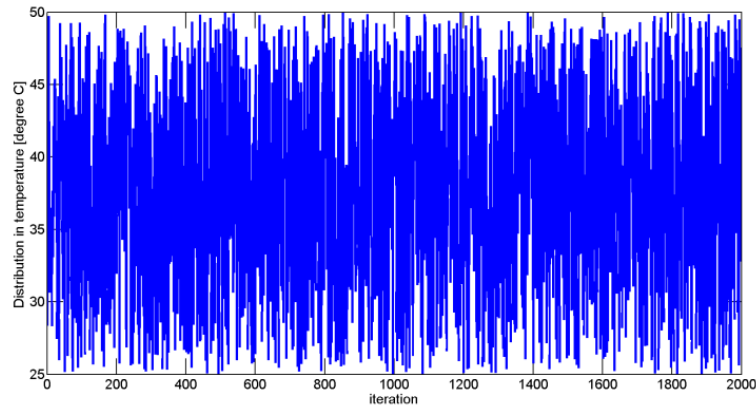
Figure 5-12: Random distribution of heatsink temperature for 2000 iterations

(a)

(b)
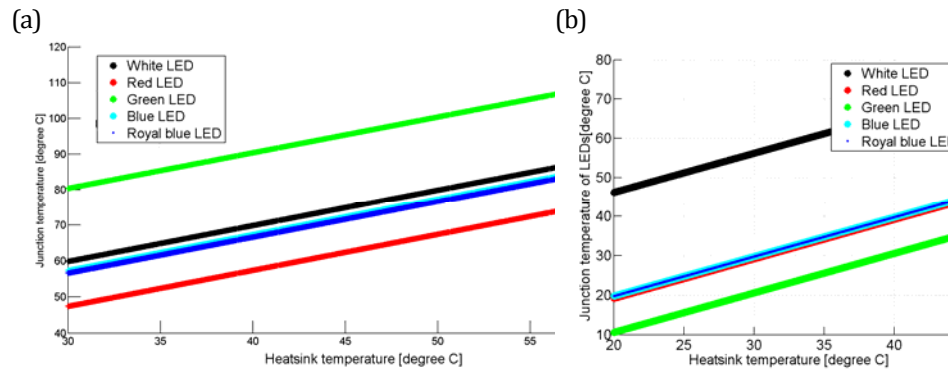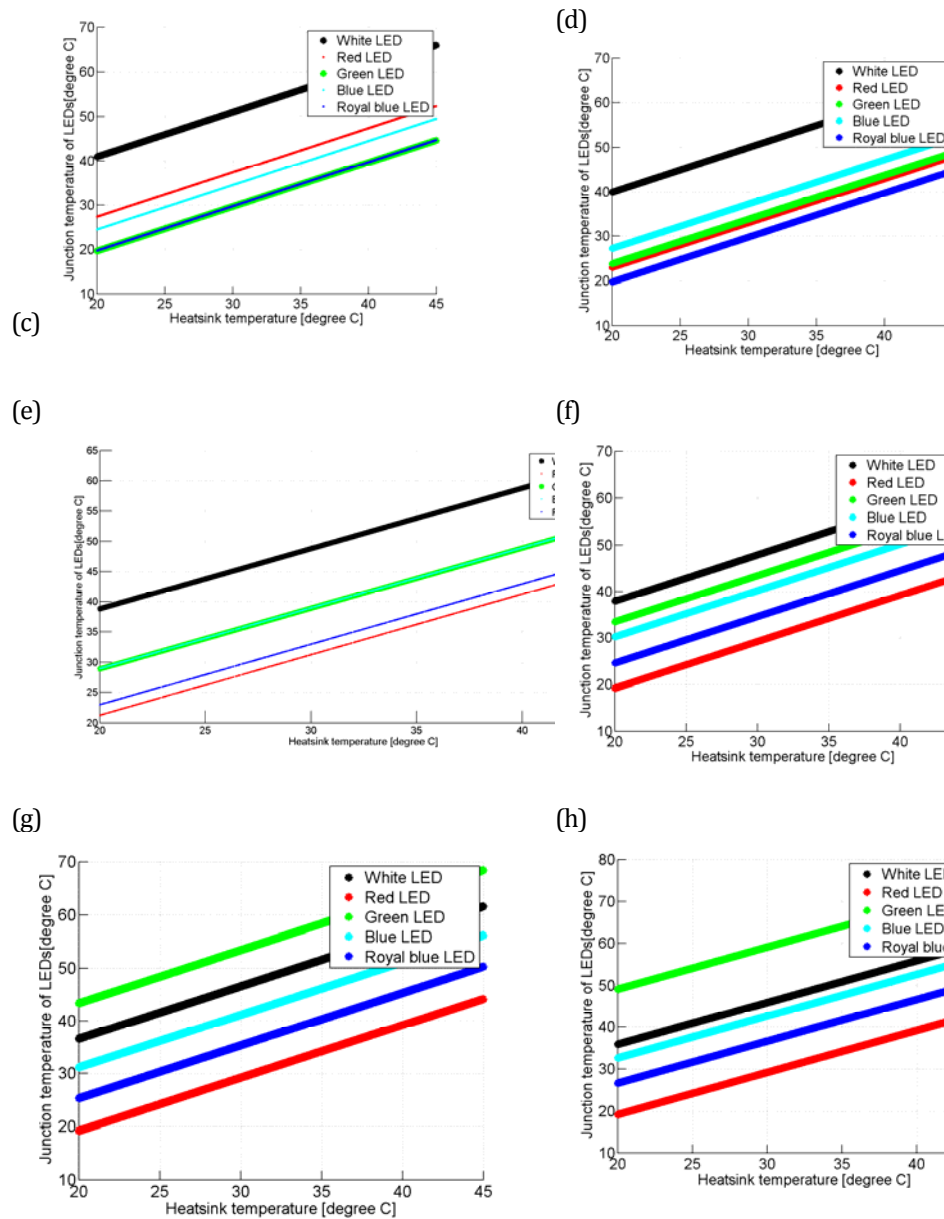
Figure 5-13: Relation between junction temperature of individual LED and heatsink temperature

Figure 5-13 (a) shows the junction temperature variation with respect to the change in the heatsink temperature while all LEDs are set at full electrical load. That means the white; the green, the blue and the royal blue LEDs are operating at a 1000 mA current while the red LED is operating with a 700 mA current. In this scenario, the junction temperature of the green LED is always higher than the other LEDs and it reaches ~110 °C while the corresponding heatsink temperature is at 60 °C. Figure 5-13 (b) to (h)

represents the junction temperature variations of the individual LEDs at 3000 K, 3500 K, 4000 K, 4500 K, 5000 K, 5500 K, and 6000 K, respectively. As seen from Figure 5-3, the contribution for each LED is not the same for all regions of the white light generation (warm, neutral, and cool). Therefore, at the warm white region,(Figure 5-13 (b) to (d)) the junction temperature of the red LED is high compared to the neutral and cool white regions (Figure 5-13 (e) to (h)). Similarly the green LED takes over the position of the red LED for having a high junction temperature if the CCT from the warm white transits towards the cool white region. However, the change in the junction temperature influences the LEDs to change the luminous flux and/or wavelength shift may occur (Figure 5-6). Due to the influence from the uncertainty contributors, the light output from the V8 light engine cannot provide the desired target light. The graph in Figure 5-14 is a comparison between the three resultant SPDs obtained from a pre-calibrated lookup point (as target), uncontrolled light output (due to uncertainty parameters), and a new pre-calibrated lookup point (for controlled light output) at 5500 K. As shown in the graph, due to wavelength shift in the system from the target, the SPDs for controlled light adjust correspondingly and shift in the wavelength space compared to the target light. However, the controlled light output delivers the desired light output which is closer to the target CCT and the target Φ_V.
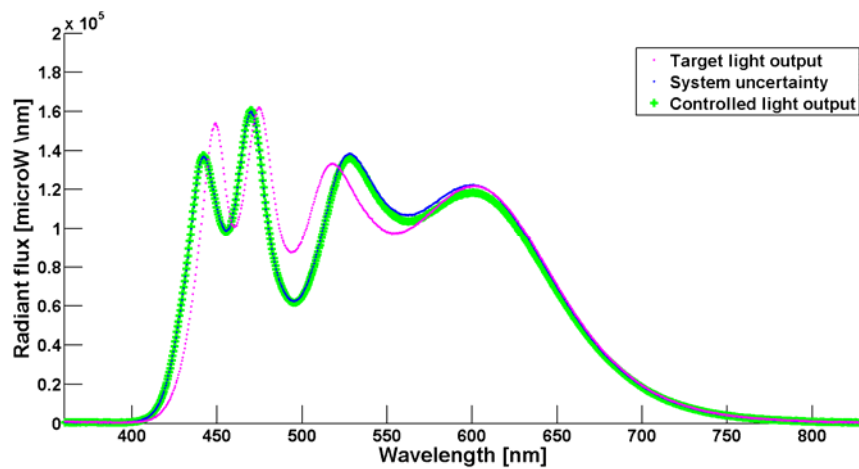
Figure 5-14: Compared SPDs between target, before and after implementing the control system

From the resulting 2000 SPDs, the chromaticity coordinates (u´, v´) are calculated. The probability distributions of variations in CCT and D_{uv} for 2000 systems are derived and are shown in Figure 5-15(a)-(b). The coverage interval of 95 % from the distribution implies that $\Delta CCT = 738$ K with mean of 5709 K and $\Delta D_{uv} = 0.0252$ with mean of 0.0028, are represented by the green color in the same figure. In Figure 5-15 (c) and (d) the corresponding probability distribution of variations in CRI (R_a) and CRI (R_9) deriving from tristimulus color sensor output[119] , indicating a 95 % coverage interval by also green color have plotted. Within the 95 % coverage interval ΔCRI (R_a) = 15.4 with mean of 91 and ΔCRI (R_9) = 95.7 with mean of 43, respectively have found. Similarly, the same output parameters from Monte Carlo simulations for target CCT

settings from 4000 K to 6000 K with a target Φ_V of 8000 lm have evaluated, which is listed in Table 5-2.

Figure 5-15: (a) - (d) represent the probability distributions within a 95 % coverage interval (green) of CCT, D$_{uv}$, CRI (R$_a$), and CRI (R$_9$), respectively, for 2000 iterations while the red color is indicating the same for outside of the 95 % coverage interval (Ref. Figure 3 of Chakrabarti et. al [25])

Table 5-2 CCT and Φ_V variations within 95% coverage interval at target settings of target CCT and Φ_V respectively (Ref. Table 1 of Chakrabarti et. al [25])

Target CCT [K] at Φ_V = 8000 lm	ΔCCT [K] (uncontrolled)	ΔCCT [K] (controlled)	$\Delta\Phi_V$ [lm] (uncontrolled)	$\Delta\Phi_V$ [lm] (controlled)
4000	1020	125	737	169
4500	932	155	704	167
5000	898	211	684	230
5500	738	282	614	185
6000	836	381	653	187

From Table 5-2 it can be noticed that the uncontrolled ΔCCT and $\Delta\Phi_V$ values are higher at 4000 K compared to other CCT settings. This is because the uncertainty on the output from the red LED is highest at this setting and therefore its contribution to the uncertainty is high.

Figure 5-16 (a)-(b) represents the variation of CRI(R_a) and CRI(R_9)for the 2000 iteration by blue dots before implementing the control system and green dots after implementation the same, respectively. Here, the purple '+' represents the target values for the CRI(R_a) and CRI(R_9). As the color control system controls the color variation up to a certain level, the green dots are closer to the target value than the blue. The standard deviation of CRI(R_a) and CRI(R_9) variations are also plotted in the Figure 5-16 (a)-(b), where the blue lines (65% coverage interval) of the light output in the system are larger than the green lines (65% coverage interval after implementing the control system). Similar graphs can be plotted for Φ_V, CCT, and D_{uv}.
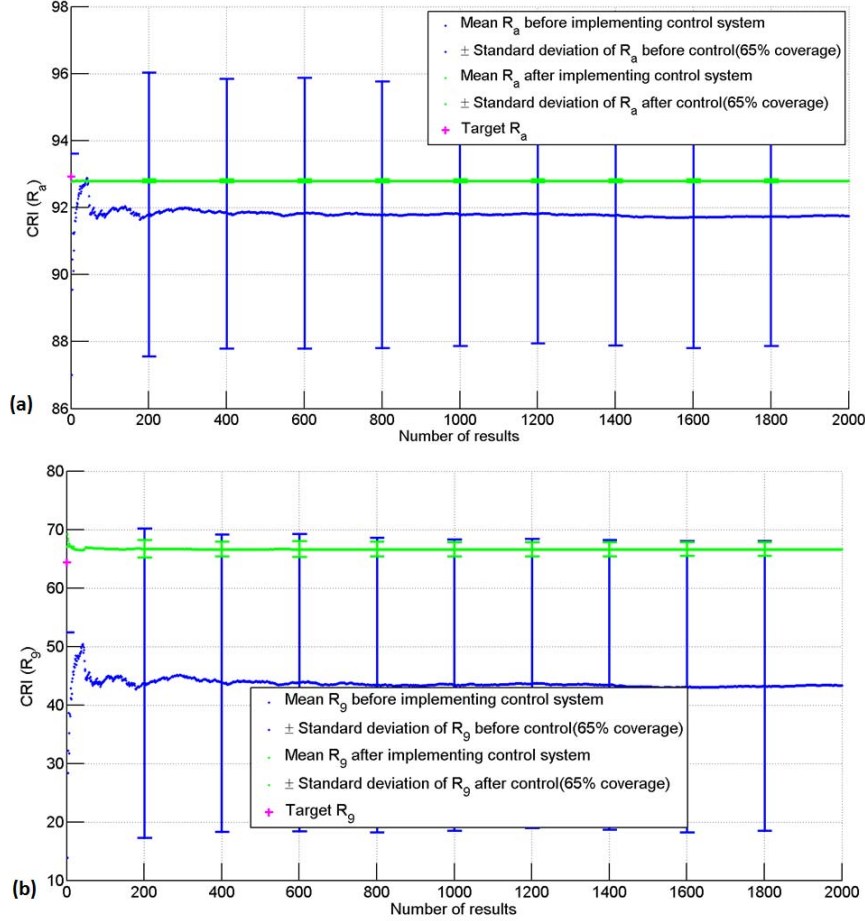
Figure 5-16: The variation of mean and standard deviation of (a) CRI (R_a) (b) CRI (R_9) for 2000 iteration for before and after implantation of the control mechanism, respectively (Ref. Figure 4 of Chakrabarti et. al [25])

Figure 5-17 shows the distribution of the four parameters for the 2000 iterations after implementing the control system. The green lines show the distribution within a 95% coverage interval. Figure 5-17(a) and (b) shows that the variation of CCT and D_{uv} has

been reduced to $\Delta CCT = 133$ K and $\Delta D_{uv}=0.0011$ within the 95% coverage interval. Similarly, Figure 5-17(c) and (d) show $\Delta R_a = 0.18$ and $\Delta R_9=4.9$ within 95% coverage interval.
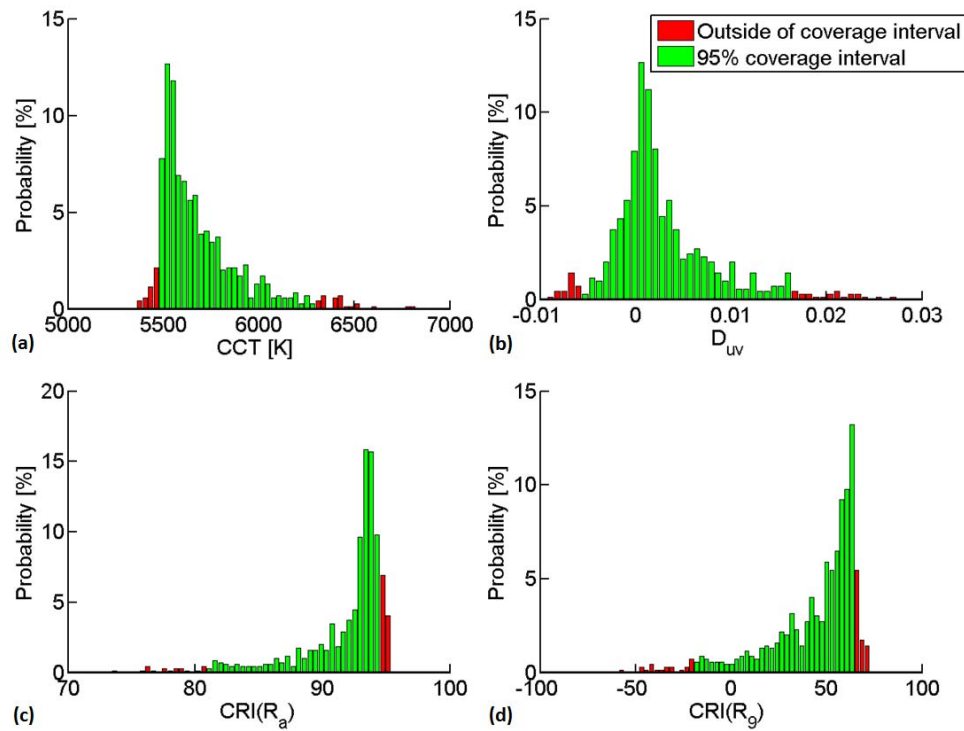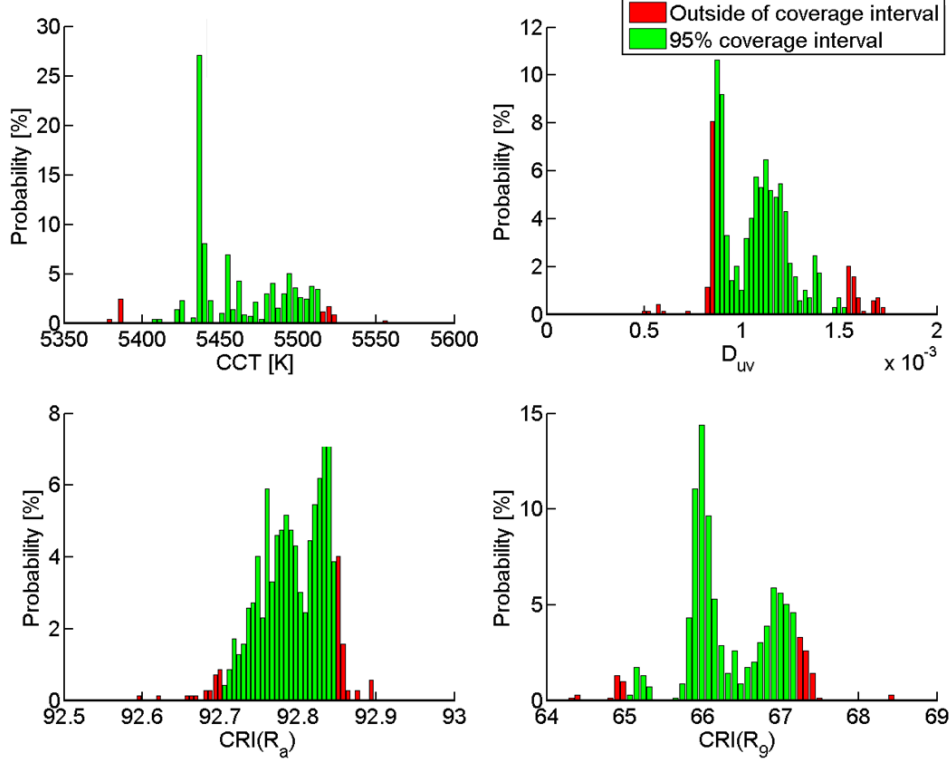

Figure 5-17: (a) - (d) represent the probability distributions within 95% coverage interval (green) of controlled CCT, D_{uv}, CRI R_a, and R_9, respectively, for 2000 iterations while the red color is indicating the same for outside of the 95% coverage interval (Ref. Figure 3 of Chakrabarti et. al [25])

Figure 5-18 indicates the working performance of the control system by showing the color variations of the 2000 iterations in the u′, v′ diagram (CIE-1976 chromaticity coordinates) before and after having the color control system inside the V8 light engine, respectively. In Figure 5-18, the isothermal line (black dash lines) demonstrates the variation in D_{uv} (ΔD_{uv}) and the Daylight locus (solid black lines) characterizes the variation in CCT (ΔCCT). Figure 5-18 also shows a JND circle (red line) and n=2 circle (dashed red line) with a radius of 0.0013 and 0.0026, respectively, [121] (u′ v′ circle defined in CIE TN001:2014) by taking the target point (purple dot) as a center point of the circle. It is clear that the target point indicate an offset from the Daylight locus. This is because the lookup point values are not optimized to D_{uv} at zero, rather; it is optimized to low D_{uv} ($< \pm 10^{-3}$) as recent findings [101], [102] show that the human preference for CCT and an optimum D_{uv} may not be at zero D_{uv}. From Figure 5-18 it is observed that the found solutions before implementing the control system (blue '.')

almost all are outside from the JND circle (red) and not even close to the target point. Similarly, the green 'o' implies the solutions for those 2000 iterations after implementing the control system in Figure 5-18. It is clear from the figure that the color control system could narrow down the variation along the Daylight locus (ΔCCT) as well as along the isothermal line (ΔD$_{uv}$). Although the all controlled points are not yet within the JND circle[46] (50% of human observer cannot preserve the color variations), 95% points are within n=2 circle. The present lookup table is made in two dimensions, by registering the variations in CCT and Φ$_V$, where each lookup point represents optimized D$_{uv}$ value (<± 10^{-3}). The future work will increase the dimension of the lookup table where the variations in D$_{uv}$ will also be stored in third dimension. The three dimensional lookup tables will resolve the issue and it will be expected that the controlled points will be inside the JND circle.
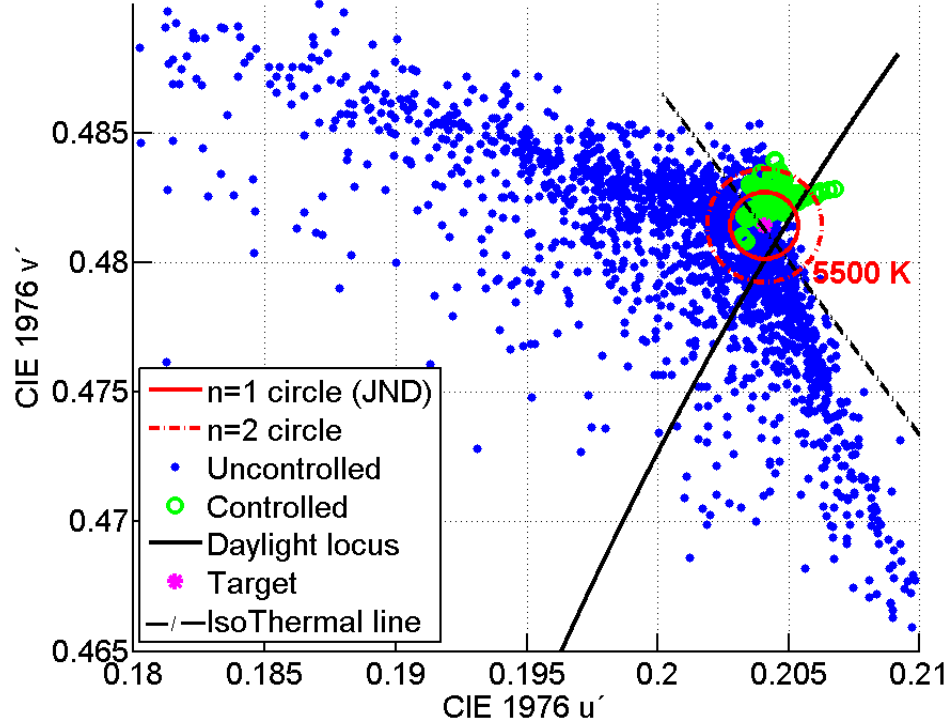
Figure 5-18: The example of uncontrolled and controlled solutions from the lighting system at 5500 K in u´- v´ diagram (CIE-1976 chromaticity coordinates) (Ref. Figure 4 of Chakrabarti et. al [25])

Figure 5-19 outlines the controlling range of the V8 light engine at Φ$_V$ = 8000 lm. The V8 light engine is tunable from 3000 K to 6000 K in steps of 100 K. The red solid square data points represents the controlled CCT value found at the corresponding target CCT and the relation between them is linear with R^2=0.965. The controlled luminous flux found at the corresponding target CCT is signified by the blue solid circle data points, while the dotted black line shows the target: Φ$_V$ = 8000 lm. Although the Φ$_V$ variation during the tuning CCT ranges from 3000 K to 6000 K, it is within ~1 %, the found CCT

values are higher than the target value at the range between 3000 K and 3500 K. This is due to the fact that within that region some lookup points inside the lookup table have had difficulty in finding the initial SPDs for the corresponding CCT settings explained earlier in section 5.2.1.

Figure 5-19: Controlled light output from the lighting system while the CCT tuned from 3000 K to 6000 K with 100 K resolution at 8000 lm (Ref. Figure 5 of Chakrabarti et. al [25])

5.4.1 Why this control technique is useful?

Although the multi-colored LED lighting systems are popular nowadays, they often suffer from poor color stability and reproducibility from system to system due to color and intensity variation over time. To address these p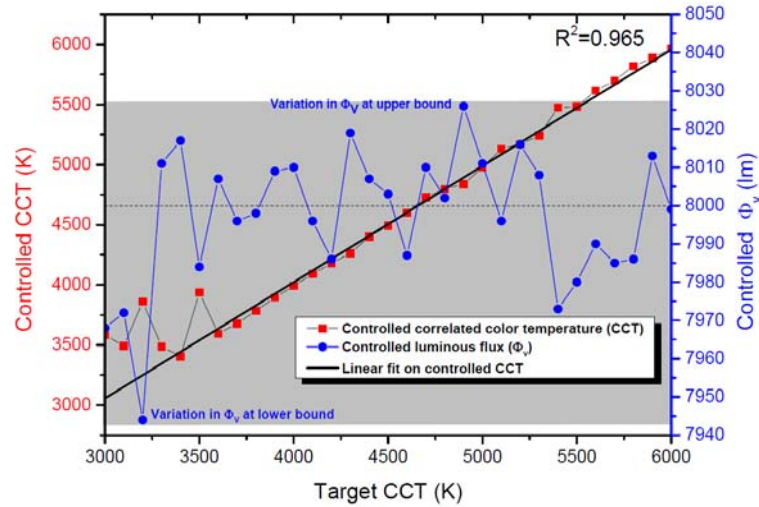roblems without compromising the efficiency and light quality, a methodology of control mechanism by introducing a color feedback inside the system, covering a wide white gamut to achieve controlled chromaticity and stability during operation time is proposed. The V8 light engine produces white tunable light output, ranging in CCT from 3000 K to 6000 K with intensity dimming capability of minimum 13 % lower on 8000 lm at each CCT setting. The color control system implemented into the V8 is a combination of a pre-calibrated lookup table utilizing a set of previously optimized settings for each target CCT and a calibrated color sensor for chromaticity control. The pre-calibrated lookup table is made by an algorithm which stores the resultant SPDs as a lookup point from the spectral mixtures of five colored LEDs, optimized to low D_{uv} and a high general color rendering index (CRI) of $R_a > 85$ and a specific CRI $R_9 > 40$ for rendering the strong red objects. The color control system is statistically analyzed using a Monte Carlo simulation process which simulates the SPD of the mixed light and hence variations in CCT, D_{uv} and Φ_V as output based on the uncertainties inside the input parameters (LED flux and wavelength bin, junction temperature, driving current, ambient temperature, driver

electronics, and color sensor response) of the V8 system. The uncertainties in input parameters are either found experimentally or taken from data sheets. There are not many people who use Monte Carlo for investigating the uncertainties of input parameters to evaluate uncertainties of output parameters for a dynamic system. To control these CCT and Φ_V variations, the color sensor has been implemented to provide the real time feedback from the light output. The calibrated color sensor monitors the white light output from the lighting system and evaluates on the error correction in CCT and Φ_V so that a new lookup point can be chosen to achieve the desired light output stability from the system. The long term stability and accuracy of the system has been inspected with a target tolerance within a circle radius of 0.0013 in the uniform chromaticity diagram (CIE 1976) which is recommended in CIE TN001:2014. The control system presented here does control the D_{uv} within two step just noticeable difference circle, and this will be implemented in future work. The control mechanism can be generalized to be used in any other SSL system (such as additive laser color mixing system) where instead of using the color sensor, a spectrometer may use for sensing the spectral information. Three LED color mixing systems are under development and will be used to experimentally demonstrate both system stability and system to system reproducibility. The Monte Carlo results will be compared with the experimental results and further simulation work on the uncertainty contributions due to abrupt failure of LEDs, LED aging, and contamination of the optical system will be considered. In this way it will open up new possibilities for analysis of the color uncertainty of multicolored LED systems which would easily be expandable to larger and more complex systems, without dealing with analytical propagation of uncertainties.

5.5 Color variation in laser-color mixing system

Since laser light is a potential candidate for making the spot light, as mentioned in the Chapter 4, the research area for color mixing by laser light has been investigated initially. Therefore the color variation from such a system is also considered in the part of the research and thus the idea of a speckle wavemeter is discussed. Normally the light output from the laser is sensitive to temperature[122]. Generally, there will be a temperature dependence[123] on the wavelength shift for a long operational time. This change in wavelength can be recognized by the speckle wavemeter which is inexpensive compared to the commercially available spectrometers. Therefore, instead of using the color sensor, the speckle wavemeter can provide the wavelength change in used laser of the laser color mixing system which can be converted to the (u´,v´) to provide the error correction in the feedback system of the control mechanism (explained above). The following paragraphs will elaborate on the functionality of the speckle wavemeter based on the previously published article by Chakrabarti et. al [21] and Hanson et. al[22].

5.5.1 Speckle based wavemeter

Many materials have surfaces that are significantly rough on the scale of the optical wavelength and their lateral scale usually exceeds the diameter of the illuminating spot. When a nearly monochromatic light is reflected from such a surface, the objects viewed

in coherent light acquire a granular appearance of the intensity where the structure of this granularity is chaotic and unordered with an irregular pattern that can only be described by the methods of probability theory and statistics. This pattern is named a speckle pattern [124]–[126]. Numerous applications have been presented where the displacement of this speckle pattern arising from a dynamic scattering surface is investigated. By measuring speckle cross-correlation before and after deformation of the object using a photodiode array, Yamaguchi [127]–[129] directly found strain due to small object deformations. Later, Yamaguchi et al. [130] also showed roughness measurement by calculating speckle cross-correlation before and after a change of the incident angle of a laser beam. An abundance of applications in this field is available.

Here, the cross-covariance is used between two speckle patterns obtained with only a difference in the wavelength to measure the change in the wavenumber of a laser beam, and thereby propose and demonstrate a novel attractive, inexpensive speckle wavemeter with a reasonable resolution. Brandon et. al [131] proposed a low loss spectrometer by using speckle pattern images generated by interference during propagation in multimode fibers. The standard way of measuring wavelengths is by a grating spectrometer [132], Fabry-Perot (FP) interferometers [133], wavemeters, or by heterodyne methods. In the grating-based spectrometer, light with different wavenumbers ($k - \Delta\frac{k}{2}$ and $k + \Delta\frac{k}{2}$) are deflected in directions determined by the wavelength of light. This setup is delicate if a high resolution is needed, and furthermore the temporal resolution is low. FP spectrometers are sensitive to align and the temporal resolution is usually limited. This method is based on allowing the light to pass between two highly reflective mirrors with a variable distance. When the mirror spacing match an even number of standing waves, the resonant wavelength will pass, and the wavelength can be found within certain limitations, but unfortunately with a redundancy given by the so-called free spectral range (FSR) of the FP interferometer. Compared with other expensive spectrometers, the proposed speckle wavemeter is simple and providing the possibility of a high temporal resolution and a reasonably good spectral resolution, however, only providing changes in wavelength. In this way, the proposed precise system is comparable with the FP interferometer without some of its limitations. The following section will provide the basic theory for the system, supported by two simple experiments.

Figure 5-20 shows the basic setup, here for free space propagation. A coherent incident beam illuminates the surface at an oblique angle and the speckle pattern is observed with a CMOS array, being it linear or 2D, placed at a distance L. As the wavenumber is changed, the speckle pattern will shift laterally, as shown in the following. For the sake of theoretical simplicity, the incoming and outgoing beams are supposed to be in the same plane, as is the normal to the scattering surface.
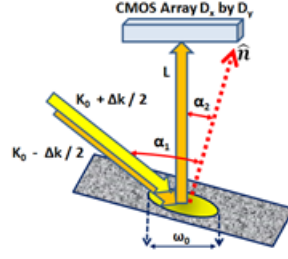
Figure 5-20: Experimental setup for probing wavelength changes by observing the speckle displacement (Ref. figure 1 of Chakrabarti et. al [21])

The cross-covariance $C\left(\mathbf{P}, \Delta\mathbf{p}; k, \Delta k\right)$ between the speckle pattern - before and after a shift in wavenumber - is given by the equation (48).

$$C\left(P, \Delta p; k, \Delta\frac{k}{2}\right) = \left\langle I\left(P - \frac{\Delta p}{2}; k - \frac{\Delta k}{2}\right) I\left(P + \frac{\Delta p}{2}; k + \frac{\Delta k}{2}\right)\right\rangle \qquad (48)$$
$$- \left\langle I\left(P - \frac{\Delta p}{2}; k - \frac{\Delta k}{2}\right)\right\rangle \left\langle I\left(P + \frac{\Delta p}{2}; k + \frac{\Delta k}{2}\right)\right\rangle$$

where the variable shift of the intensity I is given by $\Delta\mathbf{p}$ and the center of the CMOS array is positioned at $\mathbf{P}$. Angular brackets indicate "ensemble averages". Assuming the field to obey circular symmetric statistics – i.e. assuming the speckle field to be fully developed – the cross-covariance of the intensities can be reduced to calculating the simpler field correlation:

$$C\left(P, \Delta p; k, \Delta\frac{k}{2}\right) = |\langle U(P - \Delta p/2; k - \Delta k/2)U^*(P + \Delta p/2; k \qquad (49)$$
$$+ \Delta k/2)\rangle|^2$$

The field scattered off the surface (**r**-plane) and observed in the CMOS plane (**p**-plane) can be written as:

$$U(p; k) = -\frac{ik}{2\pi B}\int_{-\infty}^{\infty} dr \psi(r) U_{in}(r) \qquad (50)$$
$$* \exp\left[-ikx\left(sin(\alpha_1) + sin(\alpha_2)\right)\right.$$
$$\left. * \exp\left(-\frac{ik}{2B}\left(Ar^2 - 2r.p + Dp^2\right)\right)\right]$$

Here the scattering phases $\Psi(\mathbf{r})$ will be assumed delta – correlated in accordance with the surface giving rise to a fully developed field, i.e. the ensemble average being $\left\langle\Psi(\mathbf{r}_1)\Psi^*(\mathbf{r}_2)\right\rangle \propto \left(4\pi/k^2\right)\delta(\mathbf{r}_1 - \mathbf{r}_2)$. The ensemble average is denoted by angular brackets

and the incident deterministic field is $U_{in}(\mathbf{r})$. The linear phase of the incident beam and the outgoing beam is $kx\sin[\alpha_1]$ and $kx\sin[\alpha_2]$, respectively, having assumed that the scattering and incident wavevectors lie in the x-plane. In order to track the field from the rough surface to the detector array, we here use the matrix formalism [134], [135], where the Green's function is given by the complex numbers *A*, *B* and *D* defining the optical system as $-\frac{ik}{2\pi B}exp\left(-\frac{ik}{2B}(Ar^2 - 2r.p + Dp^2)\right)$, including apertures (Appendix C). In this formalism all apertures are assumed Gaussian apodized. Two optical systems are treated here, namely free space propagation *A*=1, and *D*=1 and a Fourier transform system with the scattering surface in the front focal plane of a lens with focal length *f* and the CMOS array in the back focal plane, without any apertures *A*=0, and *D*=0. An analytical expression for the cross-covariance can now be obtained by inserting the expression of equation (50) in the expression for the cross-covariance in equation (49) taking into account the delta – correlation of the scattered field. A common factor in front of the cross-covariance has been omitted as it carries little information on the speckles and their dynamic behavior. Further, the result is given for the center of the detector array, i.e. P=0. For optical systems without apertures, the on-axis covariance becomes then:

$$C(0, \Delta p; k, \Delta k) \propto exp\left[-4\frac{(\beta B\Delta k - k\Delta p_x\cos(\alpha_2))^2\cos(\alpha_1)^2\omega_0^2}{16B^2\cos(\alpha_1)^4 + A^2\Delta k^2\omega_0^4}\right] \quad (51)$$

This expression is valid for a collimated incident beam of width ω_0 (1/e2 intensity radius). The scattering wavevector in the plane of the object is given by β where $\beta = \sin(\alpha_1) + \sin(\alpha_2)$. The peak position Δp_{x0} for the cross-covariance reveals the change in wavenumber given by

$$\Delta p_{x0} = \frac{\beta B}{k\cos(\alpha_2)}\Delta k \quad (52)$$

In case of a free space system, as depicted in Figure 5-20, the *B*-element equals the optical length *L*, and *A* is the magnification, herein unity. In case of a Fourier transform system, an intermediate lens is located between the surface and the CMOS array placed in the back focal plane of the lens. Here, the *B*-element equals its focal length *f* and *A*=0. In case a limiting aperture is included for a Fourier transform system, a very minor change in the speckle displacement given by equation (52) will occur.

It is noticed that a slight uneven displacement is observed, as a function of the position in the observation plane, which would be revealed by writing the full expression in equation (51) where $\mathbf{P} \neq \mathbf{0}$. In fact, the speckle pattern expands from the point where the light reflected off the surface would hit the plane of the CMOS array, had the surface not been specularly reflecting. The effect of an uneven speckle displacement will thus decrease as the projection of the scattering wavevector in the object plane increases, which fortuitously corresponds to the ratio between speckle displacement and change in wavevector being largest, i.e. the configuration giving the

highest sensitivity. Besides, a finite curvature of the incident beam will not influence the scaling derived in equation (52), neither will it change the speckle size. But, needless to say, a high degree of mechanical stability is required, as is the case for a majority of interferometers. A slight change in angle of the incident beam between the two exposures will give rise to an error in the determination of the shift in wavevector as will an in-plane displacement of the object in case of a free space propagation setup. In the Fourier transform case, only a change in angle will give rise to a shift in the speckle pattern. A linear displacement of the scattering structure will in this case only give rise to speckle decorrelation.

For free space propagation, equation (51) will give the speckle size by the width of the cross-covariance in Δp_x for $\Delta k = 0$. The speckle size becomes $2L\cos[\alpha_1]/(K_0\omega_0\cos[\alpha_2])$. In the same way, the decorrelation due to a change in wavenumber is given by $\Delta k_{decor} = 4L\cos[\alpha_1]^2/\omega_0^2$, in good agreement with the known expression for the length of the speckles. One experiment was carried out in order to verify the concept. A collimated beam from a vertical cavity emitting laser (VCSEL, type TO 510) emitting at a wavelength of 760 nm was used giving an almost collimated beam at the target, here being a sandblasted aluminum plate. The speckle patterns were recorded with a CMOS array (1024 x 1280 pixels, pixel distance of 5.2 μm). The speckle images were recorded successively after changing the desired parameter for the VCSEL, after which the cross-covariance between the two recordings was calculated and the peak position found with a Gaussian fitting procedure. A representative speckle recording is shown in Figure 5-21. The displacement incurred during a change of wavevector is horizontal in Figure 5-21, i.e. along the minor axes of the ellipsoidal speckles. The elongation of the speckles is due to the grazing angle of the incident beam, here being $\alpha_1 = 85^0$. The angle of observation was $\alpha_2 = 30°$, and the diameter of the illuminating beam – before incidence – was approximately 1 mm. The distance from the object to the CMOS array was 20 cm.

Figure 5-21: Speckle pattern from a slanted object resulting in a needle-like speckle pattern (Ref. figure 2 of Chakrabarti et. al [21]**)**

A series of recordings were made with a constant current applied to the VCSEL. At the same time, the VCSEL temperature was changed with a Peltier element placed next to the VCSEL. A calibrated thermistor was placed next to the VCSEL and the temperature was changed and subsequent speckle images were acquired for various temperatures

after a stable temperature was obtained. A two-dimensional correlation was performed with subsequent images and the peak position of the correlation function was found with sub-pixel accuracy by Gaussian fitting of 7 pixels and 42 pixels in the horizontal and vertical direction, respectively, about the peak pixel value. The speckle width was 3.5 pixels, FWHM and the height, perpendicular to the direction of movement, was 39 pixels. It has to be noted that the entire 2D covariance function is used for estimating the speckle shift. Mathematica software is used to compute the various Correlation functions of speckles. The peak location is detected by centroid and parabolic fitting after doing Fourier transform of two images as shown in Figure 5-22. At that moment it is not done by real time. However, the process is taking less than 1 minute.
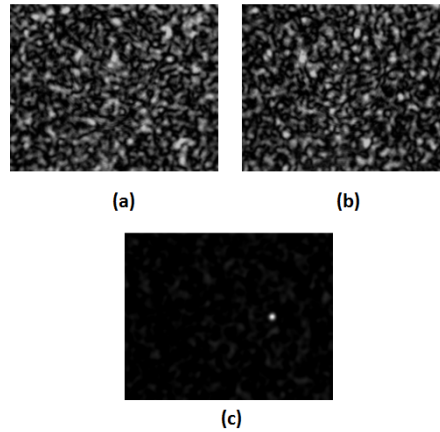

(a)   (b)

(c)

Figure 5-22: Speckle pattern of (a) first image (b) second image (c) cross correlation
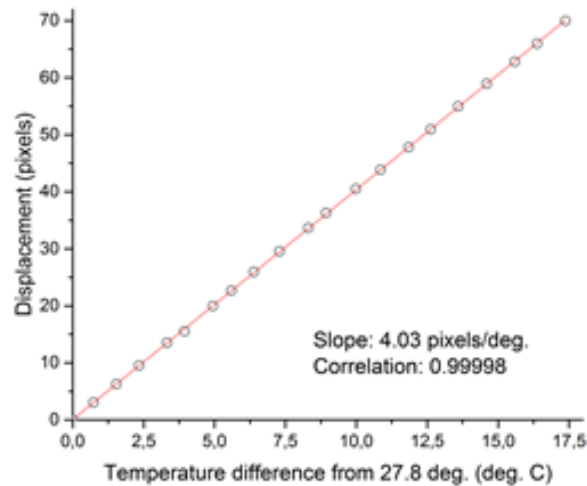
Figure 5-23: Change in peak position of the cross-correlation function measured in pixels as a function of the change in VCSEL temperature for constant injection current (Ref. figure 3 of Chakrabarti et. al [21])

Figure 5-23 shows the result where the speckle pattern is shifted as a function of the temperature change in injection current. The first reading was for a temperature of 27.78 °C, and the last reading was made at 45.16 °C. In this setup, a change in peak position of one pixel corresponds to a change in wavelength of 11.44 picometer, where 1 picometer wavelength change corresponds to a frequency change of 520 MHz at this wavelength. The recording was made by correlating all speckle patterns with the first one acquired at the lowest temperature, and subsequently finding the peak positions for each of following. The measured change in wavelength as a function of the temperature becomes 46.1 pm/ °K, where the specification for the VCSEL reports a typical value of 55 pm/ °K. The injection current, at which this was stated, was not stated by the manufacturer. Figure 5-24 shows the result where the speckle displacement is displaced as a function of the change in injection current. In this setup, a change in peak position corresponds to a change in wavelength of 25.3 picometer. The measured change in wavelength as a function of the change in injection current becomes 0.706 nm/ mA, where the specification for the VCSEL reports a value of 0.3 nm/ mA. In this experiment, the temperature of the VCSEL was not kept constant, which could explain the difference.
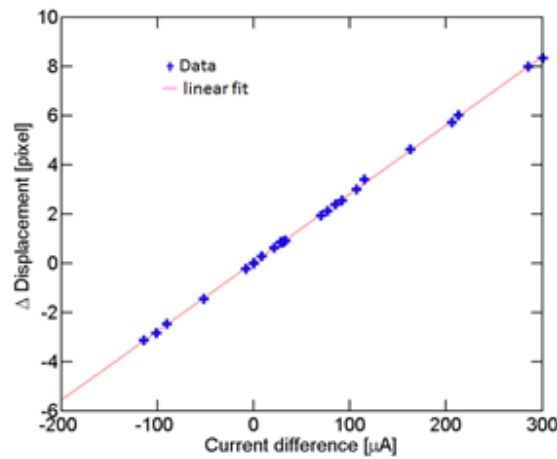
Figure 5-24: Change in peak position of the cross-correlation function measured in pixels as a function of the change in VCSEL injection current (Ref. Figure 3 of Hanson et. al [22])

The change in the emitted wavelength as a function of the natural heating of the VCSEL was found at a constant injection current. Hence, a series of measurements were obtained by acquiring a data point for every 30 seconds. The first speckle recording was used as a reference with which the following 9 recordings were correlated. The temporal change in pixel displacement is shown in Figure 5-25. The specification for the VCSEL calls for a thermal change in wavelength of 60 picometer/ °K. Using this value, the heating of the VCSEL for the given injection current is 10 m°K/sec.
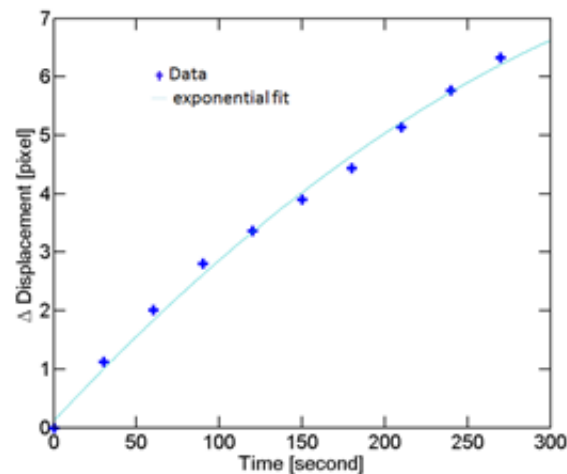

Figure 5-25: Temporal change of the peak pixel position as a function of time, here giving a wavelength change due to natural heating of the VCSEL (Ref. Figure 4 of Hanson et. al [22])

The sensitivity of the system heavily relies on the accuracy, with which the speckle displacement can be probed. According to Zhou [136], an accuracy of 0.005 pixel can be obtained by developing an iterative, spatial-gradient based algorithm, by using only first-order spatial derivatives of the images before and after deformation. Later, a method based on new algorithms for 2D translation image registration to within a small fraction of a pixel that use nonlinear optimization and matrix-multiply discrete Fourier transforms were put forward [137]. Here, accuracy for a fast method for 2D correlation gave an accuracy of close to 0.01 pixel. If the results form Figure 5-23 are used and no error is assumed in the temperature measurement and furthermore, a totally linear dependency of the wavelength versus temperature relation are assumed, the accuracy in that experiment would become 0.03 pixels. This again would correspond to a measurement accuracy of 180 *MHz*.

5.5.1.1 Utility of the speckle wavemeter

Therefore a novel, yet simple, speckle-based wavemeter aimed at measuring minor changes in wavelength have been presented here. Experiments that support the validity of the method have been given, although no attempt has been given in order to obtain the ultimate accuracy achievable. An accuracy of at least 100 MHz can be obtained by using a CMOS array with a higher number of pixels and having a setup where the incidence and observation angles as well as the spot size on the target are further increased. Finally, the use of a 1D correlation function row by row with subsequent averaging will further increase the sensitivity.

The standard way of measuring wavelength changes would be with a commercial scanning Fabry-Perot interferometer, with which a resolution of down to 7.5 MHz. but with the drawback of having a free spectral range of 1.5 GHz in case of a finesse of 200. A delicate alignment is needed, and a series of concave mirrors have to be acquired in order to cover the visible and near-infrared regime. The scan time for FP interferometer is given by the mechanical response of the mechanical system and the controller. Here a scan time of 10 msec. is representative, as it will be for the time interval between recordings with a CMOS array. In this way, the present system is inferior to a FP-system with respect to resolution, but its realization is simpler.

Although the speckle wavemeter cannot detect the wavelength change in the LED based system, it can easily detect the temperature dependent wavelength change with in the laser-based color mixing system with an accuracy of a picometer during the operation time. Knowing the average wavelength of the incident radiation, the shift in wavelength is tacitly given by the physical parameters of the setup, i.e. the angle(s) of incidence and the distances. The absolute wavelength of the incident radiation can be coarsely determined by the speckle size, but in real applications, the incident wavelength has to be known. If one allows two measurements of the speckle pattern, between which some physical parameter has been changed (e.g. distance, tilt of object), the absolute wavelength might be derived with a higher accuracy.

5.6 Summary

The variations in color properties and light intensity are due to the uncertainties in LED binning and aging, operational and environmental conditions, etc. This chapter reports the development of a Monte Carlo simulation process to analyze color variations of the multi-colored LED lighting system. This is needed for e.g. studio lighting where variation in color from lamp to lamp and stability over both short and long time are critical and should be controlled to certain limits. The development of the simulation is done for a white tunable V8 light engine, using the experimentally measured sensitivities of individual colored LEDs with respect to uncertainties in input parameters which are fed into the simulation process. The Monte Carlo simulation provides the resultant uncertainty of the chromaticity for the tunable CCT range of the V8 light engine. It is analyzed in the Uniform Chromaticity Scale Diagram comparing the variations in chromaticity differences with the "n-step u' v' circles" for visually noticeable variations (varying from n = 3-8 circles corresponding to the n-step MacAdam ellipses for the target CCT settings 3000 K to 6000 K) and will also be important to compare to TV camera sensitivities. This information is used in the color control system in real time to narrow down the uncertainty by using a pre-calibrated lookup table and a calibrated color sensor for feedback. In future it is aiming to incorporate the uncertainty of individual LED life time and failure mode. There is also a plan to validate the control system experimentally on three similar kinds of systems. The Monte Carlo method is used to evaluate the uncertainties of the output parameters for the V8 light engine, which are finally used as input for the color control system so that dynamically output parameters can be controlled within acceptable variation e.g. within a just noticeable chromaticity difference circle as defined in CIE TN001:2014. The results show that the stabilized system decreases in the average uncertainty within 95% coverage interval on luminous flux from 8.5% to 2.3% and similarly reduces the uncertainty on the CCT at 4000 K from 1020 K to 125 K. Lower reductions in the CCT uncertainties are observed at higher CCTs. The present control mechanism control the light within a certain limit so that the control point in the CIE 1976 (u',v') diagram would be within n=2 circle, taking the target point as the center of that circle.

The effectiveness of the proposed control mechanism is that the control mechanism can use in any SSL system. Therefore, instead of using the color sensor, a novel and inexpensive speckle wavemeter is proposed to use in the laser color mixing system which can indicate the wavelength variation in the laser system as a feedback to the control unit. The wavelength change can be converted to (u',v') for further analysis purpose. It is experimentally verified that the minimum variation in wavelength of the order of the pico-meter can be detected by the speckle wavemeter.

The following chapter will elaborate on the experimental investigation and the corresponding results related to the V8 light engine.

Experimental investigation of V8 light engine

'At the beginning of all experimental work stands the choice of the appropriate technique of investigation.' – Walter Rudolf Hess
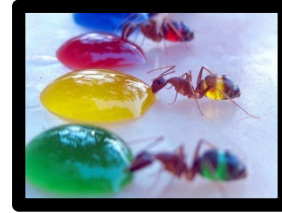
Chapter 6 : Experimental investigation of V8 light

engine

6.1 Introduction

The previous three chapters have elaborated on the V8 light engine and it's characteristics as a multi-colored tunable white light source [138]–[143] which can be applied into stage lighting. This chapter studies the experimental validity of the V8 light engine design by evaluating the light output from the prototype of the design. There will be a comparison between the luminaires which are available on the market for stage lighting application. The chapter also registers the experimental results and data analysis for characterizing the different components used for the V8 light engine design.

6.2 Forward luminous flux measurement for LED

This section will register the experimental results for the light output from the individual 5 different types of LED print circuit boards, using the 1 m IS according to the CIE standard [40] mentioned in the section of 1.5.1.1 in Chapter 1. The light was coupled through the side port (15 cm diameter) in a forward flux configuration (as seen in Figure 6-1) and a self-absorption correction was applied. The experimental results are compared to the respective datasheet values [103]–[105] and there is a good agreement with a ~7% variation. Figure 6-2 represents the value of luminous flux when the driving current is ramping up with 50 mA step. The figure indicates that the increased driving current almost linearly increases the luminous flux from the individual LED except for the green and white LEDs. The experimental results are later used for evaluating the TIR lens loss discussed in the section 6.4.
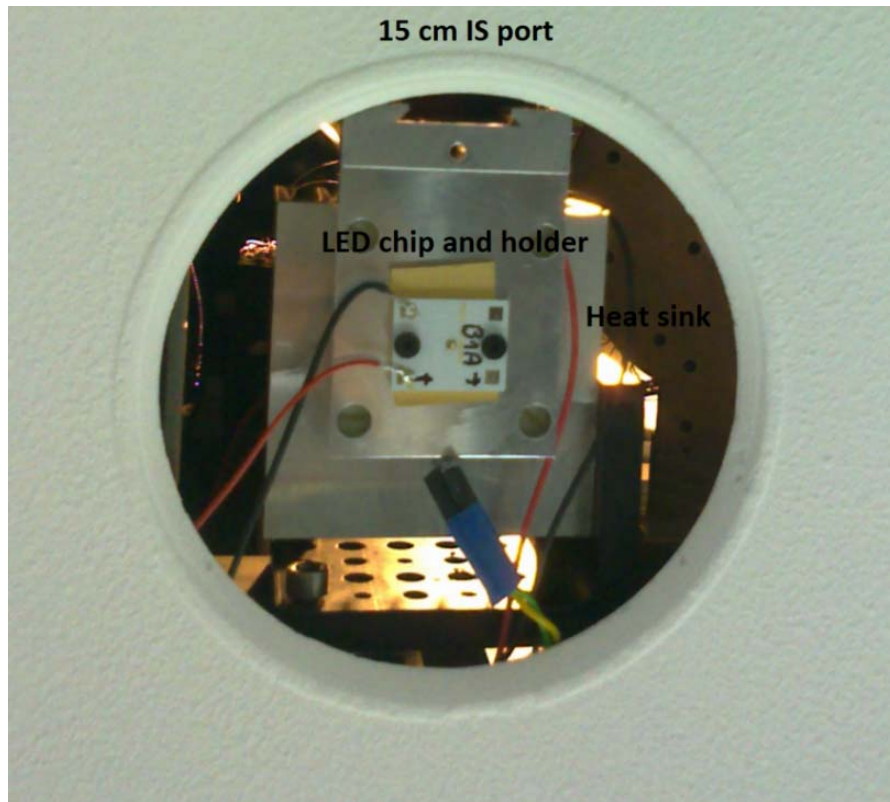
Figure 6-1: Experimental setup showing the IS port
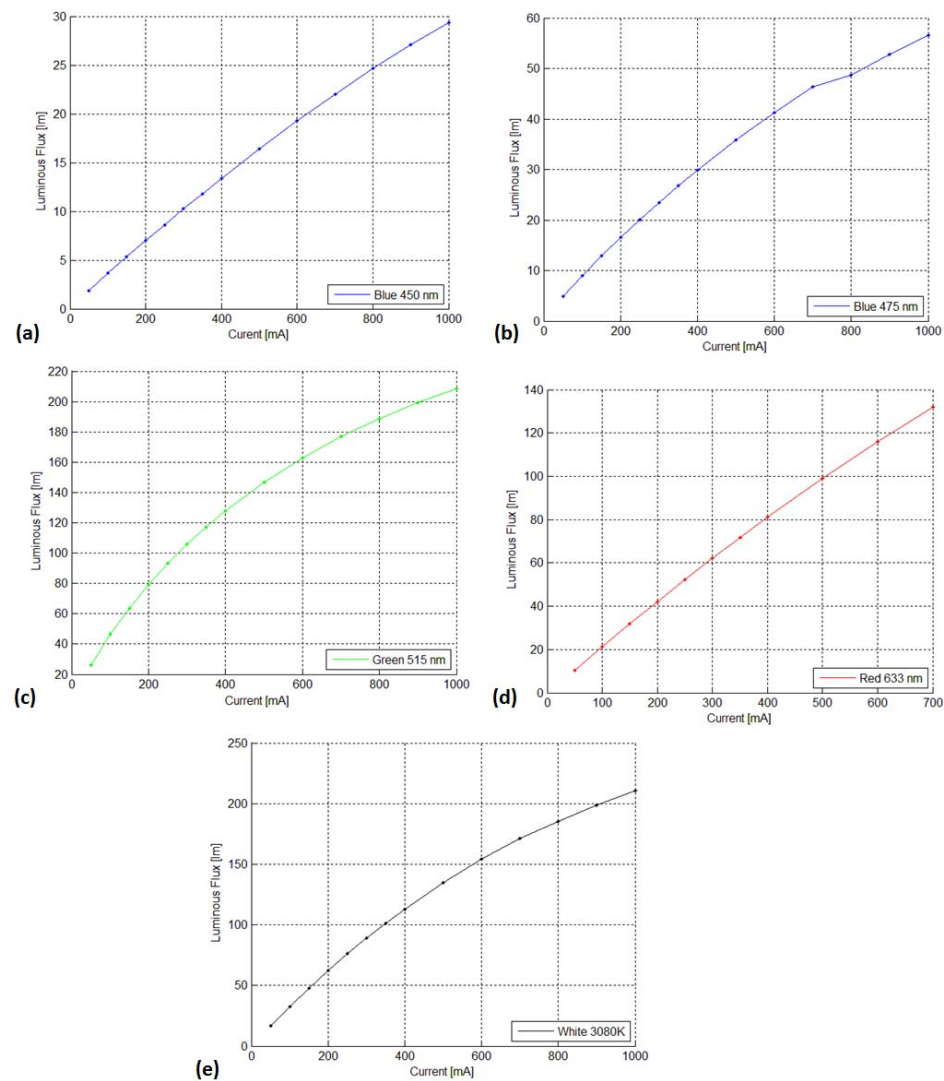
Figure 6-2: The relation between the driving current and the luminous flux from the individual LED at case temperature 25° C

Table 6-1 represents the luminous flux while the driving current is set at 350 mA, 500 mA, 700 mA and 1000 mA, respectively, with a case temperature at 25 °C for the individual LED. The temperature is maintained at 25 °C by a Peltier temperature controller. The similar experiment setup is shown in Figure 6-3. To check the LED bin consistency, another print from each LED type has been measured. It was observed that the red LED has maximum variation (~12%) between two LED print circuit boards.

Table 6-1: Experimentally measured luminous flux @ 25° C case temperature

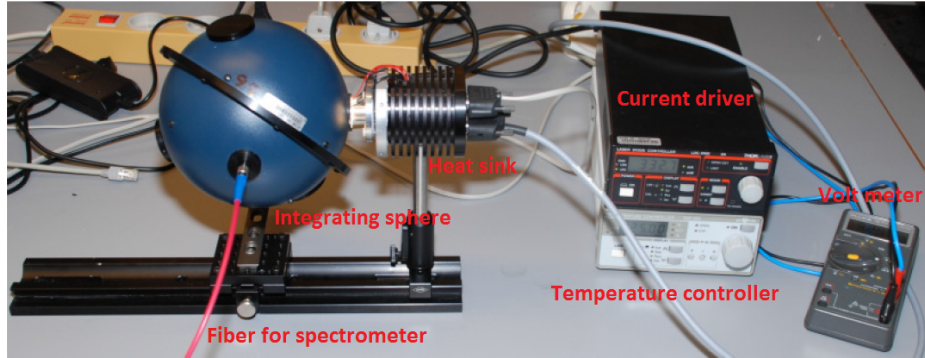| LED type	LED colors	Luminous flux [lm] @ 350mA	Luminous flux [lm] @ 500mA	Luminous flux [lm] @ 700mA	Luminous flux [lm] @ 1000mA
Luxeon Z	Royal blue	13	18	24	33
Luxeon Z	Blue	30	40	52	66
CREE XPE	Green	122	153	186	220
CREE XPE	Red	70	97	125	125 (@700mA)
CREE XPE2	White	102	136	174	218

Figure 6-3: Experimental setup for forward flux measurement from LED at varying current when case temperature is at 25 °C

6.3 Reflectance from the parabolic reflector

The parabolic reflector of the prototype has been tested for its reflectance property and the uniformity of the surface. There is a relative luminous flux measurement done by using 1 m IS. The used collimated white source for the experiment had known luminous flux values which are measured through the forward flux measurement using IS (explained in 1.5.1.1 in Chapter 1) and then the same source was measured after reflecting from the parabolic reflector. The results for those two instances are compared to find out the reflectance which is already shown in the section 3.3.2 in Chapter 3. The surface uniformity of the reflector has been analyzed by comparing the reflectance values from the different parts of the reflector.

6.4 TIR lens loss

TIR lens is a critical component of the V8 light engine. Normally the LED has a large viewing angle (~110° - 130°) and is difficult to collimate. However, TIR lenses are used in the design of the V8 light engine to get collimation of the LED beam after transmitting from the TIR lens. The optical loss from the TIR lens has been characterized separately for two sizes of lenses. The experimental setup is seen in Figure 6-4.
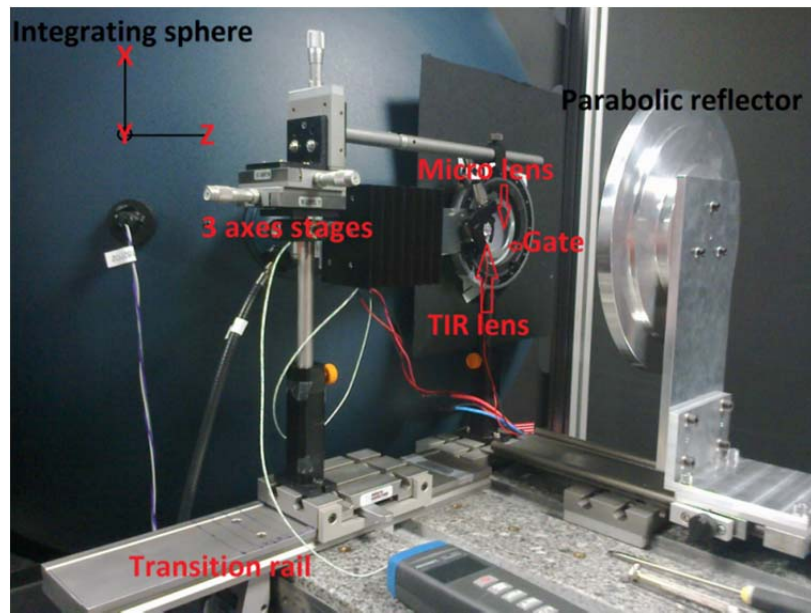
Figure 6-4: Experimental setup for the lens efficiency measurement inside the V8 light engine

According to the experimental setup, the LED beam is transmitting through the TIR lens, gets reflection by the parabolic reflector which is situated at the focal plane distance (reflector) from the lens position. The reflected beam passes through the microlens array (MA), placed at the gate and then enters into the IS. The transition rail is used to set the lens at a time to the center of the gate following the ring position inside the V8 light engine (Figure 3-1 (b)). Thus, the nearest position is considered 32 mm from the center of the gate. The three axes micrometer transitional stage is used so that the LED print circuit board can be at the middle of the TIR lens and the TIR lens can sit on the print. The blue and the white LEDs are used for the experiment as the blue LED print circuit board is smaller than the white LED print circuit board. The driving current of the LEDs was 1000 mA. To evaluate the lens loss, luminous flux values of the LEDs are compared and measured applied with and without the TIR lens. The experimental results and related analysis are already discussed in Chapter 3, section 3.3.3. The optical efficiency in Figure 3-10 shows the losses due to the position of the lens from the gate. However, the above mentioned loss is mixed with the reflection loss from the reflector as well as the ray cone. The ray cone is created because the reflector is situated ~170 mm away from the gate having Ø50 mm. Therefore, to find the loss based only on the TIR lens as well as the ray cone, another experiment is arranged (Figure 6-5).
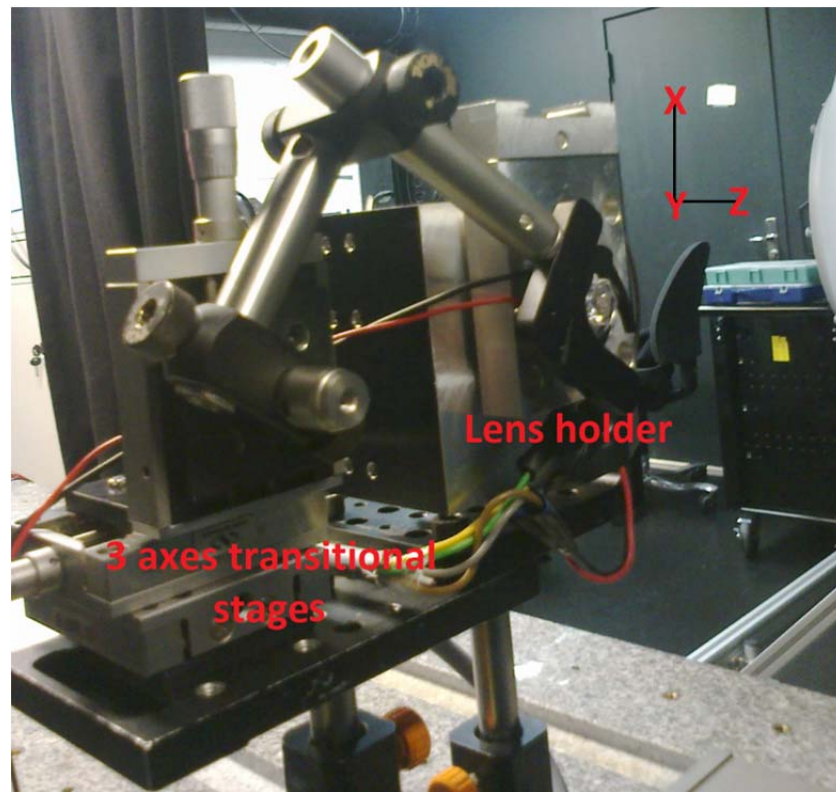
Figure 6-5: Experimental setup for TIR lens loss measurement

The Figure 6-6 shows the optical efficiency obtained from the TIR lens (big lens with size 12.7 ± 0.2 mm) while the lens holder in Figure 6-5 is placed at a particular distance away from the IS (2cm, 14 cm, 19 cm, 29 cm, 39 cm and 58 cm) to produce the corresponding ray cone considering five different LEDs. With 100° ray cone, almost all transmitted light from the TIR lens enter into the IS. Therefore the optical efficiency is ~80% for the five different LEDs. That includes the Fresnel loss from the TIR lens and the ray loss due to the geometry of the TIR lens (as seen in Figure 3-8). As we know, the optical efficiency starts decreasing as the ray cone decreases. From a ray cone of <20°, the optical efficiency for the green, the red, and the white LEDs are less than the royal blue and the blue LEDs. This is because the LED print circuit board is smaller for the blue and the royal blue LEDs than other three LEDs. According to the V8 light engine design, a ray cone ~15° is expected and shows good agreement with Figure 3-10 (b) when the TIR lens is situated at the first ring. Similarly, the TIR loss has been also characterized for the small lens size (11.7 ± 0.2 mm).
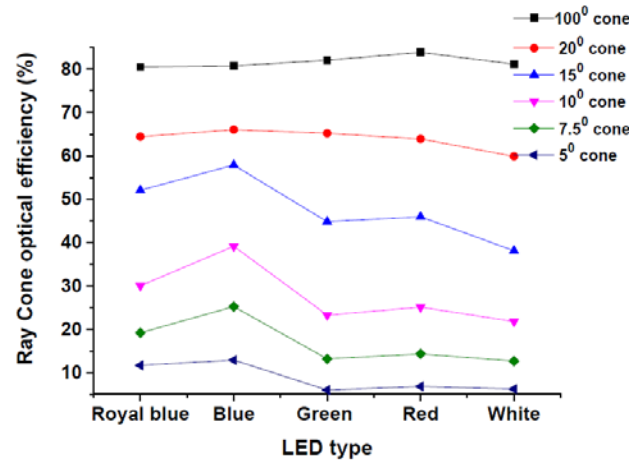
Figure 6-6: Loss characterization from the TIR lens

6.4.1 TIR lens tolerance

There was a thorough investigation on the tolerance of the TIR lens. By using the three axes micrometer transitional stage (seen in Figure 6-6), the optimized position of the TIR lens for three axes with respect to the blue LED print circuit board is found which corresponds to the maximum luminous flux transmitted from the TIR lens. The tolerance of one side for the X, Y, and Z axes are 0.51 mm, 0.4 mm, and 0.36 mm, respectively, (Figure 6-7) while the transmission loss is 10% of Full Width at Half Maximum (FWHM). Similarly, the white LED print circuit board shows the tolerance values for the X, Y, and Z axes 0.64 mm, 0.6 mm, and 0.64 mm, respectively, while the transmission loss is 10% of FWHM.
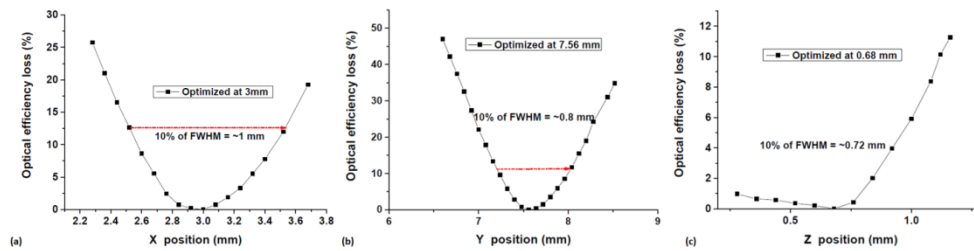
Figure 6-7: TIR lens tolerance for the optical efficiency loss

6.5 Color sensor and related measurement

The color sensor used for the control mechanism is a development kit DK MTCS-INT-AB4 of MAZeT (Figure 6-8), and includes the OEM MTCS-INT-AB4 sensor board, fitted with optical interface, a standard I^{2}C-to-USB converter, as well as software. The software enables to control the converter, calibrate the sensor and allows data logging options[144], [145]. The OEM sensor board MTCS-INT-AB4 is a small PCB for general

color measurement and control applications, includes a True Color sensor (MTCSiCF XYZ color sensor) based on the interference sensor technology, having functionality on color teaching, relative color measurement, and absolute color measurement. The color measurement based on DIN 5033 colorimetry with international standard observer CIE 1931 spectral function, a special analog-to-digital converter MCDC04EQ with a high dynamic range (1: 1,000,000), an EPROM for sensor data, an integrated temperature sensor, 2 LDO micro power regulators (LT1761ES5-3, Linear Technology) to manage the analog, and digital supply voltage. I^2C is required for the external communication, configuration of the sensor, readout of the sensor data, as well as writing and reading of the memory. The OEM sensor board uses a standard I^2C-to-USB converter for initial testing reasons via USB and PC software. The converter IOW24-DG is connected to the sensor board via cables and controls uncritical functions (not synchronized) of the sensor board via PC.
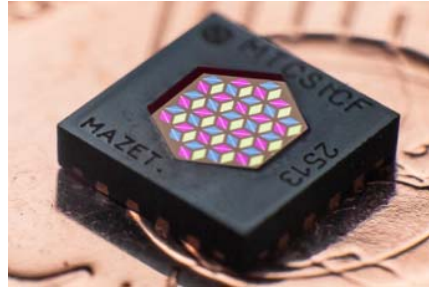

Figure 6-8: Jencolor (DK MICS-INT-AB4) true color sensor from MaZet

6.5.1 Calibration of the color sensor

In the V8 application, the color sensor is connected through USB cable and monitors the generated white light from the V8 light engine and provides the corresponding data to the control mechanism of the V8 light engine for processing internally(as seen in Figure 5-11). However, the reading from the color sensor is calibrated with the handheld GS-1150 spectrometer[118]. Initially, the different monochromatic as well as the white light (covering the warm, neutral, and cool white light regions) are measured by the handheld GS-1150 spectrometer (in total 32 sets of measurements) and corresponding (x,y) coordinates of measured light are plotted in the CIE 1931 diagram in Figure 6-9. Simultaneously, the same light is measured by color sensor also. Figure 6-10 shows the experimental setup for the color sensor calibration. In the figure, the lightbox is able to provide the desired light (monochromatic/white) which is seen by a 2° observer window (according to CIE 1931) of the spectrometer as well as the color sensor. The illuminating plane was the same for the spectrometer as well as the color sensor and the lightbox is providing the uniform light throughout the illuminating plane so that the spectrometer and the color sensor can see the same LID coming from the lightbox. The measured data by the spectrometer as well as by the color sensor are logged into the PC through the USB cables for the further process.
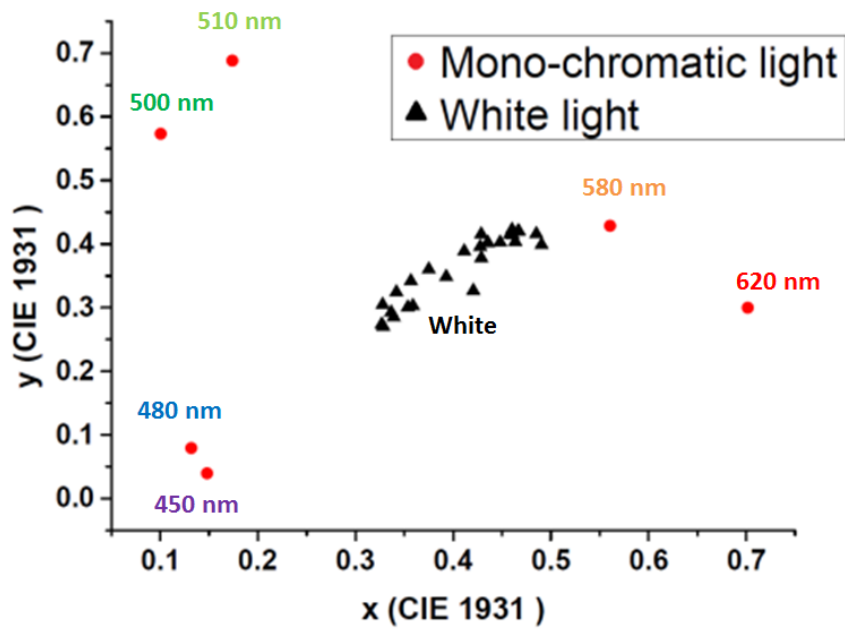
Figure 6-9: (x,y) co-ordinate in CIE 1931 diagram for inspected light
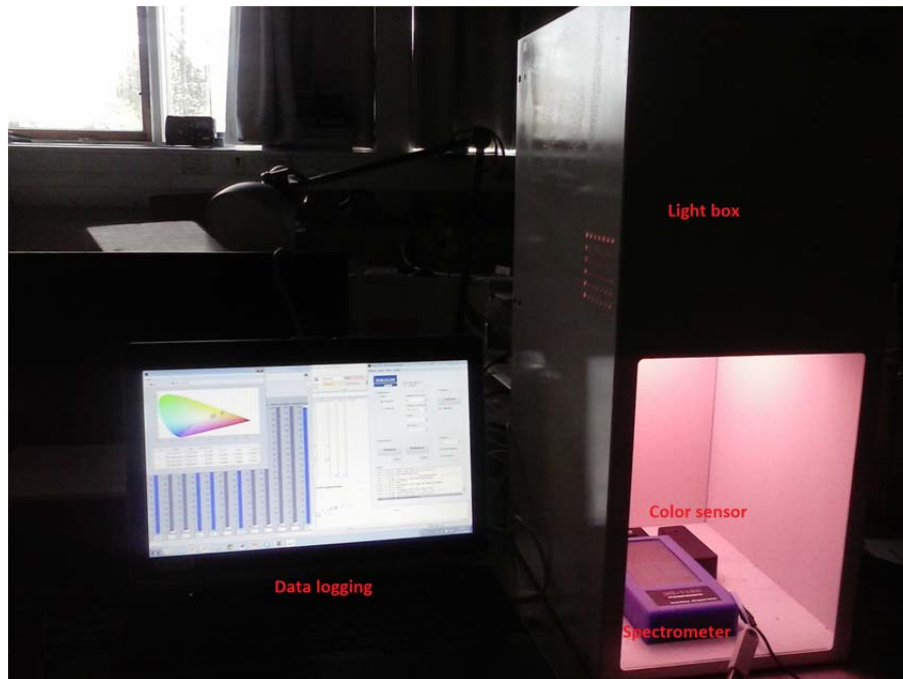

Figure 6-10: Experimental setup for the calibration of color sensor

To find out the calibration matrix for the color sensor the following equations (53)-(57) need to be abided. Let us assume that X_s, Y_s, and Z_s are the tristimulus values measured by the spectrometer for measured light which can be related to the tristimulus values (X_J, Y_J, and Z_J) measured by the color sensor after multiplying by the calibration matrix A (assumed linear relation) as seen in equation (53), where the coefficient of the calibration matrix is defined in equation (54).

$$\begin{bmatrix} X_s \\ Y_s \\ Z_s \end{bmatrix} = A * \begin{bmatrix} X_J \\ Y_J \\ Z_J \end{bmatrix} \tag{53}$$

$$where, A = \begin{bmatrix} a_{11} & a_{12} & a_{13} \\ a_{21} & a_{22} & a_{23} \\ a_{31} & a_{32} & a_{33} \end{bmatrix} \tag{54}$$

Now to do the calibration, we have to find out the coefficient of the calibration matrix. Three calibration points are chosen from the 32 sets of light measurements and corresponding tristimulus values are noted from the spectrometer as well as from the color sensor. In equation (55) S and J represent the three sets of tristimulus values from the spectrometer as well from the color sensor, respectively, whereas A is the same for each case. Therefore, A can be evaluated by the equation (56). Finally the test vector T can be determined by using equation (57), while T represents the tristimulus values for any light measured by the color sensor.

$$Now \begin{bmatrix} X_{s1} & X_{s2} & X_{s3} \\ Y_{s1} & Y_{s2} & Y_{s3} \\ Z_{s1} & Z_{s2} & Z_{s3} \end{bmatrix} = A * \begin{bmatrix} X_{J1} & X_{J2} & X_{J3} \\ Y_{J1} & Y_{J2} & Y_{J3} \\ Z_{J1} & Z_{J2} & Z_{J3} \end{bmatrix} \tag{55}$$

$$where, S = \begin{bmatrix} X_{s1} & X_{s2} & X_{s3} \\ Y_{s1} & Y_{s2} & Y_{s3} \\ Z_{s1} & Z_{s2} & Z_{s3} \end{bmatrix} and J =$$

$$\begin{bmatrix} X_{J1} & X_{J2} & X_{J3} \\ Y_{J1} & Y_{J2} & Y_{J3} \\ Z_{J1} & Z_{J2} & Z_{J3} \end{bmatrix}$$

$$\therefore A = S * J^{-1} \tag{56}$$

$$\therefore T = \begin{bmatrix} X \\ Y \\ Z \end{bmatrix} = (S * J^{-1}) * \begin{bmatrix} X_{J4} \\ Y_{J4} \\ Z_{J4} \end{bmatrix} = A * \begin{bmatrix} X_{J4} \\ Y_{J4} \\ Z_{J4} \end{bmatrix} \tag{57}$$

Since the control mechanism evaluates the color characteristics according to CIE 1976, after calibrating the color senor reading, the measured lights are validated and plotted in the CIE 1976 diagram (Figure 6-11). In the Figure 6-11 (a)-(c), '◊' represents the three calibrating points to create the calibration matrix while characterizing any white light. By using that calibration matrix, the color sensor readings are calibrated, (u′,v′) coordinates are evaluated and plotted in the CIE 1976 diagram along with the reading for the same measured lights from the spectrometer. As seen in the Figure 6-11 (b)-(c), with the three calibrating points, the measured white light from the spectrometer as well as the color sensor are in good agreement with each other (average variation ~2.7x10^{-6}) and they are within the just noticeable difference (JND) circle[46]. However, for the characterization of monochromatic light, these calibration points are not good (Figure 6-11 (a)) as the spectrometric and color sensor are not in good agreement. Therefore, it is required to find another three calibration points for the monochromatic light to avoid the error due to a spectral mismatch. There is ~6% measurement discrepancy between the spectrometer and the color sensor (as seen in Figure 6-11 (d)) by using the three calibration points indicated in Figure 6-11 (a)-(c). Appendix D will describe the method if 32 measurement points have been taken to evaluate the same calibration matrix.
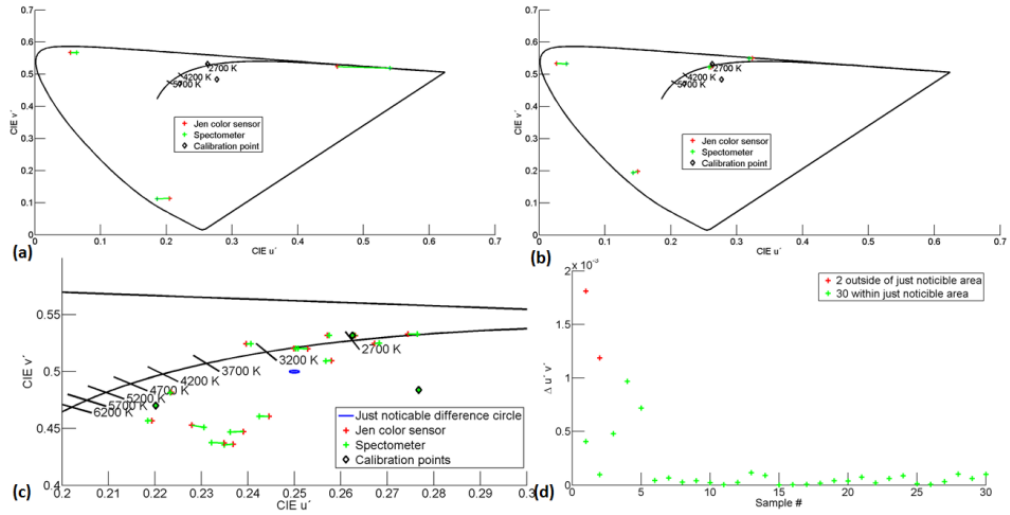

Figure 6-11: (u′,v′) co-ordinate in the CIE 1976 diagram after measuring the spectrometer and the color sensor (a) monochromatic light (b) mixed light (c), and white light; (d) characterizing the points according to JND definition [46]

6.5.2 Color sensor dynamic gain settings

The color sensor gain settings are a critical aspect for the measurement of tristimulus values as each setting corresponds to a particular calibration matrix. Therefore the gain settings of the color sensor have influence on the measurement during the operational time. There are two ways of changing the gain settings of the color sensor, which ultimately change the reading of ADC count (X, Y, and Z). Table 6-2 represents the available reference current and the integration time settings for the color sensor which are responsible for the gain settings. For a certain reference current, ADC count (X, Y and Z) increases if the integration time increases. However, the ADC count (X, Y and Z) decreases if the reference current increases at integration time. The maximum and minimum ADC count for the settings is 65536 and 0. The operating range of the ADC count between 65000 and 30 are good, as count s <30 and > 65000 have the probability of detecting the error in the measurement. Figure 6-12 represents the ADC counts (X, Y, and Z) for different gain settings.

Table 6-2: Gain settings for the color sensor

Reference current [nA]	Integration time [ms]
20	64
80	128
320	256
1280	512
5120	1024

In the figure, the y axis represents the ADC count while the x axis represents the logarithmic scale of the reference current. The line with a solid square represents the X ADC count, the dash-dotted line with a solid circle represents the Y ADC count and the dashed line with a solid triangle represents the Z ADC count. The different color in the legend represents the different set of X, Y and Z ADC counts for different integration time. For an example, the black color represents the ADC X, Y and Z counts for the integration time = 64 ms.
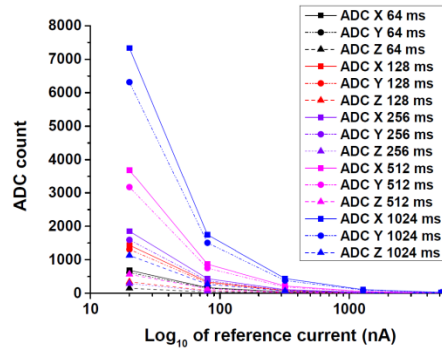

Figure 6-12: For different sets of integration time, the ADC X,Y and Z counts variation on reference current for the color sensor

As seen in the figure, irrespective of any settings, the Z ADC count is always lower than the X and Y ADC count. Since the ADC count depends on the light intensity incident

on the color sensor, it is critical to set the gain-settings at the optimum condition so that the ADC count cannot reach saturation or cannot count <30. To facilitate the dynamic gain settings according to the light intensity incident on the color sensor, software codes are written in MATLAB and incorporated into the control unit of V8 light engine. The thorough investigation has been done on the ADC count depending on the light intensity. Therefore there will be a default settings (reference current: 80 nA and integration time: 128 ms) for when the measurement will start. The corresponding calibration matrix will be taken during the calculation of tristimulus values of light (equation (57)). If the light intensity is high enough to reach the saturation in the ADC count, the control unit changes to a higher reference current or lower the integration time according to the situation and the action will be vice versa for the low lighting. However, for each case, the calibration matrix will be different. The standard deviation for the maximum error occurs due to different settings is ~0.0004.

6.6 Microlens array characterization

The surface quality looking at pre and after coating process results of the fabricated lenslets are measured and analyzed by 3D confocal and interferometric microscopy (Sensofar Plu-neox). Confocal microscopy (Figure 6-13(a)) is used in this application because it offers several advantages over conventional optical microscopy, which includes shallow depth of field, elimination of out-of-focus glare, and the ability to collect serial optical sections from thick specimens. Therefore confocal microscopy is an optical imaging technique for increasing optical resolution and contrast of a micro-graph by introducing a spatial pinhole placed at the confocal plane of the lens to eliminate out-of-focus light. By this way, within a thick object, it enables the reconstruction of 3D structures from the acquired images by accumulating sets of images at different depths.

The white light interferometric microscope system (Figure 6-13(b)) exploits a method known as two-beam interferometry to measure surface profiles. Two beams of light interfere with each other as the term "two-beam interference" suggests. The light from the light source divides in two when it hits a half mirror. One part reflects off the mirror and the other transmits through it. The reflected light then travels to the reference mirror, while the light that transmits through travels to the material under observation on the stage. However, both beams of light bounces off the respective mentioned objects. The beams interfere with each other to form an image in the camera, where they produce striped patterns known as interference fringes. This microscopic measurement is used to get bright contrast between the interference fringes which helps to measure accurately the height of the optical component.
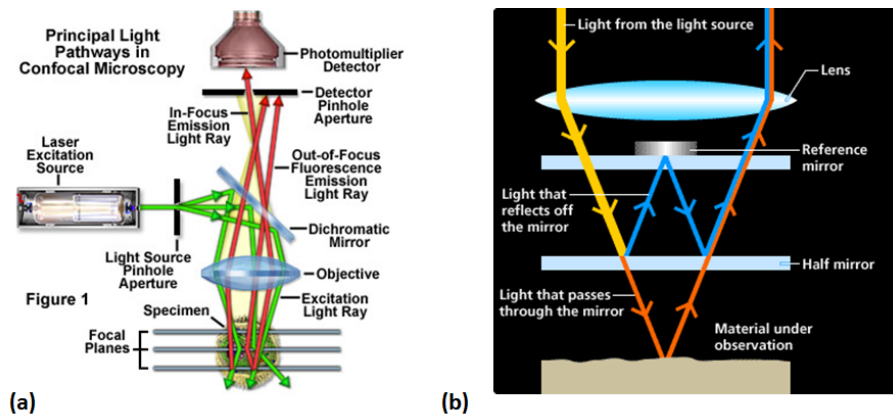
Figure 6-13: Basic principle of (a) Confocal microscopy (Ref.:[146]); (b) Interferometric microscopy (Ref.:[147])

The analytical results for surface quality and the quantitative measurement on lens parameters are shown in the 6.6.1 section. The optical performance with regard to the application was investigated by measuring the angular dependence of the transmission and investigating the light scattering effect. Figure 6-14 illustrates the setup for simulating the transmitted light as a function of incident cone and different exit cones. It also describes the transmission measurement, where a collimated white light beam with a beam diameter of 10 mm from a fiber coupled source (Ocean Optics HL 2000) was used. The incidence angle was varied over the interval ±45°. The transmitted light was measured as a function of incidence angle using a 6 inch integrating sphere as collection optics. The MA was mounted at the 1 inch diameter port opening and the exit cone half angle is nearly 90°, which corresponds to the top part of the simulation results shown in Figure 3-16. The results from the measurement are shown in Figure 6-17. The transmitted light was measured using a spectrometer (QE 65000) fiber coupled to the sphere. Further, the light scattering from the surface of the MA is investigated by looking at the reflected laser light of a single lenslet and discussed in the 6.6.2 section.
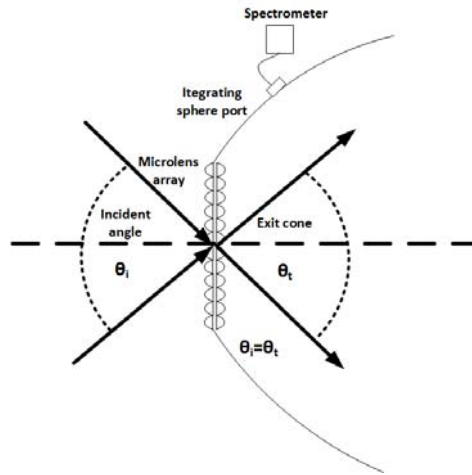
Figure 6-14: Sketch illustrating the simulation and experimental set-up for measuring angular transmission and acceptance angle of the MA where dashed line represents the optical axis (Ref. Figure 6 of Chakrabarti et. al [13])

6.6.1 Surface topology

The properties of the injection molded samples from the uncoated and the coated mold tool is compared. The confocal microscopy measurement was done using the objective of Nikon 50x with NA 0.95. The 3D images have been taken for 5 consecutive lenslets by the method of stitching 3x3 images with the condition of 25% overlap. From each of the two microlens arrays 5 individual lenses have been analyzed. The diameter of the lens array including the outer ring is 85 mm as shown in Figure 6-15(a). The position of the central lens was 39 mm from the edge of the perimeter of the outer ring and the five consecutive lenslets were taken for the measurements from that region. The diameter of the hexagonal lenses is measured at an edge to edge distance which is measured by Fourier transform of the image (20x microscope images) to identify a unit cell or lenslet. Thus, the whole image is used for the measurement (seen in Figure 6-15 (b)). The total height of the lens is measured from the stitched image (1x8 50x) as seen in Figure 6-15 (c) where the center and the edge of the single lenslet is visible. The vertical distance from the edge to the center of the lenslet gives the height. The radius of curvature is measured for each lens by fitting a sphere to the 3D surface. The aberration from this sphere is also investigated as a 3D image. The roughness of the surface is also measured after suitable waviness filtration. Table 6-3 summarizes the measured results for the lens parameters. The standard deviation between all measurements for the radius of curvature is 35µm. The table shows the repeatability and reproducibility of the fabrication process within ± 50 µm accuracy. The values corresponding to uncoated and coated mold are equal within the uncertainties and shows that the coating process does not affect the lenslet parameters.
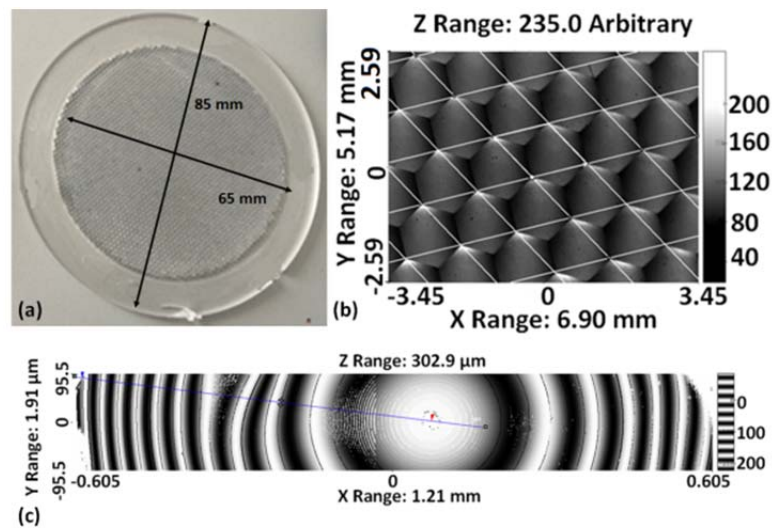
Figure 6-15: (a) Photo of the injection molded sample; (b) Magnified view of the selected portion of the five lenslets for measuring the lens width; (c) Magnified single lenslet for height measurement (Ref. Figure 7 of Chakrabarti et. al [13])

Table 6-3 : Measure Single Lens Parameters by 3D Microscopy (Ref. Table 2 of Chakrabarti et. al [13])

Microlens array type	Radius of curvature for lenslet [mm]	Sag [mm]	lenslet width [mm]
Uncoated	0.863 ±0.040	0.503± 0.001	1.457± 0.005
Coated	0.869 ±0.035	0.492 ± 0.001	1.46 ± 0.005

The surface quality of the lenslet has been investigated through surface topography measurements. Figure 6-16 compares the images of the top surfaces of lenslet from the uncoated (left) and coated (right) mold, after fitting with a sphere of radius 846.1 μm. The surface roughness is calculated by measuring R_a, R_q, and R_z [148] which are shown in Figure 6-16. There is some cast defect occurrence at the edge of the perimeter of the array. However, those defects did not influence the light path. It is observed that the photoresist coating of the mold improves the surface roughness of the injection molded microlens arrays, in reducing the R_a, R_q, and R_z by factors of 2, 2.5, and 2.6. It is seen from the cross-sections (Figure 6-16(c) and (d)) that the maximum variation is reduced from 1.2 μm to 0.2 μm for these specific scans.

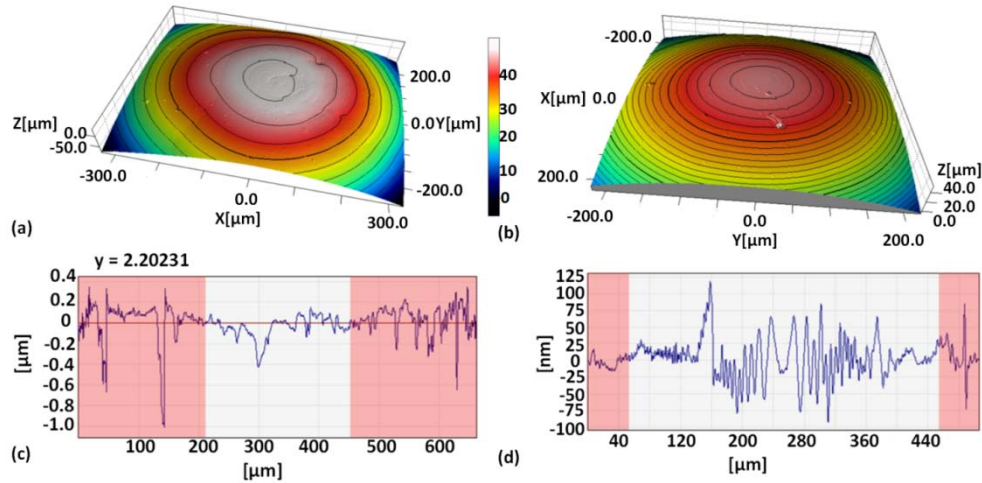**Figure 6-16: Topography image with height contours for each 2 μm in the z-direction for microlens lenslet from (a) (shown 600 x 600 μm² area) uncoated and (b) (shown 400 x 400 μm² area) coated mold and corresponding surface variation along cross section in (c) and (d) (Ref. Figure 8 of Chakrabarti et. al [13])**

Table 6-4: Roughness Measurement According to ISO 4287:1997 [148]

MA type	R_a^{*a} [nm]	R_q^{*b} [nm]	R_z^{*c} [nm]
Uncoated	75±29	110±56	441±194
coated	38±1	42±2	173±26

$^{*a}R_a$: arithmetic average of absolute value for surface roughness; $^{*b}R_q$: root mean square (rms) average of the roughness profile ordinates; $^{*c}R_z$: the mean roughness depth which is the arithmetic mean value of the single roughness depths of consecutive sampling lengths

6.6.2 Working performance of MA

The working performance of the injection molded MA from the coated mold has been investigated through measurement of the angular transmission, Figure 6-17 shows the measured transmission as a function of the incidence angle and the corresponding simulation is shown as well. This is used to determine the acceptance angle of the MA. Figure 6-17 shows the corresponding results for another MA with D = 1.2 mm used in the first prototype of the LED light engine. The acceptance angle for this is 37°. For the optimized design of the MA produced in this work, the numerical aperture (NA) has been increased by increasing the width D to a value of 1.45 mm. The measurement for this in Figure 6-17, shows a maximum transmission of ~ 92% which is almost constant within ±40°, hence an acceptance angle of 40°. The refractive index of PMMA is 1.489. Thus, the Fresnel reflection loss per interface for 2.1 mm MA is ~3.9 % and transmission from the array was ~ 92%. Again, the calculated acceptance angle according to equation (35) is ~ 41°. Hence, there is a good correspondence between simulation and measurements on the produced MA. Due to machine accuracy in lens parameters; there is a discrepancy of ~2° in acceptance angle between the simulation

and the experiment. The increasing measured and simulated efficiency at angle larger than ±40° corresponds to the coupling of light through the neighbor lenslets, illustrated in Figure 3-15 (b).
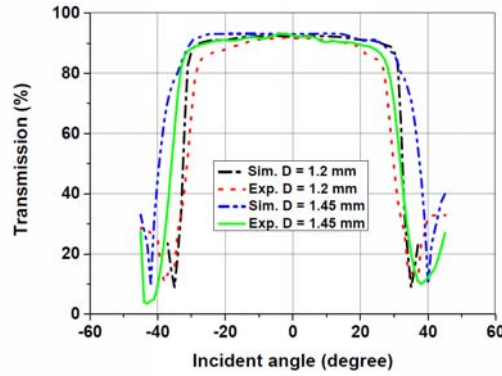
Figure 6-17: Comparison of MA by both simulation (Sim.) and experiment (Exp.) (Ref. Figure 9 of Chakrabarti et. al [13])

Figure 6-18 shows the results of the visual and light scattering investigation of the surface quality. The investigation is on a single lenslet, where the images to the left shows photos of the top surface taken by optical microscope and the images on the right are photos of the reflected light when a lenslet is illuminated by a He-Ne laser beam. The images in Figure 6-18 (a) are for the injection molded MA from the uncoated mold. Irregularities are seen on the microscope image and the reflected He-Ne laser beam is strongly distorted and scattered. This surface quality is not good enough to consider for the microlens application. The MA produced from the photoresist coated mold, has a much improved surface quality as shown in Figure 6-18 (b), there are much fewer irregularities in the microscope image and the transmitted He-Ne laser beam is nearly undistorted and less scattered light has been observed. This surface quality is applicable for the LED light engine application and a 5% increase of the efficiency of this was observed when using the MA produced from the coated mold compared to the one from the uncoated mold.

Figure 6-18: Optical microscopic images of a single lenslet (left side) and photo of transmitted He-Ne laser beam from a single lenslet (right side) in injection molded MA from the (a) uncoated mold and (b) photoresist coated mold (Ref. Figure 10 of Chakrabarti et. al [13])

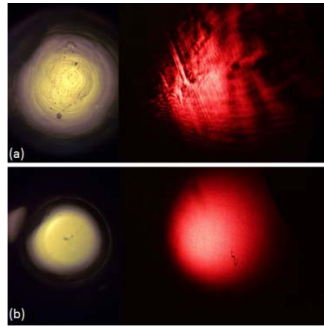## 6.7 Measurement of the prototype

Figure 6-19 shows the prototype of the V8 light engine in operation. This section will characterize the beam properties of the light engine such as LID, total luminous flux, CRI scores, beam homogeneity, light output stability in terms of operational time as well as temperature, etc. for the prototype.
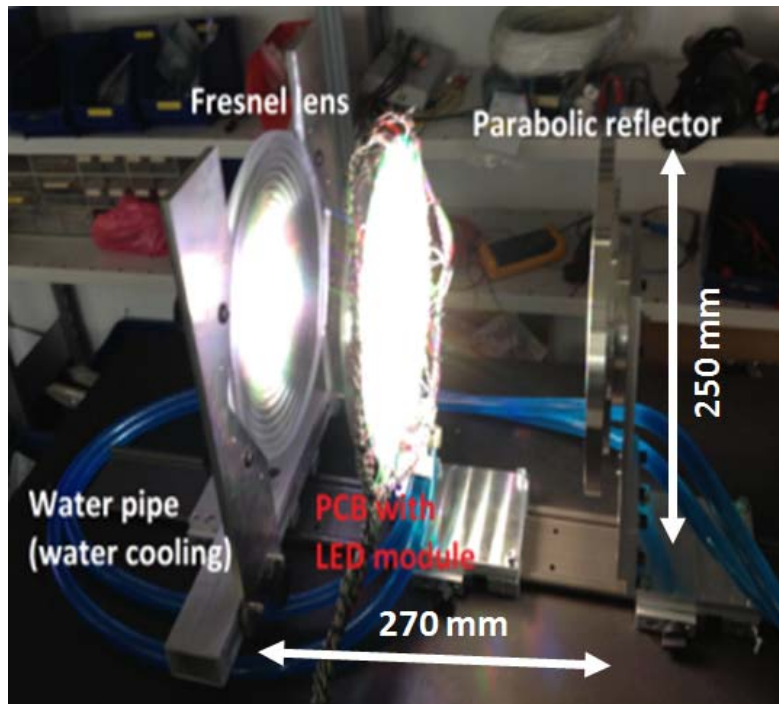
Figure 6-19: White light output is coming out from the prototype of V8 light engine

6.7.1 Forward flux and LID measurement from the prototype

Initially the luminous flux from each of the colored LEDs are measured from the prototype by forward flux measurement using 1 m IS according to the CIE standard [40]. Figure 6-20 represents the total luminous flux obtained from the corresponding DMX values for the individual color LEDs inside the prototype. As seen in the figure, except for the red LEDs; all other LEDs achieving saturation in the luminous flux after reaching a DMX value of 90%. This is because, at a 90% DMX level, the current level for all colored LEDs (except the red LED) reach saturation point at $\sim$ 984 mA (Figure 6-21). Therefore, during the operational time of the V8 light engine, it is safer to use the maximum 90% of DMX for all LEDs. It is also noticed in Figure 6-21 that the relation between the current and DMX are not same for the red LED as other colored LEDs. Therefore, the uncertainty of the luminous flux for the variation of DMX values is considered in the Monte Carlo simulation in section of 5.2 in Chapter 5.

Figure 6-20: Increased luminous flux with increasing DMX for all; (a) the royal blue, (b) the blue, (c) the green, (d) the red, (e) the white LED with reflector loss at 30%
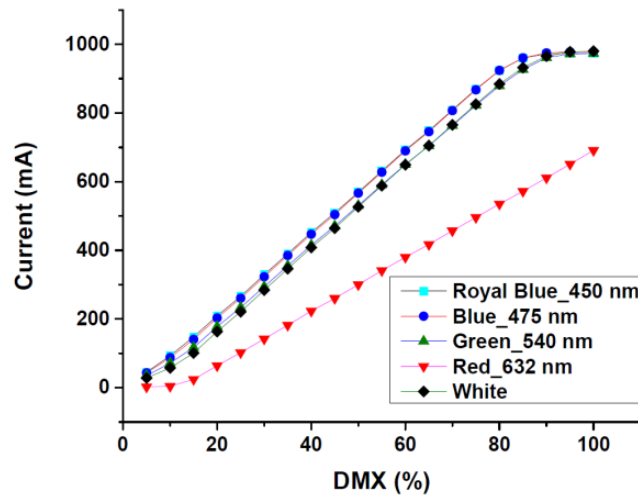
Figure 6-21: Change in current with a changing DMX for the individual colored LEDs

Table 6-5 compares the measurement of luminous flux at 100% DMX from the individual colored LEDs transmitted from the TIR lens using 2 m IS with the measurement of luminous flux at 100% DMX from the individual colored LEDs from the prototype using 1 m IS. Total loss inside the prototype is 20316 lm. However, the l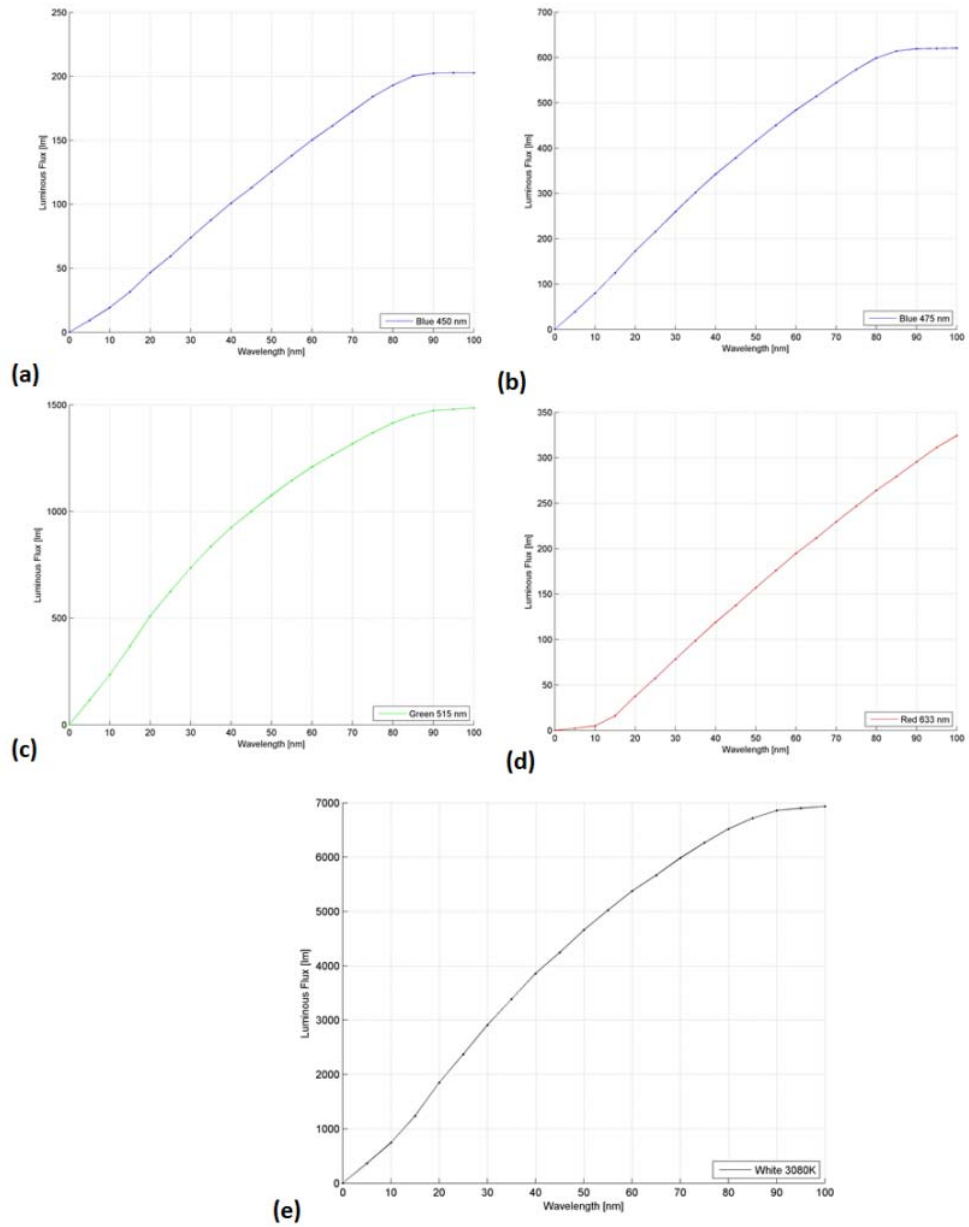oss was decreased to 18153 lm when the reflector was modified. The optical efficiency of the prototype was ~42%. The position of the LEDs, with respect to the gate, influences the loss in the prototype, which is discussed in section 3.3 in Chapter 3. The print size of the royal blue and the blue LED are small. Therefore the loss from the TIR lens is less for those LEDs compared to others.

Table 6-5: Total luminous flux for the individual color LEDs from the prototype

LEDs	LED numbers	Luminous flux (lm) @ individual color LEDs + TIR lens at 100% DMX	Luminous flux (lm) @ individual color LEDs at 100% DMX for prototype	Loss (%) for individual color LEDs
Royal blue	18	466	238	51
Blue	24	1396	688	49
Red	12	1224	352	29
Green	30	5597	1675	30
White	126	22960	8375	36
Total	210	31643	11327	39

The prototype was not able to produce the required luminous flux (~20,000 lm) from the V8 light engine. Therefore, the optimization of the V8 light engine design was needed and the optimization steps are elaborated on in Chapter 3, section 3.3. The luminous flux values can be increased after optimization of MA and TIR lens which are shown in Table 6-6. The increase in number of LEDs from 210 to 288 also increases the final light output by 56.5% compared to the prototype. However, the overall size and

weight would increase accordingly by 25% and 27%, respectively. In addition to this the mechanical design difficulty increases since making such a large reflector is complicated and costly.

Table 6-6: Improvement in luminous flux after optimization in simulation

Luminous flux (lm) (Prototype)	Luminous flux (lm) (after MA Optimization)	Luminous flux (lm) (after TIR lens size Optimization)	Luminous flux (lm) (288 LEDs)
11327	16624	22284	25990
Improvement	5297	5660	3706

Due to time restrictions as well as the budgetary limitation, the second prototype was not made after the design optimization. Figure 6-22 shows the experimental validation with respect to the simulation where the optical efficiency of the white LED transmitted through the TIR lens is characterized inside the optical system at different ring positions. The average deviation in optical efficiency of the light engine between the simulation and experimental results is ~9.7%, whereas the measurement uncertainty for the experiment is ~6%.
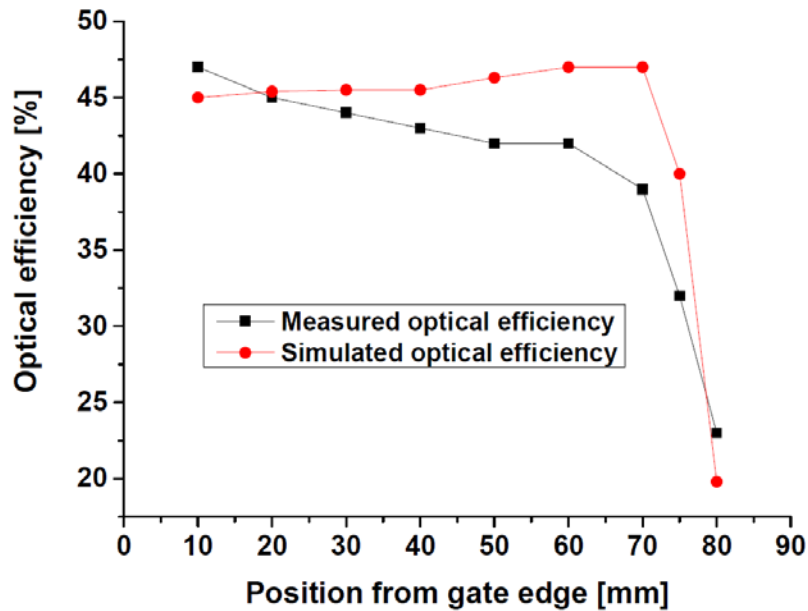
Figure 6-22: The comparison between simulation and experimental results considering the optical efficiency of white LED through the TIR lens at each ring position

The angular distribution of the luminous intensity of the prototype was measured using goniospectrometers; a horizontal c–type manually controlled goniospectrometer, which is equipped with an optical probe with diffuser (EOP-146) for the irradiance

measurement. The detector was fixed in space and the LED system was rotating with a specific angle. The measurement distances was 8.65 m and the diameter of the luminous area, i.e. the hemisphere of the optical system, was D = 125 mm. The measurement distances was 68xD and thus, the measurement was done in the far field [40]. For the 100% DMX setting, the measurements were done for the flood and spot position of the V8 light engine. The experimental results are plotted in polar graph (Figure 6-23).
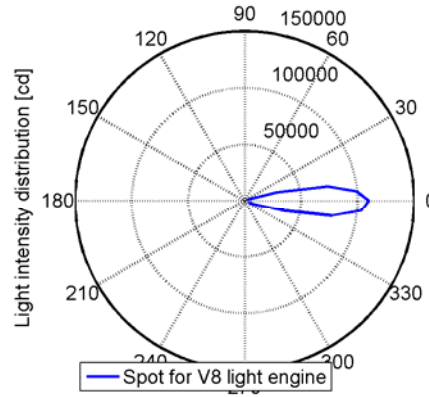
(a)
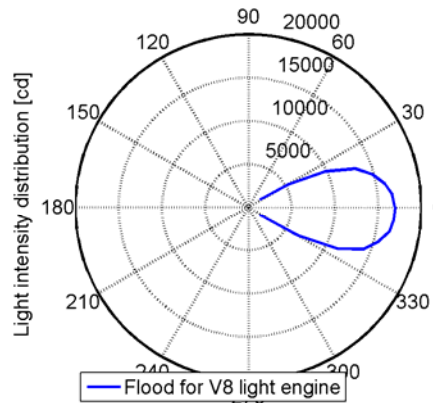
(b)

Figure 6-23: The LID for (a) spot; (b) flood position of the V8 light engine

6.7.2 Beam homogeneity

Figure 6-24(a) represents the experimental results for light intensity at flood position from the prototype measured by PRC photometer, while the projected light distance was 5 m and the manually controlled gonio-spectrometer respectively. Both the measurement shows the FWHM of the beam size is ~60° and the uniform intensity is

found within ±20° (Figure 6-24 (a)). There is 25% variation in intensity within the entire beam size (FWHM) in the PRC measurement. The data point for the measurement by gonio-spectrometer was less and thus the intensity variation was not observed. The handheld spectrometer is used to investigate the beam homogeneity in CCT and CRI (Figure 6-24 (b)), and also in u´, v´ parameters (Figure 6-24 (c)). The measurement shows the uniformity in CCT, CRI, u´, and v´ are within ±25°. Due to the measurement uncertainty of low light level, the both end of the graphs in Figure 6-24 (b) and Figure 6-24 (c) show the large variations.
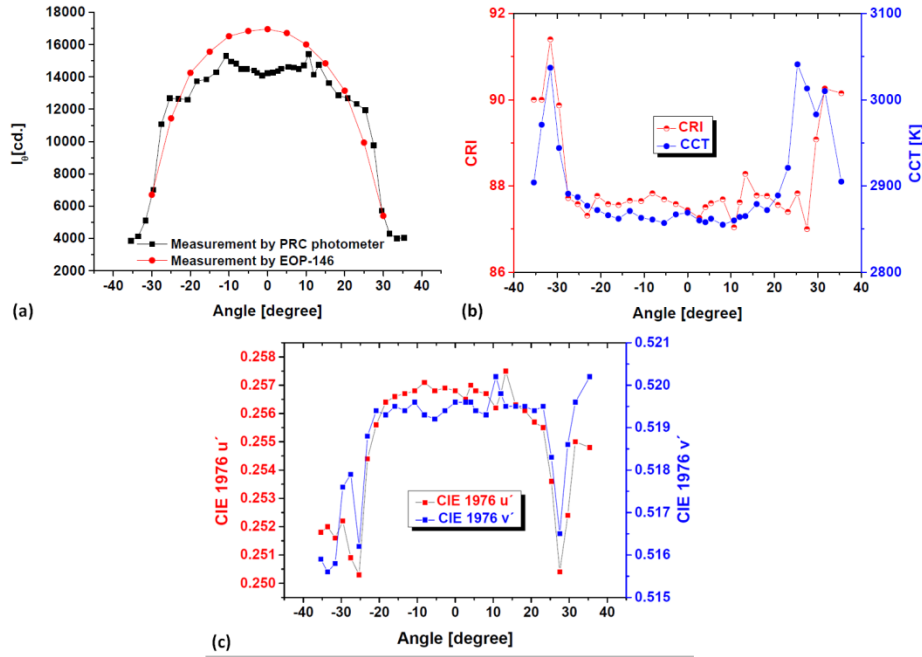
Figure 6-24: (a) Distribution of light intensity with respect to beam size (b) Distribution of CRI and CCT with respect to beam size (c) CIE 1976 (u´, v´) with respect to beam angle (Ref. figure 8 of Chakrabarti et. al [14])

The spot position for the V8 light engine is found by placing the light engine at the focal plane of the Fresnel lens. To obtain flood position, the Fresnel lens is positioned as close as possible to the MA. The picture is taken by projecting the light on a white piece of cardboard for the spot and for the flood position to check the visual appearance (Figure 6-25). It looks uniform to the naked eye. However, the shape of the spot is hexagonal due to the hexagonal MA, which is already seen by the simulation (Figure 3-23). The outlook section 7.2.1 in Chapter 7 will discuss this issue further.
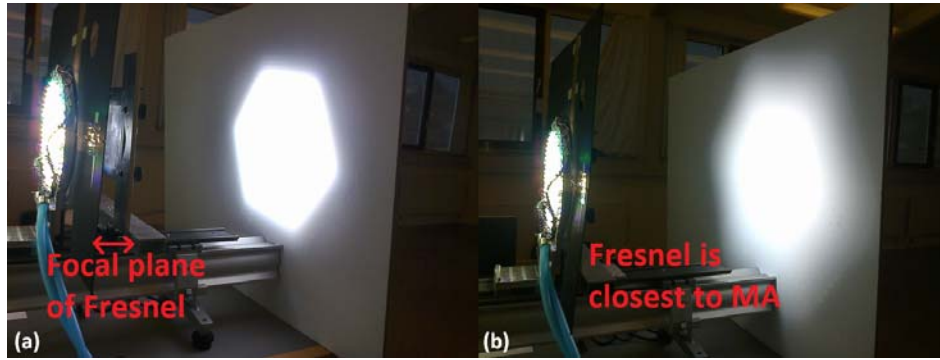
Figure 6-25: (a) the spot; (b) the flood from the V8 light engine

Instead of using the MA in the V8 light engine, the color mixing from the diffuser (Gaussian laser beam shaper LBH(DG)-GT-DV84° at 633 nm from aμs) was also experimented on by using the same setup as mentioned in Figure 6-14. The diffuser is in form of the 2D – refractive micro-optic array for transforming the beam intensity distribution into the Gaussian beam. The beam divergence of the diffuser was 84°. Although, the output from the V8 light engine after using the diffuser did not show the hexagonal spot at the screen, luminous flux was less compared to the MA. Figure 6-26 represents the transmission comparison between the MA and the diffuser. In case of the diffuser, the transmission decreases gradually from the peak transmission value which is not desirable for the beam homogeneity.
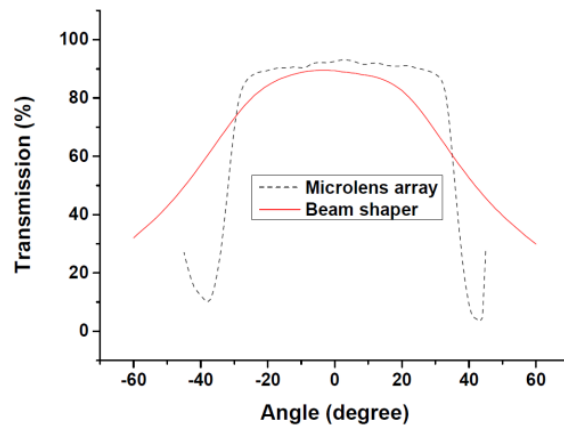
Figure 6-26: Light transmission comparison between the MA and the beam shaper (diffuser)

6.7.3 CRI & CQS score

As mentioned earlier, the CRI matrices scores are high for the V8 light engine; Figure 6-27 represents the metric scores for four CCT positions. It is seen in the figure that CRI (R_a) as well as CQS are > 85 for each CCT values and the lowest CRI (R_9) is 41 at 3000 K. CRI (R_{10}) is also ~80 for each CCT. According to the application, the measured metric

scores at each CCT have good values. The good value of CRI(R_9) renders the strong red contents whilst CRI(R_{10}) is good for rendering yellow objects[120], [149]–[154].
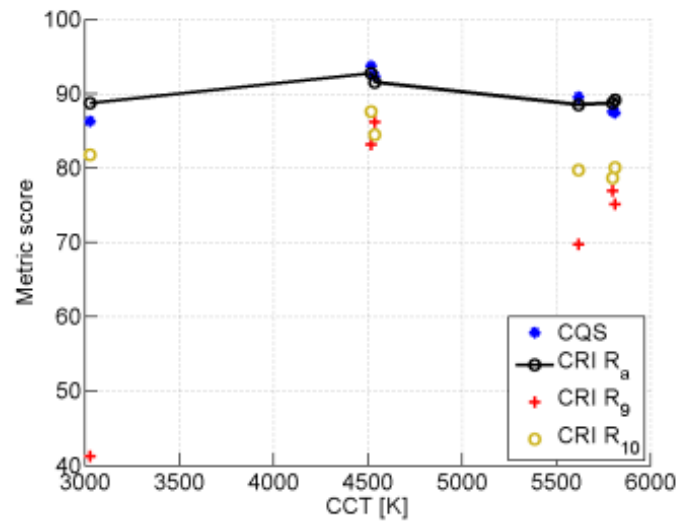
Figure 6-27: Metric score for four tuned CCT positions (3000 K, 4500 K, 4600 K and 4800 K)

6.7.4 Warmup time

The temperature dependency of the prototype was investigated during the warmup time (Figure 6-28). The prototype was stable for 25 minutes after switching on the driver control unit. From the figure it is observed that the luminous flux was decreased by ~1.5% for increasing of the temperature by 9%.
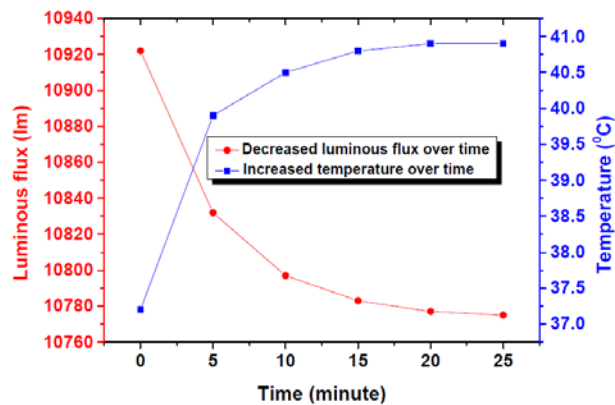
Figure 6-28: The temperature dependency of the luminous flux during warmup time

6.7.5 Temperature sensitivity

The color characteristics stability (e.g CCT, D_{uv}, CRI(R_a), and CRI(R_9)) with varying temperature from 61 ℃ to 35 ℃ was examined when all LEDs inside the prototype were set at 100% DMX (Figure 6-29). Temperature sensitivities for CCT, D_{uv} are calculated from this measurement which is used as uncertainties in the Monte Carlo simulation in section 5.2 in Chapter 5.
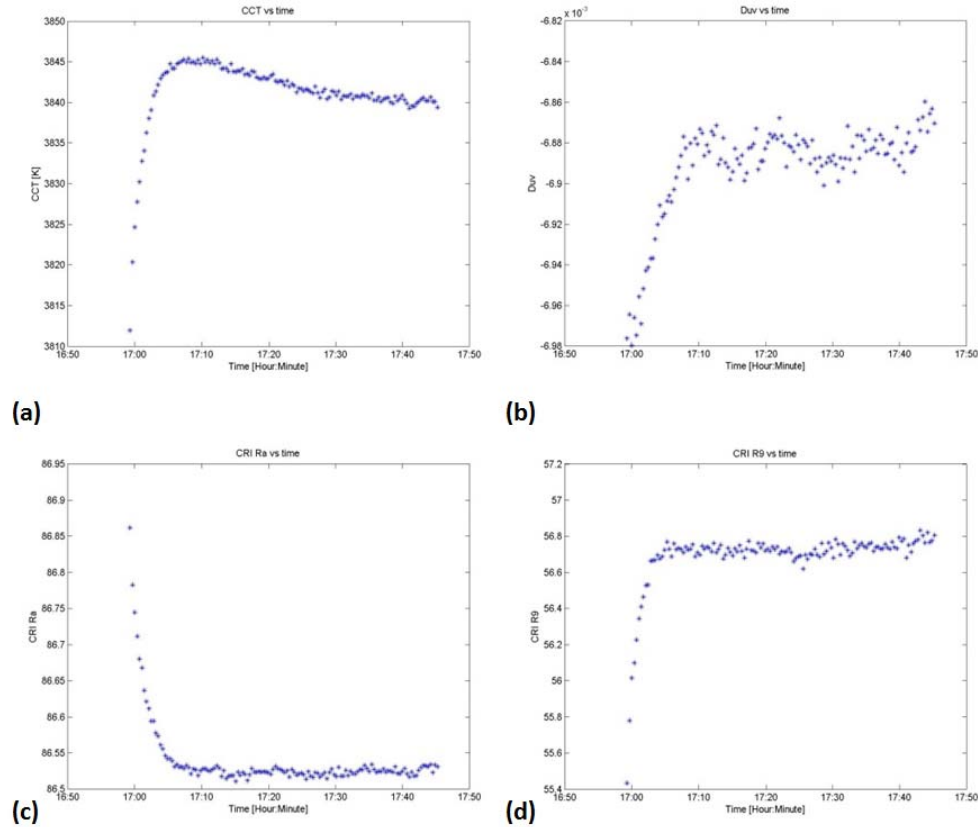
Figure 6-29: Variation of color characteristics with varying temperature

6.7.6 Flickering test

There was no temporal periodic intensity variation observed during the intensity dimming of the color channel in the V8 light engine. The experimental analysis has been done by feeding the measured signal from the detector to an oscilloscope (Scopein@Box).

6.7.7 Comparison with the traditional lighting

The measured light output from the Halogen-Fresnel traditional lamp (2 kW) is compared with the light output from the prototype of the V8 light engine (0.6 kW). Table 6-7 shows the comparison between the two lighting systems. Although the Halogen-Fresnel lamp is producing ~34% more luminous flux compared to the V8 light engine, it consumes 70% more electrical energy. Due to having a wider beam, the V8 light engine has less intensity than the other. However, after implementing the design modification, the final product of the V8 light engine with a low electrical consumption (~ 0.9 kW) will provide ~20,000 lm which is comparable to the light output from the Halogen-Fresnel. Moreover, the transition from flood to spot in the case of the Halogen–Fresnel lamp lose ~37% optical efficiency, whereas the loss in optical efficiency is ~10% for the V8 light engine. Figure 6-30 shows the comparison of normalized light intensity distribution (LID) between the Halogen-Fresnel lamp and the V8 light engine. As seen in Figure 6-30(a), the distributions of the Halogen-Fresnel lamp and the V8 light engine are similar for the flood position. However, for the spot position, the V8 light engine provides a broader light output (~±3°) than the Halogen-Fresnel lamp.

Table 6-7: Measured total ΦV, luminous efficacy, intensity and beam angle for the 2kW Halogen-Fresnel spotlight and the V8 prototype light engine; and corresponding values for the optimized simulated V8 light engine (Ref. Table 4 of Chakrabarti et. al [14])

Lighting system	Fresnel lens adjustment	Φ_V [lm]	Luminous efficacy [lm/W]	Intensity [cd]	FWHM @ 50% [degree]	Field angle [degree]
Halogen-Fresnel spotlight	Flood	18745	10	33902	50.6	69
V8 prototype	Flood	12350	19	15680	55	70.8
V8 simulated	Flood	22284	33	28292	-	-
Halogen-Fresnel spotlight	Spot	11777	7	237273	10.8	24
V8 prototype	Spot	11100	17	115494	16.2	29.2
V8 simulated	Spot	20060	30	208721	-	-
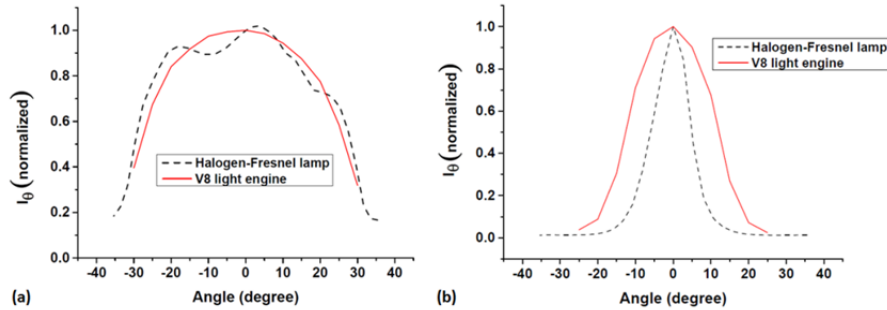
Figure 6-30: LID comparison between the Halogen-Fresnel lamp and the V8 light engine for (a) the flood; (b) the spot position, respectively

6.8 Summary

The experimental investigation results in the light output from the prototype are analyzed and discussed thoroughly within this chapter. The optical efficiency of the prototype was ~39%. The optical efficiency was enhanced after the optimization of the optical components of the V8 light engine. However, the final simulated optical efficiency from the V8 light engine is ~56%, whereas the average deviation between the simulation and the measured value is ~9.7%. The results indicate that the beam is uniform in intensity as well as in color. The CRI (R_a) is found > 85 and CRI (R_9) >40 for warm, neutral, and cool white. The comparison between the V8 light engine and the Halogen-Fresnel lamp shows that the V8 light engine loses 10% optical efficiency by changing the position from spot to flood, whereas the Halogen-Fresnel loses 37% of optical efficiency for the same. The LIDs for the flood position are similar for the Halogen-Fresnel lamp and the V8 light engine. However, the V8 light engine has a broader spectrum than the Halogen-Fresnel lamp.

Conclusion and outlook

Chapter 7 : Conclusions and outlook

7.1 Conclusions

The goal of the thesis is to describe a novel optical design and control of multi-colored LED lighting system for stage lighting applications which was carried out within three years (2013 – 2015) at the premises of DTU Fotonik, department of Photonics Engineering in collaboration with the Danish company Brother, Brother & Sons Aps, funded by The Danish National Advanced Technology Foundation in 2012.

The objectives of the project were to design, develop, and experimentally examine an optical system that produces collimated tunable white light from the combination of multi-colored LEDs cluster into a single energy efficient focusable beam. The intelligent color control of the individual LEDs inside the optical system would be able to provide a good quality of light output from the optical system such as: high luminous flux, high color rendering, and light uniformity in intensity as well as in correlated color temperature (CCT). The color variation as well as the light intensity variation from the lighting system needs to be within a just noticeable difference (JND) circle so that the probability of 50% of the human visual perception does not notice the color variations of the light output from the system during the operational time. Therefore, the lighting system should be capable of replacing the Fresnel lens spotlight Halogen lamp (2kW) as well as the commercially available LED luminaire (~160W) which has applications in stage lighting, theater lighting, TV studio lighting, etc.

Being conscious of the aim of the project, Chapter 1 describes the state-of-the-art of the present LED lighting technology as well as the measuring technique of the LED lighting which is used during the project work. 0 elaborates on the state-of-the-art of the traditional stage lighting and provides the experimental results on the light output from the Halogen-Fresnel lamp and the commercially available LED luminaire.

From Chapter 3 onward the thesis reports on the simulated design of an optical system, called the V8 light engine, which can address the requirement of the project goal. The simulated design is subsequently demonstrated by making a prototype. Keeping in mind the goal of achieving ~20,000 lm of luminous flux, one LED cluster having 210 five-colored LEDs are used inside the optical design of the V8 light engine.

The quasi-collimated beam (maximum divergence ∼±8°) from the individual LEDs transmitted through the total internal reflection lens (TIR) is reflected by a parabolic reflector and is directed towards the optical window (gate), which is situated at the focal plane of the reflector. One hexagonal patterned double-sided convex microlens array (MA), called a Kohler integrator, is used at the gate position to combine a large number of quasi-collimated beams from the individual colored LEDs arriving at the MA at different angles into a homogenous color mixed beam. To provide a cost effective solution in making an MA, a new process for tool fabrication utilized for injection molding of the microlens structures is proposed. The process exploits the standard CNC milling process to make a first rough mold in steel. A surface treatment is introduced afterwards by spray coating with photoresist to obtain the optical surface quality required for the MA. The process overcomes the expensive and tedious manual polishing or direct diamond turning and provides an easy and inexpensive mold and hence an extraordinarily inexpensive injection molding replication process. The experimental investigation of the direct 3D printed MA indicates more loss compared to the MA made through the proposed procedure. The fabrication process is demonstrated by producing a double-sided MA with ø50 mm for the prototype of the V8 LED light engine. The working performance and the surface quality of the lens array are characterized experimentally.

To achieve the goal of high luminous flux (∼20,000 lm), the simulated optical design of the V8 light engine is optimized through the experimental investigation of the prototype which is discussed in Chapter 6. The modified simulated optical design indicates the possibility of receiving the luminous flux > 20,000 lm from the V8 light engine. The light transmission from the MA depends on the refractive index of the material as well as the lenslet parameter of the MA. The optimization on the lenslet parameters allows a high angle beam to transmit through the MA, and enhances the optical efficiency of the V8 light engine. Therefore, the critical design optimization of the MA helps to increase the acceptance angle of the MA from ±30° to ±40°, increasing the optical efficiency further. An extensive optical loss characterization was carried out for the optical components used inside the V8 light engine. Using a larger total internal reflection (TIR) lens and optimizing the parameter of the reflector, further enhancement of the optical efficiency is found. The final optical efficiency of the system is ∼56% which delivers the goal of having luminous flux >20,000 lm from the light engine. The modified design is not experimentally validated due to insufficient financial support. However, there is an agreement between the previous simulations and related experimental results with a maximum average variation of ∼9.7%.

To offer tunable white light and high color rendering, the additive color mixing technique of multi-colored LEDs is used which is explained in Chapter 4. Initially, the color mixing technique is investigated by simulating an example of a simple tri-color LED system. A white light complemented by cyan and deep red LEDs are used inside the simulation to achieve high color rendering at a low correlated color temperature. A spectral mapping of the possible combinations of tri-color LEDs is used to locate the optimal solutions within the color gamut, emphasizing chromaticity and the color rendering indices. This mapping is further exploited as a tool to simulate a complicated system like the V8 light engine where the color mixing is done by five colored LED clusters. A geometrical optical model of the tri-color LED system is used to design and optimize the light intensity distribution as a function of angle. The resultant design

produces a diffused homogeneous white light with a tuned low correlated color temperature (CCT). The experimental characterization of the tri-color optical system indicates that it is capable of replacing the incandescent lighting in museum lighting application. Using the tri-color system as a tool, the V8 light engine design uses four colored LEDs to supplement and change the spectral power distribution (SPD) from a warm white LED at 3000 K. The output from the individual LEDs is added to produce the resultant SPD, which provides dimmable white light output from the V8 light engine at a CCT ranging from 3000 K to 6000 K with a high color rendering. The measured light output from the first prototype shows good color rendering (CRI (R_a)> 85, CRI (R_9)>40) and light uniformity in intensity as well as in CCT. To deliver a collimated white light, a laser color mixing technique could be a potential candidate. However, it would be expensive to use more than 20 lasers in order to reach the aim of a luminous flux > 20,000 lm. Moreover, the color rendering of the resulting mixed light is not good compared to color mixing by LED. This is due to the narrow bandwidth of the laser. Therefore, unlike color mixing by LED, the color mixing by laser produces a resultant SPD which cannot have a broad spectrum. Therefore, the produced white light will be uncomfortable for viewing an object due to the narrow band width in laser emission.

Another stringent requirement for stage lighting is to have lighting stability during the operational time. Chapter 5 is about the color consistency of the V8 light engine. Since the light engine consists of several different colored LEDs, some instability in light intensity may occur as well as in color. LED binning (wavelength and flux) and aging, ambient temperature, LED junction temperature, driver electronic such as digital control of current, system run time, etc. are the influencing factors that provide uncertainty in the desired light output. The chapter describes the method of analysis for those influencing factors on the light engine by the Monte Carlo simulation. The known values of the influencing factors can help to control the uncertainty in the desired light output. In the chapter, a simulated color control system mechanism is proposed and explained, which incorporates a pre-calibrated lookup table as well as a calibrated color sensor to provide a feedback to the control system. The stability of the color variation from the final light output is characterized by the JND circle during the operational time. The same control mechanism can be applied to the laser color mixing system where instead of the color sensor; a proposed novel speckle wavemeter can provide the information on the change in wavelengths (accuracy 100 MHz) for the used laser during the operational time, which can further be converted into the desired parameters to provide the feedback to the control system. Experimental research was carried out on the VCSEL laser to validate the performance of the proposed speckle wavemeter examining the change in wavelength due to temperature variation during the operational time which is described in Chapter 6.

Finally, the light output from the prototype is compared with the Halogen-Fresnel lamp (2 kW) and shows that the V8 light engine (0.9kW) is 55% more energy efficient than traditional stage lighting. The comparison also indicates that the optical energy loss due to changing from flood to spot position is 10% for the V8 light engine while the traditional lighting loses 37%.

The following section will discuss the ideas which can be implemented in future for the betterment of the luminaire, which is proposed in this thesis.

7.2 Outlook

Due to time restrictions as well as the budgetary limitations, some ideas related to further extension of the project couldn't be materialized. However, this section discusses the ideas which could be implemented in future for the aspects of further improvement of the light output from the V8 light engine as well as for better understanding of the V8 light engine as a commercial product.

7.2.1 Beam spot

Due to the use of a hexagonal patterned MA in the V8 light engine design, the projected light output from the V8 light engine as a hexagonal shape. In addition, it has a positive distortion called pincushion due to the geometrical aberration of the lenses. This distortion can change with the change of working distance from the lens and distortions are different for different wavelength of light. Since the V8 light engine comprises several wavelengths, the chromatic aberration is predominant at the periphery of the light spot if the spot is projected on a screen. The pincushion distortion can be addressed by a lens correction model[155], [156]. To modify the shape of the spot from the hexagonal pattern to the circular one, several ideas can be adopted. Using the circular aperture can solve the problem with a tradeoff of energy loss. The random pattern of the lenslet of the MA can also be considered to solve the problem. However, to do so further research of the fabrication difficulty of the MA needs to be done. To address the issue for the chromatic aberration at the edge of the beam spot, the film with a fly-eye pattern can be added on the top surface of the Fresnel lens so that the beam will be evenly distributed. However, the pattern and the film material need to be optimized according to the application.

7.2.2 Light quality and visual perception

To enhance the optical efficiency of the V8 light engine, a phosphor converted blue laser (acting like white laser) with the correct optics for the beam shaping can be used inside the optical design. The present thesis reports on the tunable white light from 3000 K to 6000 K. However, there is a possibility of obtaining only saturated color with dimming ability as the V8 light engine covers a wide color gamut in the CIE 1930 chromaticity diagram.

The spectral control which is reported in the thesis minimizes the variations in luminous flux and CCT to some limit. However, it cannot control the variation in D_{uv}. Therefore it is observed that the controlled output is spread along the Iso-thermal line in Figure 5-18. Future work will address this issue and propose the error correction method in D_{uv} considering the tristimulus values from the color sensor.

Three LED color mixing systems are under development and will be used to experimentally demonstrate both system stability and system-to-system reproducibility. Monte Carlo results will be compared to the experimental results and further simulation work on the uncertainty contributions due to abrupt failure of LEDs, LED aging, and contamination of the optical system will be considered.

The same CCT and D_{uv} values can be obtained from two different white lights while the lights are produced by two different SPDs. When two lights from two different V8

light engines, which are different in SPDs, but with the same CCT and D_{uv} values, are projected on an object simultaneously side by side, the human eye can distinguish the difference between two lights to some extent according to the object reflectance and the visual perception of the human eye. These effects can be examined by user test, where two exposures shown side by side simultaneously from the two above mentioned light sources to the object and viewers will be asked to express their opinion on the experienced light on the screen. This experiment will lead to a result of the tolerance of the human eye towards the different light exposure.

7.2.3 V8 light engine components

Presently, the V8 light engine is using water cooling as a passive cooling, which is not convenient to use inside a compact product. Therefore, there is a research on to replacing the water cooling by active cooling using a heat pipe, a temperature sensor, together with a fan. This replacement will further enhance the stability of the light output by controlling the heat generation inside the V8 light engine.

The present parabolic reflector has a 10% reflection loss. There is a state-of-the-art on the surface quality enhancement of the reflector and the commercial product is available [157] to achieve a 5% reflection loss from the precision parabolic reflector. Therefore, in future there will be a potentiality to use a reflector with a better quality, which will lead to enhancement of the light output from the V8 light engine. The surface of the reflector needs to protect from corrosion, which will increase the durability and in this context, the utility of applying HSQ is quite significant[158], [159]. Further research can lead to improvement of the surface quality of the reflector.

The V8 light engine used a Fresnel lens is made by glass. In future it could be replaced by an acrylic Fresnel lens, which has a lighter weight along with a desired pattern to eliminate the chromatic aberration from the lens.

7.2.4 Scope for the customisation

There is a room for customizing the V8 light engine design according to the requirements. There was research made on the relation between the size and the light output from the V8 light engine. It was observed in the simulation, that the smallest V8 light engine (~ 10 cm) has the capability of illuminating 5000 lm, which can be used in many applications such as photo-voltatic lighting etc..

7.3 Application

By meeting the entertainment industry's critical demands for color gamut, color rendering of white light and intensity, the V8 light engine finally permits a revolutionary and attractive replacement of the energy consuming halogen based light sources in professional lighting. As an integrated light engine combining advanced optics, technology, and software, it is promising to integrate the V8 light engine as a light source in a wide range of products in a professional lighting; exploring the full potential of the LED technology. Optimized and size reduced technology will also be relevant for e.g. retrofit architectural lighting and lighting products for the consumer market[160].

7.3.1 Business potential

The V8 light engine has obvious commercial potentials: (a) as a retrofit light engine to replace energy consuming light sources in functioning Spotlights (ETC, Altman, ADB, Robert Juliat, Spotlight, De Sisti, Selecon, Strand, etc.). (b) as an integrated light source for new fixtures, automated lights and architectural lights. (c) as a light source for a revolutionary LED spotlight, designed by BB&S.

The increasing price of oil and the global need to reduce CO_2 emission leads to shift towards energy saving light sources in general. Most institutions in Denmark are forced to make energy saving investments within 4-5 years. V8 light engine is anticipated to meet this goal at a 5 hours daily use. If savings on cooling, maintenance, man hours, etc are involved, it would be even less. This tendency is projected to be relevant for the majority of leading institutions in the global entertainment industry, facing the challenge of energy reduction. As a retrofit, the V8 light engine offers a new LED solution to luminaries still in function, increasing the lifetime of the previous luminary investments. Apart from meeting the high standards of conventional halogen light sources, the V8 light engine also delivers completely new functions and features, based e.g. on the additional color mixing system. The V8 light takes the LED technology from "just as good" to "different".

The V8 light engine meets the customers (such as: theater, TV studio, sports, stadium, etc.) basic needs for:

1. An energy reducing light source.

2. A light source that meets the critical level for light intensity and color mix.

3. A cost effective solution concerning previous investments (retrofit).

The V8 light engine creates customer value by:

1. Reducing energy use by up to 90 % (selected colors)

2. Reducing the energy consumption related to cooling.

3. Providing light sources with a longer lifetime.

4. Eliminating IR and UV radiation

5. Offering a more cost efficient extension of the lifetime of functioning light fixtures.

6. Reducing other costs related to lighting (lower frequency in changing light sources, no overheated fixtures, reducing man hours, filters, e.t.c.)

The V8 light engine is unique to challenging LED products by

1. Proposing an optimal additional color mix of 5 or more different colored LED units, overcoming the technological limits/barriers of RGB coloring mixing

2. Offering high quality LED light sources to a wide range of professional lighting products in a unique light engine

3. Providing an integrated spotlight light source where the optical system combines the light source, advanced driver electronic, thermal cooling and color calibration, color control

References

"True leaders do not make choices with reference to the opinion of the majority. They make choices based on the opinion of the truth and the truth can come from either the majority or the minority!" - Israelmore Ayivor

Chapter 8 : Bibliography

[1]   ADB lighting, "' EUROPE ' RANGE PC and Fresnel Spotlights," 2000. [Online]. Available: http://www.adblighting.com/files/DS5113-E Europe PC & Fresnel data sheet.pdf.

[2]   J. K. Kim and E. F. Schubert, "Transcending the replacement paradigm of solid-state lighting.," *Opt. Express*, vol. 16, no. 26, pp. 21835–21842, 2008.

[3]   A. De Almeida, B. Santos, B. Paolo, and M. Quicheron, "Solid state lighting review - Potential and challenges in Europe," *Renew. Sustain. Energy Rev.*, vol. 34, pp. 30–48, 2014.

[4]   J. T. Bailey and P. L. S. Husar, "Multi-color focusable LED light," US005,752,766A, 1998.

[5]   K. J. Leblanc, L. D. Hagan, and B. Hammond, "LED floodlight system," US 2007/0019415 A1, 2007.

[6]   B. Chemel, M. K. Blackwell, C. Piepgras, and J. S. Warwick, "Method and apparatus for providing LED-based spotlight illumination in stage lighting applications," US 2010/0204841 A1, 2010.

[7]   J. GADEGAARD, T. K. JENSEN, D. T. JØRGENSEN, P. K. KRISTENSEN, T. SØNDERGAARD, T. G. PEDERSEN, and K. PEDERSEN, "High-output LED-based light engine for profile lighting fixtures with high color uniformity using freeform reflectors," *Appl. Opt.*, vol. 55, no. 6, pp. 1356–1365, 2016.

[8]   C.-C. Sun, I. Moreno, Y.-C. Lo, B.-C. Chiu, and W.-T. Chien, "Collimating lamp with well color mixing of red/green/blue LEDs.," *Opt. Express*, vol. 20, no. 1, pp. A75–84, 2012.

[9]   H. Murat, D. Cuypers, and H. De Smet, "Design of new collection systems for multi LED light engines," *Proc. SPIE*, vol. 6196, no. 2006, pp. 619604–619604–11, 2006.

[10]   A. Wilm, "Requirements on LEDs in etendue limited light engines," *Proc. SPIE,*

Photonics Multimed. II, vol. 7001, p. 70010F–70010F–10, 2008.

[11]   D. Jørgensen, "Color mixing illumination device," US20140185285 A1, 2012.

[12]   A. Neumann, J. J. Wierer, W. Davis, Y. Ohno, S. R. J. Brueck, and J. Y. Tsao, "Four-color laser white illuminant demonstrating high color-rendering quality.," *Opt. Express*, vol. 19 Suppl 4, no. May, pp. A982–A990, 2011.

[13]   M. Chakrabarti, C. Dam-Hansen, J. Stubager, F. T. Pedersen, and C. H. Pedersen, "Replication of optical microlens array using photoresist coated molds," *Opt. Express*, vol. 24, no. 9, pp. 9528–9540, 2016.

[14]   M. Chakrabarti, H. C. Pedersen, P. M. Petersen, C. Poulsen, P. P. Behrensdorff, and C. Dam-Hansen, "Focusable , color tunable white and efficient LED light engine for stage lighting," *Opt. Eng.*, vol. Manuscript, 2016.

[15]   H. C. Pedersen, T. Brockmann, and C. Dam-Hansen, "Light engine for an illumination device," EP2843301, 2015.

[16]   M. Chakrabarti, A. Thorseth, D. D. Corell, and C. Dam-Hansen, "A white – cyan-red LED system for low correlated colour temperature lighting," *Light. Res Technol*, vol. 0, pp. 1–14, 2015.

[17]   M. Aldrich, "Dynamic solid state lighting." Massachusetts Institute of Technology, 2010.

[18]   G. Eppeldauer, "Spectral response based calibration method of Tristimulus colorimeters," *J. Res. Natl. Inst. Stand. Technol.*, vol. 103, no. 6, p. 615, Nov. 1998.

[19]   J. L. Gardner, "Comparison of Calibration Methods for Tristimulus Colorimeters," *J. Res. Natl. Inst. Stand. Technol.*, vol. 112, no. 3, pp. 129–138, 2007.

[20]   H. Li, X. Mao, Y. Han, Y. Luo, and V. Author, "Wavelength dependence of colorimetric properties of lighting sources based on multi-color LEDs," *Opt. Express*, vol. 21, no. 3, pp. 3775–3783, 2013.

[21]   M. Chakrabarti, M. L. Jakobsen, and S. G. Hanson, "Speckle-based spectrometer.," *Opt. Lett.*, vol. 40, no. 14, pp. 3264–3267, 2015.

[22]   "Speckle based wavemeter," in *Speckle 2015: VI International Conference on Speckle Meterology*, 2015, p. 96600U–1.

[23]   M. Chakrabarti, A. Thorseth, J. Jepsen, and C. Dam-Hansen, "Monte carlo analysis of multicolour LED light engine," in *CIE*, 2015, p. OP60 526–10.

[24]   M. Chakrabarti, A. Thorseth, J. Jepsen, D. D. Corell, and C. Dam-hansen, "A color management system for multi-colored LED lighting," in *SPIE 9571, LED-based Illumination Systems*, 2015.

[25]   M. Chakrabarti, A. Thorseth, J. Jepsen, D. D. Corell, and C. Dam-Hansen, "Color control for tunable white LED lighting system," *Light. Res. Technol.*, vol. Under revi, 2016.

[26]   J. M. Bornhorst and T. DeSoto, "Additive color mixing system with variable hue and saturation light sources," 5,031,078, 1989.

[27]   S. Gotoh and J. Yao, "Colour mixing method for variable colour lighting and variable color luminaire for use with the method," US005384519A, 1995.

[28]   T. Fujii, Y. Gao, R. Sharma, E. L. Hu, S. P. DenBaars, and S. Nakamura, "Increase in the extraction efficiency of GaN-based light-emitting diodes via surface roughening," *Appl. Phys. Lett.*, vol. 84, no. 6, p. 855, 2004.

[29]   S. Keeping, "LED Efficacy Improvement Shows No Signs of Slowing," 2011.

[30]   S. Pimputkar, J. S. Speck, S. P. DenBaars, and S. Nakamura, "Prospects for LED lighting," *Nat. Photonics*, vol. 3, no. 4, pp. 180–182, 2009.

[31]   Y. Narukawa, M. Ichikawa, D. Sanga, M. Sano, and T. Mukai, "White light emitting diodes with super-high luminous efficacy," *J. Phys. D. Appl. Phys.*, vol. 43, no. 35, p. 354002, 2010.

[32]   Energy Efficiency & Renewable Energy, "Challenges in LED research and development," *U.S Department of Energy*, 2013. [Online]. Available: http://energy.gov/eere/ssl/text-alternative-version-challenges-led-research-and-development.

[33]   OSRAM, "LED knowledge: professional know how." [Online]. Available: http://www.osram.com/osram_com/news-and-knowledge/led-home/professional-knowledge/index.jsp.

[34]   CIE, "CIE 1931." Cambridge University Press, Cambridge, 1932.

[35]   E. F. Schubert, *Light -Emitting Diodes*, 2nd Editio. Cambridge University Press, 2006.

[36]   Light Research Center, "Swedish Energy Agency - Advanced Lighting Seminar." Rensselaer Polytechnic Institute, pp. 1–817, 2013.

[37]   C. DeCusatis, *Handbook of Applied Photometry*. AIP Press, 1997.

[38]   M. Rea, *Lighting Handbook: Reference and Application*, 9th ed. Iillumination Engineering Society of North America, 2000.

[39]   Joseph B. Murdoch, *Illumination engineering: from Edison's lamp to the laser*. Technology & Engineering, 1994.

[40]   CIE, *CIE S 025/E:2015: Test Method for LED Lamps, LED Luminaires and LED Modules*. 2015.

[41]   Technoteam, "Goniophotometer RiGO 801 General specification." 2015.

[42]   IESNA LM-79-08, "IES Approved Method for the Electrical and Photometric Measurements of Solid-State Lighting Products." ANSI, 2008.

[43]   D. MacAdam., "Visual sensitivities to color differences in daylight," *J.Opt. Soc. Amer.*, vol. 32, no. 5, pp. 247–74, 1942.

[44]   D. B. Judd and G. T. Yonemura, "CIE 1960 UCS Diagram and the Muller Theory of Color Vision," vol. 74, pp. 23–30, 1969.

[45]   CIE, "CIE S 014-5/E:2009 CIE 1976 L*u*v* Colour Space and u', v' Uniform Chromaticity Scale Diagram," in *Commission Internationale de L'Eclairage*, 2009.

[46]   CIE TN 001:2014, "Chromaticity Difference Specification for Light Sources," 2014.

[47]   American National Standard, "ANSI_ANSLG C78.377-2008," 2008.

[48]   Y. Ohno, "Calculation of CCT and Duv and Practical Conversion Formulae," in *CORM 2011 Conference*, 2011.

[49]   CIE, "Method of measuring and Specifying Colour Rendering Properties of Light Sources," 1995. [Online]. Available: http://www.cie.co.at/publ/abst/13-3-95.html.

[50]   G. Wyszecki and W. Stiles, *Color Science: Concepts and Methods, Quantitative Data and Formulae*. Wiley New York, 1982.

[51]   CIE, "TC 1-69: Colour Rendition by White Light Sources." 2009.

[52]   W. Davis and Y. Ohno, "Color quality scale," *Opt. Eng.*, vol. 49, no. 3, p. 033602, 2010.

[53]   Mike Wood, "Television Lighting Consistency Index 2012," 2012.

[54]   A. David, P. T. Fini, K. W. Houser, Y. Ohno, M. P. Royer, K. a. G. Smet, M. Wei, and L. Whitehead, "Development of the IES method for evaluating the color rendition of light sources," *Opt. Express*, vol. 23, no. 12, p. 15888, 2015.

[55]   IES TM-30-15, "IES Method for Evaluating Light Source Color Rendition," 2015.

[56]   "Correspondence: In support of the IES method of evaluating light source colour rendition," *Light. Res. Technol.*, vol. 47, no. 8, pp. 1029–1034, Nov. 2015.

[57]   Louis Hartmann, *Theatre lighting;: A manual of the stage switchboard*. New York: DBS, 1970.

[58]   Bobbi Owen, *Lighting Designers on Broadway: 1915 - 1990*. New York: Greenwood Press, 1991.

[59]   Yaron Abulafia, *The Art of Light on Stage: Lighting in Contemporary Theatre*. London and New York: Routledge, 1977.

[60]   J. Michael Gillette, *Theatrical Design and Production: An Introduction to Scene Design and Construction, Lighting, Sound, Costume and Makeup*, 4th ed. California: Mayfield Publishing Company, 2000.

[61]   I. Navigant Consulting, "Life-Cycle Assessment of Energy and Environmental Impacts of LED Lighting Products," 2012.

[62]   San Francisco Circuit, "Metal Core PCB / MCPCB," 2016. [Online]. Available: https://www.sfcircuits.com/pcb-production-capabilities/metal-core-pcb.

[63]   Multi-cb, "Printed Circuit Boards from Multi CB," 2016. [Online]. Available: http://www.multi-circuit-boards.eu/en/products/printed-circuit-boards/special-production/metal-core-pcb.html.

[64]   Epec Tec., "FLEX & RIGID-FLEX CIRCUITS." [Online]. Available: http://www.epectec.com/flex/.

[65]   ELFA, "Dielectricum," 2016. [Online]. Available: http://doctord.dyndns.org/courses/bei/ee360/Topics/Capacitors.pdf.

[66]   F. R. Fournier, W. J. Cassarly, and J. P. Rolland, "Fast freeform reflector generation usingsource-target maps.," *Opt. Express*, vol. 18, no. 5, pp. 5295–5304, 2010.

[67]   R. Zhu, Q. Hong, H. Zhang, and S.-T. Wu, "Freeform reflectors for architectural

lighting," *Opt. Express*, vol. 23, no. 25, p. 31828, 2015.

[68] W. D. Sproul, "Physical vapor deposition tool coatings," *Surf. Coatings Technol.*, vol. 81, no. 1, pp. 1–7, 1996.

[69] P. Benítez, V. Díaz, and J. Alonso, "Design and Manufacture of Aspheric Lenses for Novel High Efficient Photovoltaic Concentrator Modules," 2001.

[70] I. Wallhead, T. M. Jiménez, J. V. G. Ortiz, I. G. Toledo, and C. G. Toledo, "Design of an efficient Fresnel-type lens utilizing double total internal reflection for solar energy collection," *Opt. Express*, vol. 20, no. S6, p. A1005, 2012.

[71] C.-C. A. . Chen and F.-C. Lee, "FLOW FRONT ANALYSIS OF TIR LENS OF LEDS WITH INJECTION MOLDING," 2008.

[72] J. C. Miñano, M. Hernández, P. Benítez, J. Blen, O. Dross, R. Mohedano, and A. Santamaría, "Free-form integrator array optics," in *Proc. of SPIE*, 2005, vol. 5942, p. 59420C–59420C–12.

[73] R. Völkel and K. J. Weible, "Laser Beam Homogenizing: Limitations and Constraints," in *Proceedings of SPIE*, 2008, vol. 7102, p. 71020J–71020J–12.

[74] G. Naumann, H.; Schröder, *Bauelemente der Optik : TAschenbuch für Konstrukteure*. Carl Hanser Verlag, 1983.

[75] D. Meister and O. World, "Methods for Estimating Lens Thickness," *Opt. World*, vol. 26, no. 201, pp. 1–5, 1997.

[76] Micro.Chem, "MicroSpray™," 2016. [Online]. Available: http://www.microchem.com/Prod-Microspray.htm.

[77] B. McCall and T. S. Tkaczyk, "Fabrication of plastic microlens array for array microscopy by three-dimensional diamond micromilling," *Opt. Eng.*, vol. 49, no. 10, p. 103401, 2010.

[78] A. Y. Yi and L. Li, "Design and fabrication of a microlens array by use of a slow tool servo," *Opt. Lett.*, vol. 30, no. 13, pp. 1707–1709, 2005.

[79] S. Scheiding, A. Y. Yi, A. Gebhardt, R. Loose, L. Li, S. Risse, R. Eberhardt, and A. Tünnermann, "Diamond milling or turning for the fabrication of micro lens arrays: comparing different diamond machining technologies," *Proc. SPIE*, vol. 7927, no. 0, pp. 79270N–1–11, 2011.

[80] H. M. Leung, G. Zhou, H. Yu, F. S. Chau, and a S. Kumar, "Diamond turning and soft lithography processes for liquid tunable lenses," *J. Micromechanics Microengineering*, vol. 20, no. 2, p. 025021, 2010.

[81] J. Yong, F. Chen, Q. Yang, G. Du, H. Bian, D. Zhang, J. Si, F. Yun, and X. Hou, "Rapid fabrication of large-area concave microlens arrays on PDMS by a femtosecond laser," *ACS Appl. Mater. Interfaces*, vol. 5, no. 19, pp. 9382–9385, 2013.

[82] S. Scheiding, A. Y. Yi, A. Gebhardt, L. Li, S. Risse, R. Eberhardt, and Andreas T¨unnermann, R. Eberhardt, and A. Tünnermann, "Freeform manufacturing of a microoptical lens array on a steep curved substrate by use of a voice coil fast tool servo," *Opt. Express*, vol. 19, no. 24, p. 23938, 2011.

[83] G. Liu, W. Yu, H. Li, J. Gao, D. Flynn, R. W. Kay, S. Cargill, C. Tonry, M. K. Patel, C. Bailey, and M. P. Y. Desmulliez, "Microstructure formation in a thick polymer by electrostatic-induced lithography," *J. Micromechanics Microengineering*, vol. 23,

no. 3, p. 035018, 2013.

[84] W.-C. Chen, T.-J. Wu, W.-J. Wu, and G.-D. J. Su, "Fabrication of inkjet-printed SU-8 photoresist microlenses using hydrophilic confinement," *J. Micromechanics Microengineering*, vol. 23, no. 6, p. 065008, 2013.

[85] B. Jiri Cecha, H. Pranovb, G. Kofodb, M. Matschukb, S. Murthyb, and R. Taboryskia, "Surface roughness reduction using spray-coated hydrogen silsesquioxane reflow," *Appl. Surf. Sci.*, vol. 280, pp. 424–430, 2013.

[86] Lutron, "DMX-512 Fundamentals," 2010. [Online]. Available: file:///O:/FTNK/Public/RESOURCE-EDI/Projects/LED DTU/Maumita/Thesis/Reference/basic knowledge/DMX webinar_7-29-2010.pdf.

[87] Wyrowski Photonics UG, "Unified optical design software 'Wyrowski VirtualLab Fusion.'" LightTrans International UG, 2016.

[88] Wyrowski Photonics UG, "Wyrowski VirtualLab Fusion," 2016. [Online]. Available: http://www.wyrowski-photonics.com/virtuallab/news.html.

[89] J. M. P. J. Verstegen, D. Radielovic, and L. E. Vrenken, "A new generation deluxe fluorescent lamp - combining an efficacy greater than 80 lm/W with a color rendering index of about 85," *J. Illum. Eng. Soc.*, vol. 4, no. 2, p. 90, 1975.

[90] Karl Guttag on Technology, "Diode Green Lasers." 2011.

[91] DHgate, "Datasheet." 2015.

[92] Y.-C. Lo, I. Moreno, B.-C. Chiu, W.-T. Chien, J.-Y. Cai, Y.-Y. Chang, and C.-C. Sun, "Color mixing collimating lamp based on RGB LEDs," in *Proceedings of SPIE - The International Society for Optical Engineering*, 2012, vol. 8486, p. 84860T.

[93] S. Muthu, F. J. P. Schuurmans, and M. D. Pashley, "Red, green, and blue LEDs for white light illumination," *IEEE J. Sel. Top. Quantum Electron.*, vol. 8, no. 2, pp. 333–338, 2002.

[94] CREE, "LED Color Mixing: Basics and Background," 2016.

[95] E. F. Schubert, "Color mixing and color rendering," in *Light-Emitting Diodes*, 2nd ed., Cambridge University Press, 2006, pp. 313–327.

[96] D. B. Judd and G. T. Yonemura, "CIE 1960 UCS Diagram and the Muller Theory of Color Vision," *J. Res. Notional Bur. Stand. - A. Phys. Chem.*, vol. 74A, no. 1, pp. 23–30, 1969.

[97] ISO 11664-5:2009, "Colorimetry — Part 5: CIE 1976 L*u*v* Colour space and u', v' uniform chromaticity scale diagram," 2009.

[98] D. Corell, H. Ou, C. Dam-Hansen, P.-M. Petersen, and D. Friis, "Light Emitting Diodes as an alternative ambient illumination source in photolithography environment.," *Opt. Express*, vol. 17, no. 20, pp. 17293–17302, 2009.

[99] S. Chhajed, Y. Xi, Y. L. Li, T. Gessmann, and E. F. Schubert, "Influence of junction temperature on chromaticity and color-rendering properties of trichromatic white-light sources based on light-emitting diodes," *J. Appl. Phys.*, vol. 97, pp. 1–8, 2005.

[100] A. Thorseth, "Optimization of light quality from color mixing light-emitting

diode systems for general lighting," in *Proceedings of SPIE*, 2012, vol. 8278, p. 82781O–82781O–11.

[101]   M. S. Rea and J. P. Freyssinier, "White lighting: A provisional model for predicting perceived tint in 'white' illumination," *Color Res. Appl.*, vol. 39, no. V, pp. 466–479, 2014.

[102]   Y. Ohno and M. Fein, "VISION EXPERIMENT ON ACCEPTABLE AND PREFERRED WHITE LIGHT CHROMATICITY FOR LIGHTING," in *CIE 2014 Lighting Quality and Energy Efficiency Issue: CIE x039:2014*, pp. 192–199.

[103]   Philips Lumileds, "Color and White LED portfolio - Technical datasheet." 2014.

[104]   CREE, "Cree ® XLamp ® XP-E LEDs product family data sheet." pp. 1–38, 2014.

[105]   CREE, "Cree XLamp XT Family LEDs ® ® Binning & labeling." pp. 1–27, 2014.

[106]   Y.-F. Hsieh, O.-Y. Mang, T.-W. Huang, and C.-C. Lee, "Determination of optimal converting point of color temperature conversion complied with ANSI C78. 377 for indoor solid-state lighting and display applications," *Opt. Express*, vol. 20, no. 18, pp. 20059–20070, 2012.

[107]   Thomas Nimz and Fredrik Hailer and Kevin Jensen, "Sensors and Feedback Control of multi-colour LED systems," *LED professional Review (LpR)*, pp. 2–5, 2012.

[108]   S. Robinson and I. Ashdown, "Polychromatic Optical Feedback Control, Stability, and Dimming," in *Proc. of SPIE*, 2006, vol. 6337, pp. 633714–633714–10.

[109]   M. M. Sisto and J. Gauvin, "Accurate chromatic control and color rendering optimization in LED lighting systems using junction temperature feedback," in *Proc. SPIE*, 2014, vol. 9190, p. 919002.

[110]   K. Man and I. Ashdown, "Accurate colorimetric feedback for RGB LED clusters," in *Proc. of SPIE*, 2006, vol. 6337, pp. 633702–1.

[111]   G. He and J. Tang, "Spectral optimization of color temperature tunable white LEDs with excellent color rendering and luminous efficacy," *Opt. Lett.*, vol. 39, no. 19, pp. 5570–5573, 2014.

[112]   S. Buso and G. Spiazzi, "White light solid state lamp with luminance and color temperature control," in *COBEP 2011 - 11th Brazilian Power Electronics Conference*, 2011, pp. 837–843.

[113]   MAZeT GmbH, "True Color management for lighting systems," 2007.

[114]   J. L. Gardner, "Comparison of Calibration Methods for," vol. 112, no. 3, pp. 129–138, 2007.

[115]   M. Cox and P. Harris, "EVALUATION OF MEASUREMENT UNCERTAINTY BASED ON THE PROPAGATION OF DISTRIBUTIONS," vol. 46, no. 9, pp. 9–14, 2003.

[116]   Z. Liu, S. Liu, K. Wang, and X. Luo, "Optical Analysis of Color Distribution in White LEDs With Various Packaging Methods," *IEEE Photonics Technol. Lett.*, vol. 20, no. 24, pp. 2027–2029, Dec. 2008.

[117]   R. Qi and D. P. Bajorins, "Uncertainty analysis for chromaticity coordinates and luminous flux measurements of LEDs," vol. 9190, no. Ccd, p. 919008, Sep. 2014.

[118]   Gamma Scientific, "GS-1150 Handheld Spectrophotometers." 2015.

[119]   MAZeT GmbH, "Accuracy optimization of True Color Sensor solutions for LED color control of multiple LED light sources," 2012.

[120]   CIE, "Method of measuring and specifying colour rendering properties of light sources," *CIE 13.3*. p. 16, 1995.

[121]   CIE, "Chromaticity Difference Specification for Light Sources," 2014.

[122]   A. G. Ryabtsev, E. V. Lutsenko, G. I. Ryabtsev, G. P. Yablonskii, A. S. Smal, B. Schineller, and M. Heuken, "Study of laser threshold temperature sensitivity in optically pumped GaN epilayers," *Phys. STATUS SOLIDI C*, no. 1, pp. 479–482, 2002.

[123]   M. Fukuda, T. Mishima, N. Nakayama, and T. Masuda, "Temperature and current coefficients of lasing wavelength in tunable diode laser spectroscopy," *Appl. Phys. B Lasers Opt.*, vol. 100, no. 2, pp. 377–382, 2010.

[124]   L. I. Goldfischer, "Autocorrelation function and power spectral density of laser-produced speckle patterns," *JOSA*, vol. 55, no. 3, pp. 247–252, 1965.

[125]   J. W. Goodman, "Some fundamental properties of speckle," *JOSA*, vol. 66, no. 11, pp. 1145–1150, 1976.

[126]   J. C. Dainty, "Laser speckle and related phenomena," in *Berlin and New York, Springer-Verlag (Topics in Applied Physics. Volume 9), 1975. 298 p*, 1975, vol. 9.

[127]   I. Yamaguchi, "Speckle Displacement and Decorrelation in the Diffraction and Image Fields for Small Object Deformation," *Opt. Acta Int. J. Opt.*, vol. 28, pp. 1359–1376, 1981.

[128]   Yamaguchi I., "A laser-speckle strain gauge," *J.Phys E:Sci. Instrum*, vol. 14, 1981.

[129]   I. Yamaguchi, K. Kobayashi, and L. Yaroslavsky, "Measurement of surface roughness by speckle correlation," *Opt. Eng.*, vol. 43, no. November 2004, p. 2753, 2004.

[130]   I. Yamaguchi, "Digital Holographic Interferometry and Speckle Correlation," *AIP Conf. Proc.*, vol. 1236, pp. 46–51, 2010.

[131]   Brandon Redding and Hui Cao, "Using a multimode fiber as a high-resolution, low-loss spectrometer," *Opt. Lett.*, vol. 37, no. 16, pp. 3384–3386, 2012.

[132]   J. E. Webb, "CONCAVE GRATING SPECTROMETER," US3,229,568A, 1966.

[133]   J. M. Vaughan, *The Fabry Perot interferometer*, 0th ed. Taylor & Francis Group, 1989.

[134]   H.T.Yura and S.G.Hanson, "Optical beam wave propagation through complex optical systems," *JOSA A*, vol. 4, no. 10, pp. 1931 – 1941, 1987.

[135]   H. T. YURA and S. G. HANSON, "Optical Beam Wave-Propagation through Complex Optical-Systems," *J. Opt. Soc. Am. A-Optics Image Sci. Vis.*, vol. 4, no. 10, pp. 1931–1948, 1987.

[136]   P. Zhou and K. E. Goodson, "Subpixel displacement and deformation gradient measurement using digital image/speckle correlation (DISC)," *Opt. Eng.*, vol. 40, no. 8, p. 1613, 2001.

[137] M. Guizar-Sicairos, S. T. Thurman, and J. R. Fienup, "Efficient subpixel image registration algorithms.," *Opt. Lett.*, vol. 33, no. 2, pp. 156–158, 2008.

[138] J. H. Oh, S. J. Yang, Y.-G. Sung, and Y. R. Do, "Excellent color rendering indexes of multi-package white LEDs," *Opt. Express*, vol. 20, no. 18, p. 20276, 2012.

[139] Lei Jiang, Gu Xin, and M. Liu, "Spectral assemblage using LEDs to obtain specified characteristics," *Appl. Opt.*, vol. 53, no. 35, pp. 8151–8156, 2014.

[140] M. Zhang, Y. Chen, and G. He, "Color temperature tunable white-light LED cluster with extrahigh color rendering index.," *ScientificWorldJournal.*, vol. 2014, no. 9, p. 897960, Jan. 2014.

[141] X. Zhu, Q. Zhu, H. Wu, and C. Chen, "Optical design of LED-based automotive headlamps," *Opt. Laser Technol.*, vol. 45, no. 1, pp. 262–266, 2013.

[142] X. Zhu, J. Ni, and Q. Chen, "An optical design and simulation of LED low-beam headlamps," *J. Phys. Conf. Ser.*, vol. 276, p. 012201, 2011.

[143] E. Chen and F. Yu, "Design of LED-based reflector-array module for specific illuminance distribution," *Opt. Commun.*, vol. 289, pp. 19–27, 2013.

[144] MAZeT GmbH, "DATASHEET DK MTCS-INT-AB4," 2015.

[145] C. Mercinaries, "IOW24DG Converter I2C to USB." .

[146] Nikon corporation, "Confocal microscope," *The source for microscopy education*, 2015. [Online]. Available: http://www.microscopyu.com/articles/confocal/confocalintrobasics.html. [Accessed: 09-Jun-2016].

[147] Nikon Corporation, "White light interferometric microscopic system," 2015. [Online]. Available: http://www.nikon.com/about/technology/life/instruments/wl_interferometric /index.htm. [Accessed: 09-Jun-2016].

[148] ISO 4287:1997, "Geometrical Product Specifications (GPS) -- Surface texture: Profile method -- Terms, definitions and surface texture parameters," 1997. [Online]. Available: http://www.iso.org/iso/catalogue_detail.htm?csnumber=10132. [Accessed: 20-Sep-2015].

[149] E. Bretschneider, "Efficacy limits for solid-state white light sources," *Photonics Spectra*, vol. 41, no. 3, pp. 72–81, 2007.

[150] N. J. Miller and M. Royer, "Color Spaces and Planckian Loci: Understanding all those Crazy Color Metrics." pp. 1–49, 2012.

[151] X. Guo and K. W. W. Houser, "A review of colour rendering indices and their application to commercial light sources," *Light. Res. Technol.*, vol. 36, no. 3, pp. 183–199, 2004.

[152] W. Davis and Y. Ohno, "Toward an improved color rendering metric," *Proc. SPIE*, vol. 5941, no. 2, p. 59411G–59411G–8, 2005.

[153] W. Davis and Y. Ohno, "Evaluation of color di erence formulae for color rendering metrics," *NIST*, 2006. [Online]. Available: http://physics.nist.gov/Divisions/Div844/facilities/photo/.

[154] A. Žukauskas, R. Vaicekauskas, F. Ivanauskas, R. Gaska, and M. S. Shur, "Optimization of white polychromatic semiconductor lamps," *Appl. Phys. Lett.*, vol. 80, no. 2, pp. 234–236, 2002.

[155] D. Claus and a. W. Fitzgibbon, "A rational function lens distortion model for general cameras," *2005 IEEE Comput. Soc. Conf. Comput. Vis. Pattern Recognit.*, vol. 1, pp. 0–6, 2005.

[156] W. Hugemann, "Correcting lens distortions in digital photographs," *Ingenieurbüro Morawski+ Hugemann Leverkusen, …*, pp. 1–12, 2010.

[157] Edmund Optics, "Precision Parabolic Mirrors." 1992.

[158] J. Creusa, H. Idrissia, H. Mazille, F. Sanchetteb, and P. Jacquotb, "Corrosion behaviour of AllTi coating elaborated by cathodic arc PVD process onto mild steel substrate," *Thin Solid Films*, vol. 346, pp. 150–154, 1999.

[159] B. K. Hwang, K. Fujihara, U. I. Chung, K. H. Kim, S. I. Lee, and M. Y. Lee, "Application of HSQ (Hydrogen Silsesquioxane) Based SOG to Pre-Metal Dielectric Planarization in STC (Stacked Capacitor) DRAM," in *Symposium on VLSI Technology Digest of Technical Papers*, 1996, no. 1996, pp. 112–113.

[160] DTU Fotonik and BB&S Aps., "Advanced technology projects." 2011.

[161] B. Rose, S. G. . Hanson, and H. T. Yura, "Complex ABCD matrices: A general tool for analyzing arbitrary optical systems," in *Optical sensors and microsystems: New concepts , materials and technologies*, 1998.

[162] S. G. Hanson, M. L. Jakobsen, and H. T. Yura, "Complex-Valued ABCD Matrices and Speckle Metrology," in *Linear Canonical Transforms Theory and Applications*, vol. 27, no. 1, Springer, 2010, pp. 397–426.

[163] K. J. Beck, J.V.; Arnold, *Parameter estimation in engineering and science*. Wiley New York, 1977.

[164] A. Tarantola, *Inverse problem theory and Methods for Model Parameter Estimation*. Siam, 2005.

Appendix A

The following figure defines the light output geometry in stage lighting application.
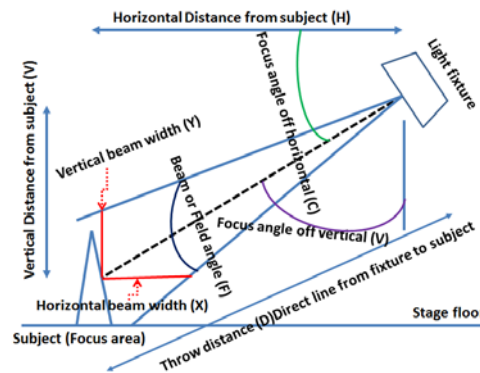

Figure 8-1 Describing the light output geometry in terms of FWHM at different distance

Appendix B

A goniospectro-photometer, called "REFLET" is used for measuring the back-scattering and forward scattering light from the diffusing sample. The BSDF (bidirectional scatter distribution function) measurement of the diffuser (section 3.4 in Chapter 3) was done in ENTPE, France. After that, the measured data was analyzed and the scatter model was fed into the Zemax software for further process. Figure 8-2 represents the Zemax BRDF (bidirectional reflectance distribution function) format where the light incident on the diffused surface creates a light cone upon reflection. Similarly, there will be a light cone after transmission from the diffuser. The detector inside the goniometer, measures reflected and transmitted light covering the full hemisphere (2π sr) by rotation. Thus, there are two angles to be considered; scattered radial and scatter azimuth during the rotation.
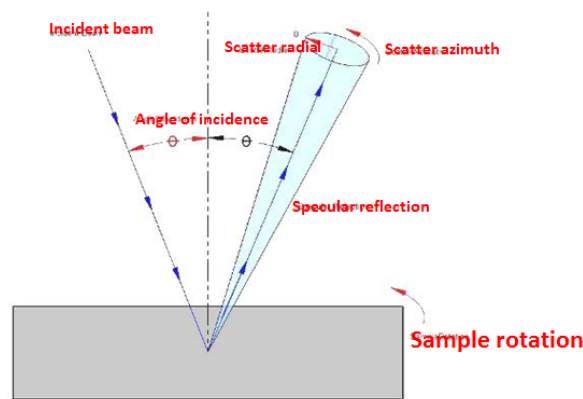

Figure 8-2: Diagram according to Zemax BRDF format which is adapted for the BRDF measurement

Appendix C

Light beam propagating through any complex optical system can be represented by an ABCD ray-transfer matrix[161], [162]. Mathematical approximations are required in each step if the field from one element to the next needs to be traced. The complex ABCD matrix method solves the problem differently, because the approximations are achieved on the optical system itself. Thus, the result acquired is effective for an arbitrary ABCD optical system. However, the consideration is limited and only true for the case where all illuminating beams are Gaussian shaped (only for TEM_{00} laser mode). This is because, Green's Functions in the Fresnel regime for free space propagation along with kernel for quadratic phase change presented by a lens are of a complex Gaussian form.

Appendix D

The calibration matrix can be found accurately using all 32 measurement points inside the S matrix and also utilizing the corresponding entire J matrix. In that scenario least-square estimate needs to consider[163], [164].

Therefore,

$$A = (J^t J)^{-1} J^t S \tag{58},$$

Where S and J represent are the 32 sets of tristimulus values from the spectrometer as well from the color sensor, respectively, whereas A is the calibration matrix.

If matrix F of measurement errors can introduce, then can be re-written as:

$$A = (J^t F^{-1} J)^{-1} J^t F^{-1} S \tag{59}$$